Finding Needles in the Haystack: A Search for AM CVn Systems using the Palomar Transient Factory

Thesis by

David B. Levitan

Advisor

Professor Thomas A. Prince

In Partial Fulfillment of the Requirements

for the Degree of

Doctor of Philosophy

California Institute of Technology

Pasadena, California

2013

(Defended May 28, 2013)

To my parents, Irina and Veniamin,

who were my first mentors and guides,

and have continued to be so for the last twenty-nine years.

To my sister, Eugenia, who has always

been there to help and support me.

And to Sarah, who has put up with my long nights and even longer trips.

May our love last as long as the stars,

yet have only joyful outbursts!

Acknowledgments

Thank you to everyone at the Palomar Observatory, the Keck Observatory, and the other telescopes I had the opportunity to work at for their support and help. In particular, I thank Kevin Rykoski, Carolyn Heffner, Jean Mueller, and Kajsa Peffer for their hard work in making every night at Palomar a success. Thanks to Patrick Shopbell and Anu Mahabal for supporting the computing infrastructure needed for this data-intensive project.

Last, but certainly not least, I thank my close friends and family. In particular, I thank Artemis Ailianou and Prakash Balachandran for always being there when I needed someone to talk to. And I thank my family, to whom I dedicate this thesis, without whom it would have never been possible.

Abstract

The AM CVn systems are a rare class of ultra-compact astrophysical binaries. With orbital periods of under an hour and as short as five minutes, they are among the closest known binary star systems and their evolution has direct relevance to the type Ia supernova rate and the white dwarf binary population. However, their faint and rare nature has made population studies of these systems difficult and several studies have found conflicting results.

I undertook a survey for AM CVn systems using the Palomar Transient Factory (PTF) astrophysical synoptic survey by exploiting the "outbursts" these systems undergo. Such events result in an increase in luminosity by a factor of up to two-hundred and are detectable in time-domain photometric data of AM CVn systems. My search resulted in the discovery of eight new systems, over 20% of the current known population. More importantly, this search was done in a systematic fashion, which allows for a population study properly accounting for biases.

Apart from the discovery of new systems, I used the time-domain data from the PTF and other synoptic surveys to better understand the long-term behavior of these systems. This analysis of the photometric behavior of the majority of known AM CVn systems has shown changes in their behavior at longer time scales than have previously been observed. This has allowed me to find relationships between the outburst properties of an individual system and its orbital period.

Even more importantly, the systematically selected sample together with these properties have allowed me to conduct a population study of the AM CVn systems. I have shown that the latest published estimates of the AM CVn system population, a factor of fifty below theoretical estimates, are consistent with the sample of systems presented here. This is particularly noteworthy since my population study is most sensitive to a different orbital period regime than earlier surveys. This confirmation of the population density will allow the AM CVn systems population to be used in the study of other areas of astrophysics.

Table of Contents

List of Figures

List of Tables

Chapter 1

Introduction

On a clear night, far from city lights, the sky is filled with thousands upon thousands of stars. It is perhaps surprising to many people that half of these stars are not single stars like our Sun, but in fact have a companion. Most such binary systems have orbital periods on the order of years or tens of years. A few, known as compact binaries, have evolved to have orbital periods of hours. Fewer still are the ultra-compact binaries, those systems with orbital periods below *one hour*.

My thesis concentrates on the AM Canum Venatoricum (AM CVn) systems, a sub-class of ultra-compact binaries that are characterized by their semi-detached nature with helium-rich, hydrogen-deficient spectra. Though they may be among the rarest ultra-compact binaries in the Galaxy, observationally they are much easier to identify than their siblings, such as detached, double white-dwarf binaries and ultra-compact X-ray binaries. This is a result of their unique helium-rich, hydrogen-deficient spectra and the presence of an accretion disk, making them both brighter than many detached systems and more prone to photometric variability.

One of the unsolved problems related to AM CVn systems, and other ultra-compact binaries, is their population density. Understanding this is important as it directly relates to several other areas of astrophysics, including the type Ia supernova rate, common envelope evolution, and gravitational wave science. Unfortunately, counting stars is tricky, as you must count not only what you *can* see but also what you *can't* see.

AM CVn, the prototype of the class, was first proposed to be an ultra-compact binary by Smak (1967). Over the following thirty years fewer than a dozen more systems were identified; all were serendipitous discoveries. These systems, selected outside of systematic searches, provided little information on what was not discovered.

Luckily, the Sloan Digital Sky Survey (SDSS), a combined photometric and spectro-

scopic astronomical survey, was released in 2005 and provided a large data set over which a systematic search for AM CVn systems could be carried out and, equally importantly, whose biases could characterized. Within only three years *six* new systems were discovered, increasing the known population by 50%. This provided the *first* sample that could be used to characterize the population of AM CVn systems.

However, a population study based on these newly-discovered, systematically-selected systems found a factor of 20 fewer systems than had been earlier predicted from population synthesis calculations. Even more worrying was a follow-up search for AM CVn systems in the SDSS was predicted to find >40 new systems, but had found fewer than 10. It was clear that a second sample was needed. One that was selected in a different, but even more characterizable, fashion than the SDSS sample.

1.1   The AM CVn Systems

The AM CVn systems are generally characterized as helium-rich, hydrogen-poor, semi-detached binaries composed of a white dwarf (WD) accretor and a (semi-)degenerate donor. Their orbital periods range from 5 min to over 65 min. A simulated rendering of such a system is shown in Figure 1.1. In many ways, the AM CVn systems are believed to be the helium cousins of the hydrogen-rich and much more populous cataclysmic variables (CVs; Warner 1995). It is important to remember that while phenomenologically they appear to share many similarities, from an evolutionary perspective they are believed to be extremely different. More extensive recent reviews of AM CVn systems can be found in Nelemans (2005) and Solheim (2010).

The accretor is believed to be a He or C/O WD with a typical mass of 0.5–$1 M_\odot$ and it is assumed to contribute most of the luminosity of the system (Bildsten et al. 2006). The Roche-lobe filling donor has not been directly observed in any AM CVn system with an orbital period (P_{orb}) of over 10 min. It is believed to be either a low mass He WD or an evolved He star, depending on the progenitor of the system. AM CVn systems are believed to form only when the two components have an extreme mass ratio. At birth the donor star will have a mass of a few tenths of a Solar mass, but by an orbital period of 10-20 min, this will have decreased to <$0.1 M_\odot$ due to the high mass transfer rate (Deloye et al. 2007).

The semi-detached nature of AM CVn systems means that they have an accretion-disk
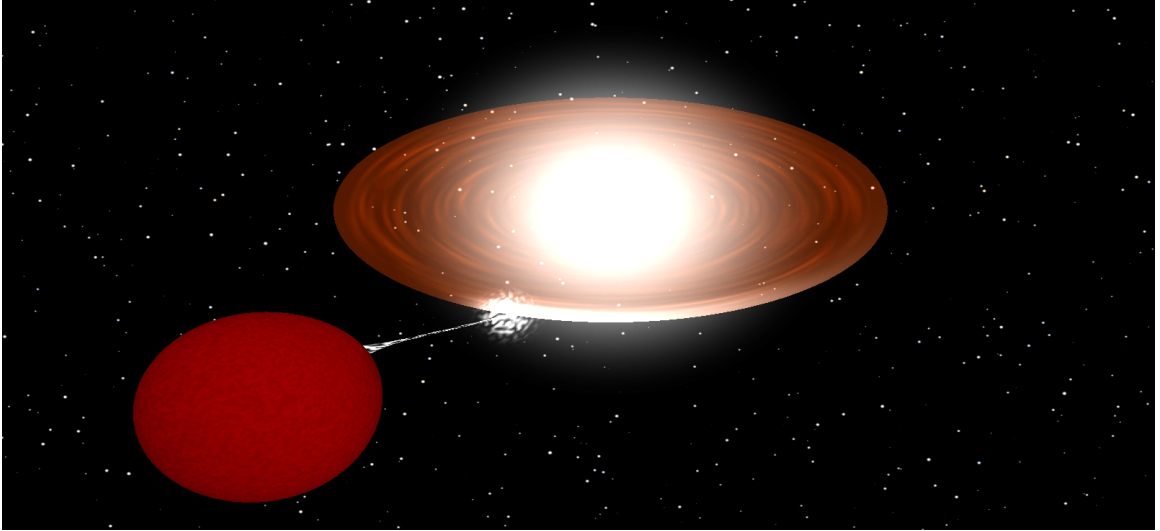
Figure 1.1 A simulated AM CVn system in quiescence, showing the bright and relatively massive accretor, the much larger (in volume) but less massive donor star, the accretion disk, and the matter stream from the donor to the accretion disk with the hot spot formed when it impacts the disk. I emphasize that while the accretor is much more luminous than the donor (as shown here), it in fact has a significant smaller radius. This figure was generated using the BINSIM package (Hynes 2002).

through which matter is transferred from the donor to the accretor. Of critical importance to the study of these systems is the presence of the so-called hot spot, which is formed when the matter from the donor interacts with the edge of the accretion disk. The motion of this small area of increased luminosity can be detected on the otherwise homogeneous accretion disk (to first order), and thus the orbital period of the system can be measured spectroscopically (Nather et al. 1981).

1.1.1 Evolutionary Channels

AM CVn systems are believed to be post-period minimum systems that form from one of three classes of possible progenitor systems: detached WD binaries (DWDs; Paczyński 1967), evolved He-star binaries (Paczyński 1971), and evolved CV systems (Podsiadlowski et al. 2003). The DWD channel is thought to be responsible for most AM CVn systems (Nelemans et al. 2001; Nissanke et al. 2012) and is the only channel with candidate progenitors (Kilic et al. 2012). However, this has not been conclusively shown and at least some of the currently known systems are likely to be from the He-star channel (Roelofs et al. 2007a; Nelemans et al. 2010). In my thesis, I consider only the DWD channel since the progenitors

of AM CVn systems cannot, at present, be easily distinguished (Nelemans et al. 2010) and the evolution of DWDs is the most straightforward to model and best understood.

DWD systems are composed of two WDs that are believed to have evolved through two common-envelope phases. The system emerges as a relatively close binary and loses angular momentum through the radiation of gravitational waves (e.g., Landau & Lifshitz 1971). The subsequent evolution of the system is believed to depend primarily on the total mass of the system and the mass ratio, $q = M_{don}/M_{acc}$, between the components. When the less massive and therefore larger WD fills its Roche lobe at an orbital period of 5–10 min, mass transfer will start. Systems with a mass ratio near unity will undergo "unstable mass transfer" and likely merge, resulting in either a type Ia supernova or an exotic star, such as an R Cor Bor star (Webbink 1984). The outcome of systems with more extreme mass-ratios ($q < 2/3$) is much more poorly understood. Many such systems are believed to survive through this phase (referred to as "stable mass transfer") and pass through a period minimum to become AM CVn systems. However, the exact circumstances that allow for a system to survive are poorly understood (Nelemans et al. 2001; Marsh et al. 2004). I refer the reader to Figure 2 of Solheim (2010) for a graphical view of this process.

Understanding the population of AM CVn systems is critical, as it is linked to the type Ia supernova rate, the population of R Cor Bor stars, and is essential to understanding the outcome of DWD mergers. AM CVn systems, together with their DWD progenitors, are also strong Galactic gravitational wave sources, particularly for space-based, millihertz gravitational wave detectors (Nelemans et al. 2004; Nissanke et al. 2012). Lastly, immediately following the birth of AM CVn systems, they are believed to be the sources of the proposed ".Ia" supernovae, which are particularly interesting as so-called "gap" transients (Bildsten et al. 2007; Kasliwal et al. 2010).

The post-birth orbital evolution of AM CVn systems is believed to continue under the influence of the same forces. It is important to remember that the youngest members of the class are those with the shortest orbital periods, while the longest period examples are the oldest. The youngest also have the most massive donors, and hence the highest mass transfer rate from the donor to the disk. This means that AM CVn systems evolve quickest when young, and spend most of their lifetimes at longer orbital periods (Nelemans et al. 2004; Nissanke et al. 2012).

1.1.2   Observed Features

Phenomenologically, the AM CVn systems have been observed to have two distinct states. In the "high" state, they are best characterized by helium absorption-line spectra thought to be from an optically-thick disk (Roelofs et al. 2006b). In contrast, in the quiescent state systems are observed to have helium emission lines in their spectra and to be significantly fainter (Ruiz et al. 2001). Systems with $P_{orb} < 20\,\text{min}$ have always been observed to be in the high state, while those with $P_{orb} > 40\,\text{min}$ are thought to remain in the quiescent state. Between these two groups of systems are the outbursting systems, which have been observed to switch from the quiescent state to the high state, showing a change of 3–6 mag. These events are referred to as outbursts. I note that the recent discovery of an outbursting system with $P_{orb} \approx 47\,\text{min}$ (Woudt et al. 2013) indicates that the lower limit on the orbital periods of permanently quiescent systems may not be as well-defined as previously thought.

AM CVn systems are typically classified as such based on their unique spectra, which vary over the lifetime of each system, but always show the presence of helium and the absence of hydrogen. The emission line features of the quiescent systems are strongest and narrowest towards longer orbital periods. In particular, the longest orbital period systems are observed to have a strong "central spike" feature in their He emission lines (Ruiz et al. 2001) that makes identification even more straightforward. Shorter period systems, those with $20\,\text{min} < P_{orb} < 40\,\text{min}$ have significantly broader He-emission lines (Carter et al. 2013a). However, any spectrum of a Galactic object with He emission lines and without the presence of H is likely an AM CVn system. I note that the shortest period systems show He absorption lines which, without high-resolution spectroscopy, are difficult to differentiate from the spectra of DB white dwarfs (Carter et al. 2013a).

The AM CVn systems show a variety of photometric variability. The outbursting systems are the best example of this, with outburst recurrence times between a few months and several years. The outbursts are believed to be driven by the same disk instability model (DIM; for a review, see Lasota 2001) as that for hydrogen-rich CVs. Recent work has been able to model AM CVn system outbursts using the DIM (Kotko et al. 2012). Although their outburst light curves are similar to those of CVs, as my thesis shows, it is possible to identify AM CVn systems by searching for their outbursts.

Apart from the outburst phenomena, AM CVn systems often have photometric variability at the orbital timescale. Those systems in the high state have been observed to show superhumps, which are believed to result from the deformation of the accretion disk during outburst (Osaki 1989). They have been observed to have amplitudes of ∼0.1 mag and recur with periods a few percent longer than the orbital period (e.g., Patterson et al. 1997, 2005). Some AM CVn systems have also been observed to have photometric variability at the orbital period in quiescence. In CVs, this phenomenon has been linked to the motion of the hot spot (Schoembs & Hartmann 1983). Although the low amplitude of both sets of variability is difficult to identify in surveys, it allows for a rough orbital period measurement based solely on photometric data.

1.2 The AM CVn System Population

The known AM CVn systems can be divided into four groups by discovery method. Roughly half were discovered serendipitously. While they are the most numerous, the lack of a systematic approach to their discovery makes a population study difficult. The remainder are equally divided between three systematic searches. The first such search was that of the SDSS spectroscopic survey which discovered six systems (Roelofs et al. 2005; Anderson et al. 2005, 2008). A follow-up spectroscopic survey of a color-selected sample of systems from the SDSS photometric database yielded an additional seven systems (Roelofs et al. 2009; Rau et al. 2010; Carter et al. 2013a). These two samples are closely related, as both were selected based on the spectral properties of the systems. They are most sensitive to the longer-period systems that have strong emission-line spectra. The last sample, which is presented in this work, is the PTF-selected sample, and was selected by a search for the AM CVn systems' photometric variability. As such, it is most sensitive to shorter-period outbursting systems.

The population density of a class of astrophysical sources can be calculated either theoretically, by means of a population synthesis calculation, or observationally, by means of a well-characterized survey of the sources of interest. The two most prominent population density calculations for the AM CVn systems represent both approaches. Nelemans et al. (2001), hereafter N01, calculated the population density of AM CVn systems using a population synthesis calculation. They modeled the birth and death rates of AM CVn systems,

and were thus able to compute the expected density. In contrast, Roelofs et al. (2007d), hereafter R07, used the SDSS sample to observationally calibrate the earlier population synthesis calculation. This was further refined with the expanded SDSS sample by Carter et al. (2013a), hereafter C13.

However, the population estimates of both N01 and R07 have not been supported by observations. The population density estimate in C13 is a factor of *fifty* lower than the estimate from N01 and a factor of three lower than that of R07. Since it is not known why the population is smaller than predicted, a sample of systems not related to the SDSS sample is necessary to confirm the latest estimate from C13.

1.3 Finding a New Sample

As described in Section 1.1.2, AM CVn systems have several observational features that can be exploited for the discovery of new systems. The systems in the SDSS sample were discovered based on their spectra, either through a direct search of the SDSS spectroscopic database or the follow-up classification of color-selected systems. It is thus most sensitive to longer-period systems, which have the most unambiguous spectra.

To find a complementary sample of AM CVn systems, I searched for their photometric variability, specifically their outbursts, to identify candidate systems. Crucially, these systems were not selected based on their colors. For this project, I used the Palomar Transient Factory (PTF; Law et al. 2009; Rau et al. 2009) synoptic survey. The PTF used the Palomar 48″ Samuel Oschin Schmidt telescope to observe up to $2,000\,\mathrm{deg}^2$ of the sky per night, with $\sim 7\,\mathrm{deg}^2$ covered per exposure. In comparison, the full moon is $\sim 0.2\,\mathrm{deg}^2$. PTF observations were scheduled with a nominal cadence of 3–5 days and used either a Mould R-band filter or a Gunn g'-filter. Its total coverage exceeded that of the SDSS, with $\geq 16,000\,\mathrm{deg}^2$ covered over the course of the four-year survey. As such, it provides a large data set that could be characterized while providing a substantial sample. Candidates, both transients and variable stars, are classified using low-resolution spectroscopy at a number of follow-up telescopes, including the Palomar 200″ Hale and the Keck-I 10 m telescopes.

The PTF used two distinct pipelines to process data. The first, available since the beginning of the project in 2009, concentrated on the real-time discovery of transient events (Gal-Yam et al. 2011). Although the first AM CVn discovered by the PTF was from

this pipeline, it was designed to focus on transient events (e.g., supernovae) and was not optimized for the analysis of long-term light curves.

Instead, a significant part of my work was to help in the development of the so-called "photometric pipeline." This pipeline, optimized for accuracy as opposed to speed, provided a well-characterized set of light curves that could be used to search for outbursting systems.

1.4 Thesis Overview

The goal of this work has been to identify a new sample of AM CVn systems selected from their outbursting behavior and to compare this sample and any population density that can be derived from it to the SDSS sample. The PTF supplied the ideal data for such a survey and allowed me to systematically select outbursting AM CVn systems.

Chapters 2, 4, and 5 report on the discovery of eight new AM CVn systems, all using the PTF. As part of these studies, I confirmed the link between the hot spot of an AM CVn system and its orbital period, studied in better detail the normal outburst phenomena, and compared the colors of our sample to that of the SDSS sample. An important section of Chapter 2 details the calibration algorithm used for PTF light curves, as well as for the calibration of my follow-up photometric data. Chapter 5 reports on the second known eclipsing AM CVn system, and includes the first published data from the CHIMERA high-speed photometer, which hints at the possibility of even shorter term photometric variability.

Chapter 3 provides a technical overview of the PTF photometric pipeline. I discuss image processing, source detection matching, and the relative photometric calibration. I also provide details on the performance of this pipeline.

In Chapter 6, I combine the photometric data from three synoptic surveys, including the PTF, and construct almost $10\,\mathrm{yr}$ long light curves of most known outbursting AM CVn systems. I used these light curves to measure the outburst properties of the respective systems and found relationships between these properties and the orbital periods of AM CVn systems. The light curves also showed even longer-term variability in the outburst behavior of some systems, and provided evidence that earlier definitions of outbursting systems are perhaps too simple.

Chapter 7 reviews the Palomar Transient Factory's data and the goals and setup of the Palomar Transient Factory Outbursting System Survey. I characterize the detection proba-

bility of AM CVn systems by the Palomar Transient Factory and constrain the population density independently of previous work.

Finally, in Chapter 8, I summarize the discoveries and advances made in this work and consider future steps that will help us better understand the AM CVn systems.

Chapter 2

PTF1 J071912.13+485834.0: An Outbursting AM CVn System Discovered by a Synoptic Survey[⋆]

David Levitan[1], Benjamin J. Fulton[2], Paul J. Groot[3,4], Shrinivas R. Kulkarni[4], Eran O. Ofek[4,5], Thomas A. Prince[1], Avi Shporer[2,6], Joshua S. Bloom[7], S. Bradley Cenko[7], Mansi M. Kasliwal[4], Nicholas M. Law[8], Peter E. Nugent[9], Dovi Poznanski[5,7,9], Robert M. Quimby[4], Assaf Horesh[4], Branimir Sesar[4], and Assaf Sternberg[10]

[1] Department of Physics, California Institute of Technology, Pasadena, CA 91125, USA

[2] Las Cumbres Observatory Global Telescope Network, 6740 Cortona Drive, Suite 102, Santa Barbara, CA 93117, USA

[3] Department of Astrophysics IMAPP, Radboud University Nijmegen, PO Box 9010, NL-6500 GL Nijmegen, the Netherlands

[4] Cahill Center for Astrophysics, California Institute of Technology, Pasadena, CA 91125, USA

[5] Einstein fellow

[6] Department of Physics, Broida Hall, University of California, Santa Barbara, CA 93106, USA

[7] Department of Astronomy, University of California, Berkeley, CA 94720-3411, USA

[8] Dunlap Institute for Astronomy and Astrophysics, University of Toronto, 50 St. George Street, Toronto M5S 3H4, Ontario, Canada

[9] Computational Cosmology Center, Lawrence Berkeley National Laboratory, 1 Cyclotron Road, Berkeley, CA 94720, USA

[10] Benoziyo Center for Astrophysics, Faculty of Physics, Weizmann Institute of Science, Rehovot 76100, Israel

Abstract

We present extensive photometric and spectroscopic observations of PTF1 J071912.13+485834.0, an outbursting AM CVn system discovered by the Palomar Transient Factory (PTF). AM CVn systems are stellar binaries with some of the smallest separations known and orbital periods ranging from 5 to 65 minutes. They are believed to be composed of a white dwarf accretor and a (semi)-degenerate He-rich donor and are considered to be the helium equivalents of cataclysmic variables (CVs). We have spectroscopically and photometrically identified an orbital period of 26.77 ± 0.02 minutes for PTF1 J071912.13+485834.0 and found a super-outburst recurrence time of greater than 65 days along with the presence of "normal" outbursts — rarely seen in AM CVn systems but well known in super-outbursting CVs. We present a long term light curve over two super-cycles as well as high cadence photometry of both outburst and quiescent stages, both of which show clear variability. We also compare both the outburst and quiescent spectra of PTF1 J071912.13+485834.0 to other known AM CVn systems, and use the quiescent phase-resolved spectroscopy to determine the origin of the photometric variability. Finally, we draw parallels between the different subclasses of SU UMa-type CVs and outbursting AM CVn systems. We conclude by predicting that the PTF may more than double the number of outbursting AM CVn systems known, which would greatly increase our understanding of AM CVn systems.

2.1   Introduction

AM CVn systems — ultra-compact semi-detached binaries — are stellar binaries with some of the smallest separations known. They have been found with orbital periods ranging from 5 to 65 minutes. The prototype, AM CVn, was initially identified as a possible binary star by Smak (1967) and was eventually theorized to be composed of a relatively massive white dwarf accretor and a much lower mass semi-degenerate or degenerate helium-transferring donor (Paczyński 1967; Faulkner et al. 1972a). AM CVn systems are believed to be one of the strongest Galactic low-frequency gravitational wave sources (Nelemans et al. 2004; Roelofs et al. 2007d) and the source of the proposed ".Ia" supernovae (Bildsten et al. 2007). We refer the reader to Nelemans (2005) and Solheim (2010) for reviews.

Short-period systems — those with orbital periods below roughly 20 minutes — are in a constant state of high mass transfer from the secondary to the optically thick accretion disk. They are known as "high" state systems, and their spectra, dominated by the accretion disk, are characterized by broad, shallow helium absorption lines with few other features. High-state systems have been observed to have superhumps — photometric variability of ~ 0.1 mag with a period slightly longer than the orbital period (e.g. Patterson et al. 1997) — similar to those found in SU UMa-type cataclysmic variables (CVs; Osaki 1996).

At the other end of the period range are the quiescent systems with orbital periods above roughly 40 minutes. They are believed to have low mass transfer rates and an optically thin disk. Instead of absorption lines, these systems have prominent helium emission lines in their spectra. Quiescent systems do not show prominent photometric variability.

Between these two period ranges are the so-called outbursting AM CVn systems, which feature outbursts similar to those found in dwarf novae-type CVs. While in the "high" state, these systems exhibit the properties of short-period AM CVn systems, and while in the "quiescent" state, they exhibit properties of the long-period AM CVn systems (see e.g. Roelofs et al. 2007b). In outburst they are typically 3–5 mag brighter than in quiescence and feature superhumps. These outbursts tend to last for a few weeks, and recur on a timescale (where known) between 46 days (e.g. Kato et al. 2000) and over a year (e.g. Copperwheat et al. 2011). Between the two states, some of these systems have been observed to have a "cycling" state wherein some experience magnitude changes of ~ 1 mag with a period of about a day (Patterson et al. 2000). One system, CR Boo, has also been found to have "normal" outbursts that last 1-2 days and recur every 4-8 days (Kato et al. 2000), as opposed to the longer "super-outbursts" described previously.

AM CVn systems have been extensively compared to CVs. Of primary interest for this comparison are the SU UMa-type dwarf novae-type CVs, which exhibit both super-outbursts and normal outbursts, but with somewhat longer typical recurrence times than outbursting AM CVn systems. See Warner (1995) for an extensive review. While the photometric behavior is similar between dwarf novae and AM CVn systems, the chemical composition, structure of the donor, and evolutionary pathways are very different.

Only 26 AM CVn systems have been reported in the literature. Being intrinsically rare and with colors similar to those of ordinary white dwarfs, they are difficult to discover and population estimates have proven to be difficult to calculate (e.g. Nelemans et al. 2001;

Roelofs et al. 2007d). Initially, AM CVn systems were serendipitous discoveries, typically as a result of their photometric variability or color. More recently, the population has almost doubled as a result of the Sloan Digital Sky Survey (SDSS). Seven systems were discovered from a search for spectra containing helium emission lines (Roelofs et al. 2005; Anderson et al. 2005, 2008) and five more from a follow-up color selection and spectroscopic survey (Roelofs et al. 2009; Rau et al. 2010).

However, the wide variety of photometric variability exhibited by AM CVn systems makes them an effective target for large-scale, synoptic surveys. The most recent published new AM CVn system, with an orbital period of 15.6 minutes, was discovered in *Kepler* satellite data from its superhump-induced photometric variability (Fontaine et al. 2011a). Here, we present a new AM CVn system discovered in outburst by the Palomar Transient Factory (PTF) — the first system discovered by a systematic, synoptic survey covering thousands of square degrees.

The PTF[1] uses the Oschin 48 inch telescope (P48) at the Palomar Observatory to image $7.2 \, \mathrm{deg}^2$ with each exposure. In a typical night, up to $\sim 2000 \, \mathrm{deg}^2$ are observed to a depth of $R \sim 20.6$ (Law et al. 2009; Rau et al. 2009).

We begin by describing the discovery of PTF1 J071912.13+485834.0[2] (hereafter PTF1J0719+4858) and summarizing our follow-up observations. In Section 2.3 we present photometric observations. We describe the features of both outburst and quiescent spectra in Section 2.4, as well as the determination of the spectroscopic period from phase-resolved spectroscopy. In Section 4.4, we compare PTF1J0719+4858 to other outbursting AM CVn systems, discuss the source of the quiescent photometric variability, and consider how many more such systems can be discovered by PTF. Finally, we summarize in Section 2.6.

2.2 Discovery and Summary of Observations

PTF1J0719+4858 was detected in outburst by the PTF at $R = 15.8$ on 2009 December 1 and classified as a transient with the designation PTF09hpk[3]. A graphical summary of the PTF photometry can be found in Figure 2.1.

---

[1] http://www.astro.caltech.edu/ptf

[2] "PTF1" refers to preliminary versions of the PTF catalog, as opposed to sources from the final catalog, which will use "PTF". It is possible that a source in the PTF1 catalog will have slightly different coordinates in the PTF catalog.

[3] This is a PTF transient designation. For stellar discoveries, we use the more conventional IAU variable star coordinate name.
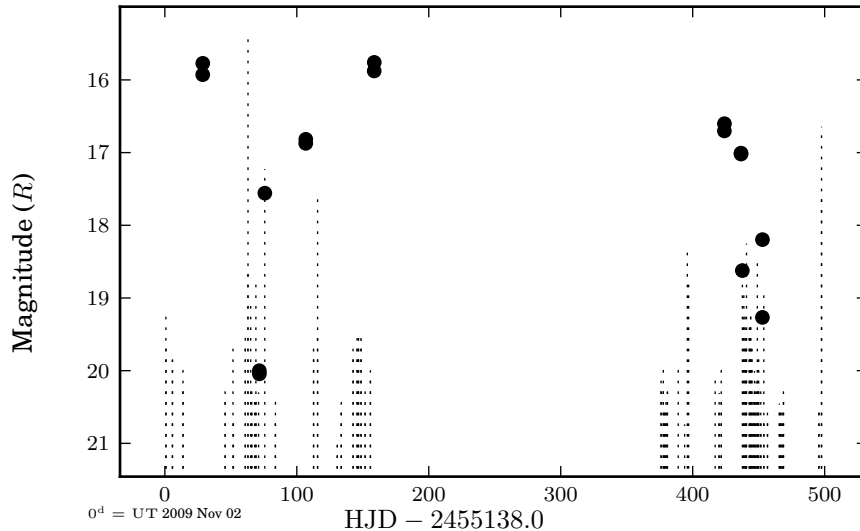
Figure 2.1 PTF light curve of PTF1J0719+4858. Discovery occurred at the first data point. Magnitudes were obtained by difference imaging relative to a deep co-add reference image as part of the PTF Transient Pipeline. The tops of the dashed lines represent limits for non-detections and are theoretical calculations based on observed conditions. Errors on observations in outburst are $\sim 0.01\,\mathrm{mag}$ and errors in quiescence are $\sim 0.1\,\mathrm{mag}$. Note that these observations are in the R band as opposed to the g' band used in the rest of this paper. PTF1J0719+4858 is a blue object and hence fainter in R.

A classification spectrum was taken using Keck-I/LRIS (McCarthy et al. 1998) on 2010 January 14 and reduced using standard IRAF tasks. Noticing the lack of a redshift, the PTF extragalactic team classified the spectrum as a CV. In a subsequent inspection of the PTF spectral database, we noticed the presence of multiple distinct, double-peaked helium emission lines, some with a central peak (we refer the reader to Section 2.4.2 which contains a high signal-to-noise quiescence spectrum), and it was re-classified as an AM CVn system candidate.

We focused our follow-up efforts on both long-term monitoring and short time-scale variability studies, using the Palomar $60''$ telescope (P60) and two telescopes from the Las Cumbres Observatory Global Telescope Network (LCOGT; Shporer et al. 2010): the 2-m Faulkes Telescope North (FTN) and the $32''$ Byrne Observatory at Sedgwick (BOS). Between 2010 October and 2011 March, we obtained a total of 195 exposures in good weather for our long-term photometric monitoring campaign using P60 and FTN with a goal of obtaining at least one exposure per night. We present this light curve in Section 2.3.2. We also observed PTF1J0719+4858 at high cadence several times to characterize the photometric variability on the order of the orbital period, both in quiescence and in

outburst. We discuss the periods identified from these observations in Section 2.3.3.

Besides photometric observations, we also obtained individual spectra of PTF1J0719+4858 on multiple nights, as well as phase-resolved spectroscopy. Individual spectra of PTF1J0719+4858 were obtained with Keck-I, the William Herschel Telescope (WHT), and the Palomar 200″ Hale Telescope in 2010 October and November. To obtain the orbital period, we obtained roughly four hours of spectroscopic observations with Keck-I/LRIS using three minute exposures. These observations are presented in Section 2.4.2.

2.3 Photometric Observations and Results

2.3.1 Analysis and Reduction Process

Palomar 60″ data were de-biased and flat-fielded using the P60 pipeline (Cenko et al. 2006). The FTN data were processed using the LCOGT pipeline. The BOS data were de-biased and flat-fielded using IRAF tasks, astrometrically calibrated using ASTROME-TRY.NET (Lang et al. 2010), and cosmic rays were removed using the L.A. COSMIC algorithm (van Dokkum 2001). The SEXTRACTOR package (Bertin & Arnouts 1996) was used to identify sources in each exposure and their instrumental magnitudes were obtained using optimal point-spread function photometry (Naylor 1998) as implemented by the STARLINK[4] package AUTOPHOTOM.

Light curves were calculated using a matrix-based, least-squares minimization, relative photometry algorithm. The primary goal of any such algorithm is to minimize noise, typically by assuming certain stars in the field are non-variable and identifying an optimal zero point for the exposure. We expanded on this to simultaneously solve for both the zero-point and additional de-trending terms that corrected for airmass and instrument changes. The algorithm is similar to that developed in Honeycutt (1992) and is described in the Appendix of Ofek et al. (2011).

To accomplish the de-trending, we modeled each observation as

$$m_{i,j} = \overline{M}_j + Z_i + \alpha c_j A_i + \sum_{k=1}^{n_k} \beta_k c_j$$

---

[4]The STARLINK Software Group homepage can be found at http://starlink.jach.hawaii.edu/starlink.

where the needed data are as follows.

- $m_{i,j}$: the magnitude of source j on exposure i.

- c_j: a color for each source. The color is required to compensate for the stronger effects of airmass on blue stars, as well as the differences in CCD efficiency over a range of wavelengths. For our light curves, we used $c_j = g'_j - r'_j$, where g'_j and r'_j refer to the magnitudes of the jth source in the respective SDSS filters.

- A_i: the airmass of each exposure.

The terms to be fitted are as follows.

- Z_i: the optimal zero-point term of each exposure.

- $\overline{M}_j$: the mean magnitude term of the source.

- α: the airmass calibration coefficient for all exposures and sources

- β_k: the kth telescope/instrument calibration coefficient, for $k = 1, 2, \ldots, n_k$ where n_k is the number of telescopes. This term is introduced to take into account the different responses of each telescope/instrument. For light curves with data from only one instrument, these terms were not used.

It is important to ensure that all stars used for the solution (calibration stars) are themselves not variable. We restricted the stars used to those found in 80%–100% of exposures, depending on the light curve, and iteratively removed any sources with high residuals. Since the solution is not unique unless reference magnitudes are provided, we used blue magnitudes from USNO-B 1.0.

This algorithm provided very good results — even light curves taken over months with different telescopes and conditions obtained a magnitude scatter (rms) of ~ 0.035 mag for $g' \approx 16$ and ~ 0.055 mag for $g' \approx 19.4$, the quiescent magnitude of PTF1J0719+4858. The rms errors provided with the figures in this paper are based on the median scatter of other stars with similar magnitude present in at least 50% of observations. Additionally, individual errors — the combination of the Poisson error and the fit errors — are provided for some of the light curves. These are typically very close to the magnitude scatter, except for those exposures obtained during bad weather.

For high-cadence light curves, period analysis was performed with SIGSPEC (Reegen 2007). All default options were used, except as noted for individual cases, and weights for measurements were always provided. SIGSPEC produces a list of significant periods and corresponding "sig" values. A "sig" value of c means that the period has a chance of 1 in 10^c of being noise.

2.3.2 Long-term Photometric Behavior

The long-term light curve of PTF1J0719+4858 from FTN and P60 is presented in Figure 2.2. We note the pattern of "high" states and "quiescent" states. Additionally, we note the presence of "normal" outbursts (as opposed to the "super-outbursts" more commonly associated with AM CVn systems).

We observed the 2011 January super-outburst in its entirety and find a rise time from the last measurement in quiescence to the peak magnitude of 3.2 days with Δmag = 3.6. Immediately following this rise, we see a drop to a plateau that may be the cycling state seen in other AM CVn systems (e.g., Patterson et al. 2000). Finally, 22 days after the beginning of the super-outburst, PTF1J0719+4858 returned to quiescence.

The recurrence time was significantly different between the two super-cycles we observed. We approximate (assuming the behavior of the super-outburst itself is the same) that the recurrence time from the first super-outburst to the second was 65 days. However, the recurrence time from the second super-outburst to the third is greater than 78 days (this uncertainty is due to weather impacting our observations).

Between super-outbursts, we observed normal outbursts in PTF1J0719+4858, which have also been identified in CR Boo (Kato et al. 2000). After initially observing single data points indicating a sudden jump in luminosity, we successfully predicted the 2011 January 29 outburst and obtained a total of 41 exposures, of which 12 are from BOS and are not included in the long-term light curve. The light curve of this outburst is presented in Figure 2.3. During this normal outburst, PTF1J0719+4858 experienced a luminosity increase of 2.5 mag over 7 hr from the last observation at $g' > 19.4$ to the brightest point measured. If we consider only the increase from $g' > 19$ we find an increase of 2.1 mag over only 4 hr.

The recurrence time of the normal outbursts was stable throughout the first super-cycle. We observed three normal outbursts with a recurrence time of $\sim$ 10.5 days. This most likely represents all the normal outbursts in this super-cycle, due to our almost daily coverage.

18
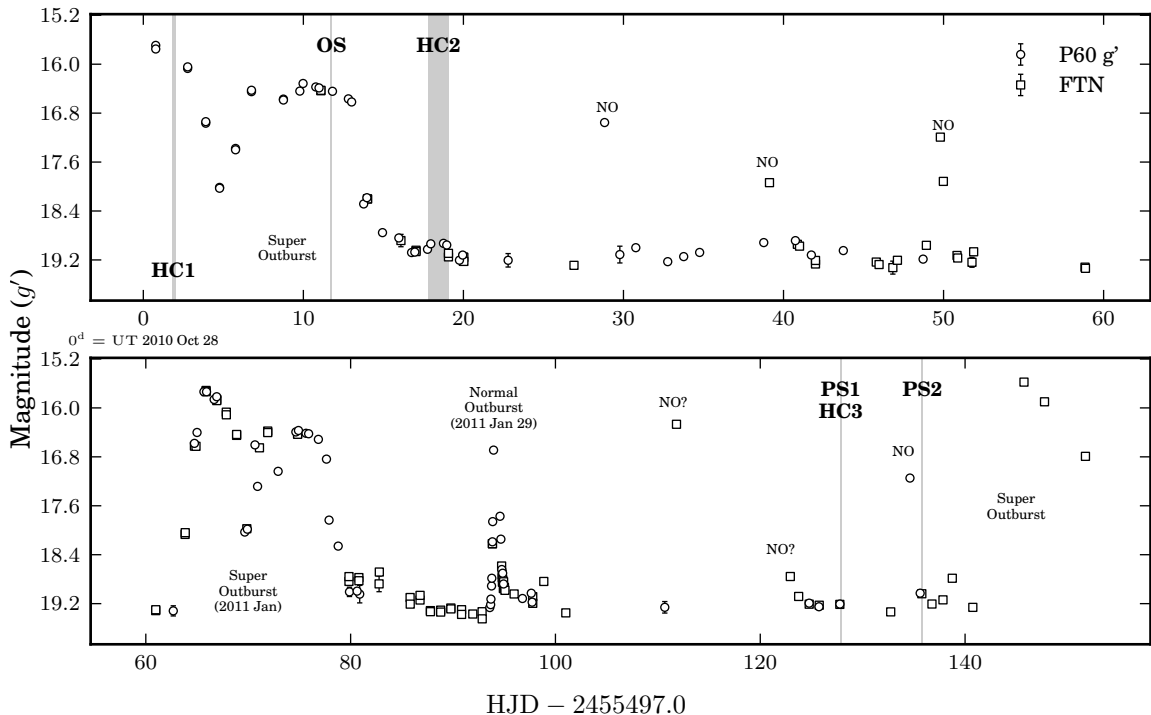
Figure 2.2 Long-term light curve of PTF1J0719+4858 with 90 exposures from P60 and 105 exposures from FTN. Exposures from both telescopes were 60 s and we attempted to obtain 1–2 exposures per night. Twenty-nine calibration stars were used to achieve an rms of ~ 0.055 mag in quiescence and an rms of ~ 0.035 mag in outburst (small enough that the error bars cannot be seen). Observations with $\sigma > 0.075$ mag (due to weather or other issues) are marked with error bars. Note the difference in the scale of the time axis for the upper and lower panels: the top half shows the first super-outburst cycle (~ 60 days) and the bottom half shows the second cycle (~ 80 days).

The 2011 January super-outburst (the only one observed in its entirety) is labeled as is the normal outburst of 2011 January 29. The other data points we believe to be normal outbursts are labeled as NO. Two of these points are questionable due to lack of observations, and are identified with a question mark. The quiescent magnitude is $g' \approx 19.4$.

The high cadence runs in Table 2.1 are identified as HCn while the phase-resolved spectroscopy runs discussed in Section 2.4.2 are identified as PSn. The outburst spectrum discussed in Section 2.4.1 is labeled as OS.
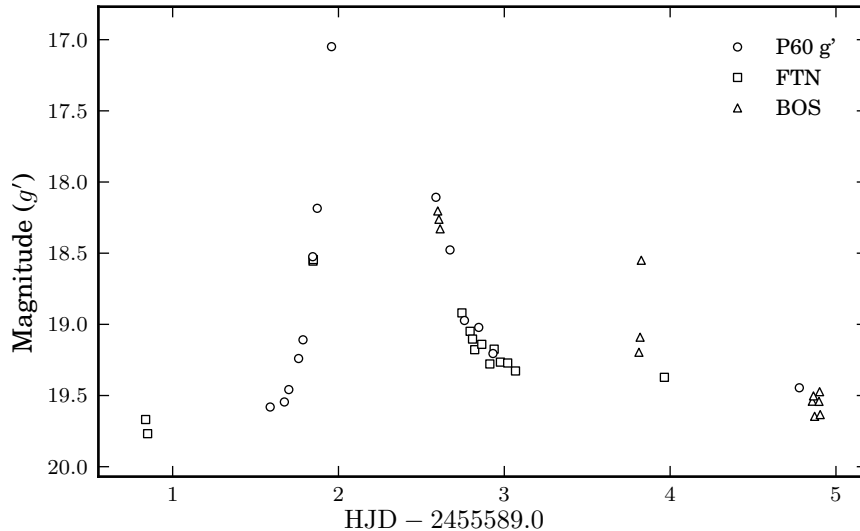
Figure 2.3 Normal outburst of PTF1J0719+4858 (2011 January 29). The light curve contains 41 exposures, with 14 from P60 (60 s), 15 from FTN (60 s), and 12 from BOS (300 s). Forty-five calibration stars were used. At $g' \approx 17$, rms ≈ 0.02 mag and at $g' \approx 19.5$, rms ≈ 0.04 mag.

The delay between the end of the second super-cycle and the first normal outburst was the same as that in the first super-cycle. However, it appears that the normal outburst recurrence time was significantly different in the second super-cycle, likely associated with the longer recurrence time of the super-outburst. Given our poor coverage (as a result of weather), we cannot make any statements about these differences.

2.3.3   High-cadence Photometry

Short-term photometric variability was detected in several high-cadence observations of PTF1J0719+4858 (see Table 2.1 and labels in Figure 2.2).

During the first super-outburst (labeled HC1), we detected photometric variability of Δmag ≈ 0.1 (see Figure 2.4) with a shape consistent with that of superhumps in other AM CVn systems (e.g., Patterson et al. 1997; Wood et al. 2002). Analysis of the period using a Lomb-Scargle periodogram suggests it is ~ 27 minutes, while a SIGSPEC analysis found a period of ~ 26 minutes. Given that we observed only two cycles, we cannot state a more accurate superhump period.

A second set of high-cadence observations (labeled HC2) was obtained almost immediately after PTF1J0719+4858 returned to quiescence following the first observed super-outburst. Here, we see photometric variability of Δmag ≈ 0.2. We performed a SIGSPEC

Table 2.1.   High-cadence photometry runs of PTF1J0719+4858

Label	Telescope	UT Date(s)	Exposures	Read-out Time (s)
HC1	P60	2010 Oct 29	$92 \times 45\,\mathrm{s}$	10^{a}
HC2	BOS	2010 Nov 14/15	$54/60 \times 300\,\mathrm{s}$	31
HC3	P60	2011 Mar 4	$87 \times 60\,\mathrm{s}$	24

Note. — All exposures taken with a g' filter.

[a]Taken in quarter-chip mode, which decreased read-out time
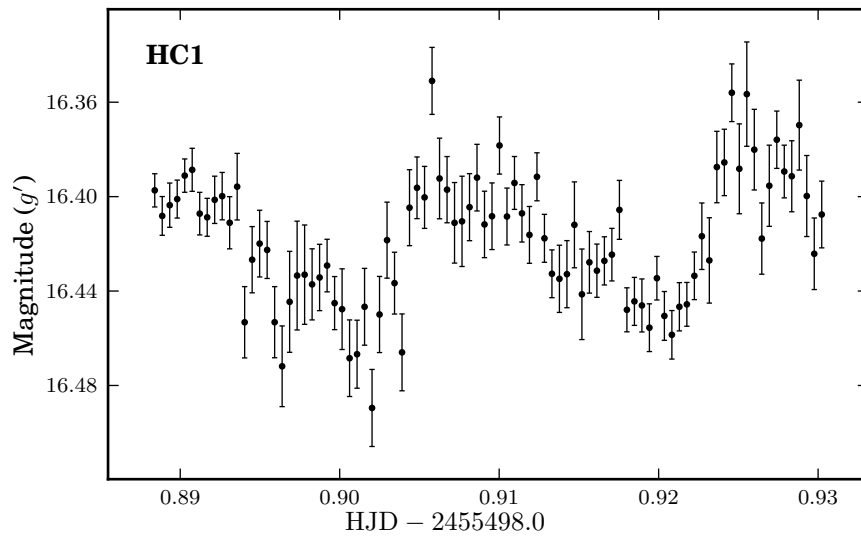
Figure 2.4 Superhumps of PTF1J0719+4858. The light curve was constructed using 12 calibration stars, and other sources at this magnitude had an rms of $\sim 0.015\,\mathrm{mag}$. The shape is consistent with superhumps in similar systems such as CR Boo (Patterson et al. 1997) and KL Dra (Wood et al. 2002).
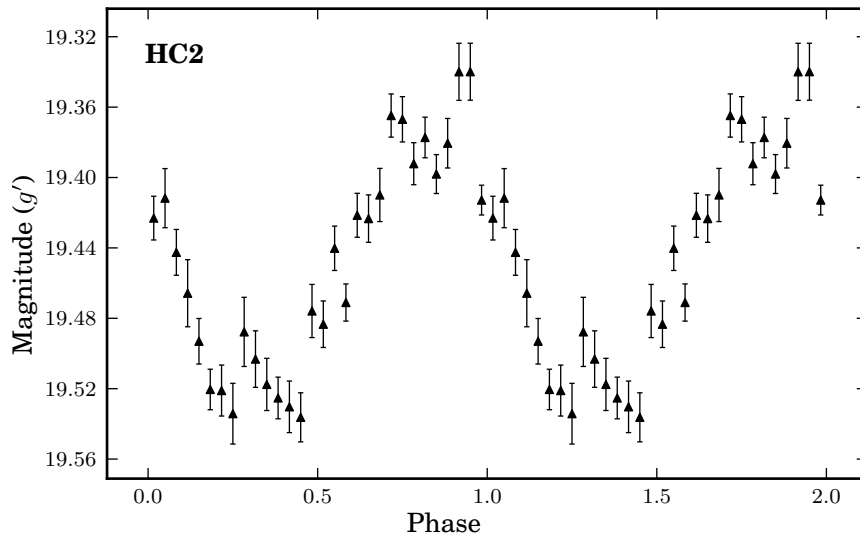
Figure 2.5 Phase-binned light curve of PTF1J0719+4858 in quiescence from 114 BOS exposures of 300 s folded on a period of 1606.3 s. Eighteen calibration stars were used to construct the light curve. At this magnitude, rms ≈ 0.035 mag. Error bars for individual points are based on the standard deviation of all measurements in that phase bin. An arbitrary zero phase of HJD = 2455514.831555 (the start of the observations) was used.

analysis of the light curve for these two nights with the AntiAIC anti-aliasing feature enabled and found a period of 1606.3 ± 2.5 s with a "sig" of 13.7. Since we observed many periods of this variability, we present a phase-binned light curve in Figure 2.5. Additional observations that allow a more precise determination of the superhump period could be used along with the quiescent photometric period to determine a mass ratio (Patterson et al. 2005).

We also obtained a set of high cadence observations (labeled HC3) coincident with our phase-resolved spectroscopy at Keck-I (see Section 2.4.2). These observations also showed photometric variability,with Δ mag ≈ 0.06. PTF1J0719+4858 was in quiescence at the time of the observations. A SigSpec analysis identified a period of 1550 s with a sig of 3.1. Given the short observation time and the low significance, we folded the light curve at both this period and the spectroscopic period obtained in Section 2.4.2. These produced similar results and, thus, we believe that the true period is that obtained via phase-resolved spectroscopy. We discuss the simultaneous photometry and spectroscopy in Section 2.5.2.
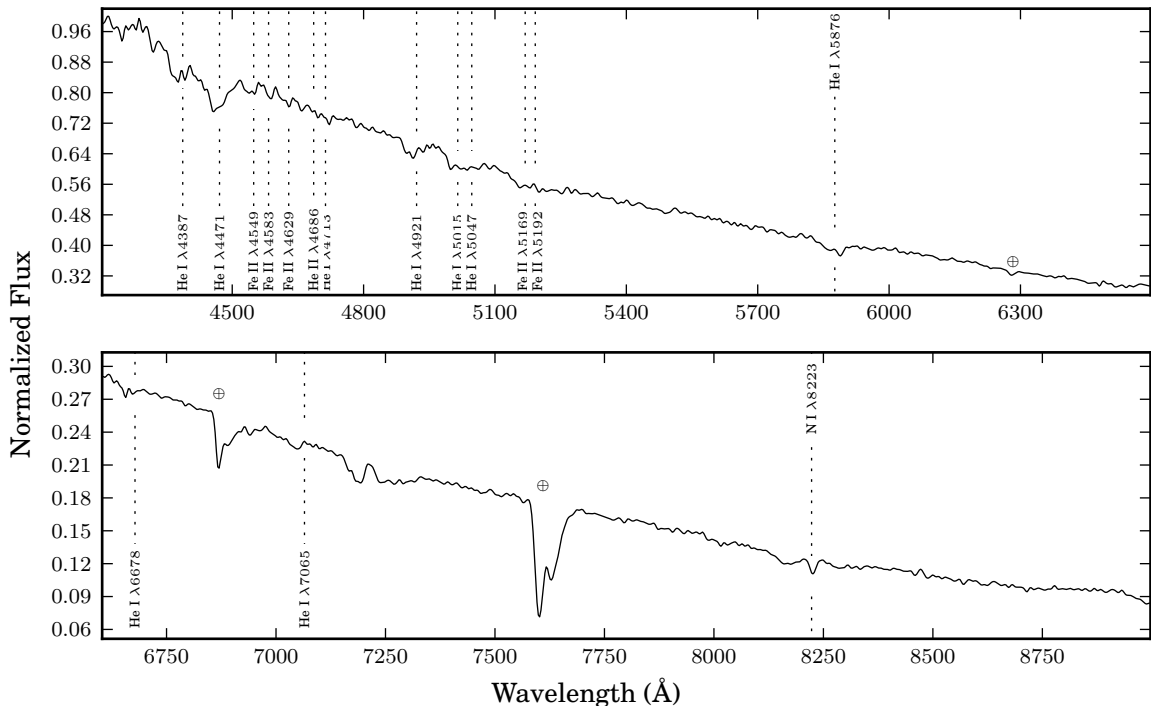
Figure 2.6 Outburst spectrum of PTF1J0719+4858 taken with WHT/ACAM on 2010 November 6. Strong helium absorption lines are present throughout the spectrum, as well a Fe II lines. We also highlight the N I λ8223 absorption line, which has not been seen before in an AM CVn system in the high state.

2.4 Spectroscopic Observations and Results

2.4.1 Follow-up Spectra

The identification spectra were reduced as part of the PTF spectroscopic program using standard IRAF tasks. We present a typical outburst spectrum — taken with WHT/ACAM (Benn et al. 2008) on 2010 November 6 and labeled as OS in Figure 2.2 — in Figure 2.6 with the prominent lines identified. The outburst spectra varied slightly, with absorption lines being more prominent on some than on others. However, He I λ4471 was always visible. The best spectrum in quiescence is the co-added spectrum of the phase-resolved observations, shown in Figure 2.7, again with lines identified.

The quiescence spectrum features very broad, double-peaked emission lines, some with a possible central spike. Shortward of 4000 Å, the spectrum shows an interplay of lines that is consistent with Ca II H and K emission interwoven with He I λ3888 (see Roelofs et al. 2006a), but the low resolution of the current observation and the broadness of the lines

Table 2.2.   Equivalent widths of identified lines of PTF1J0719+4858 from co-added quiescence spectrum

Line	Equivalent Width (Å)
He I λ4387	-4.9 ± 0.1
He I λ4471	-9.4 ± 0.1
He II λ4686 + He I λ4713	-9.8 ± 0.3
He I λ4921	-3.7 ± 0.1
He I λ5015 + 5047	-5.2 ± 0.2
He I λ5876	-14.7 ± 0.3
He I λ6678	-10.7 ± 0.4
He I λ7065	-7.2 ± 0.4

make their presence difficult to establish. We can establish the presence of Fe II, Si, and N I emission lines in the rest of the spectrum. It is also possible that He II λ4200 is seen in the spectrum, albeit very weak. He II λ4200 has not been previously seen in an AM CVn system. In the outburst spectrum, we see weak absorption lines of He I and He II, as well as Fe II. Si is not seen, but we note the presence of N I λ8223, which has not been seen this strong in other high-state AM CVn systems.

Table 2.2 lists the equivalent widths of the most prominent emission lines. Based on the presence of the noted elements, we find that the spectra of PTF1J0719+4858 are most similar to those of 2003aw (Roelofs et al. 2006a) and SDSSJ0804+1616 (Roelofs et al. 2009). Future work in identifying abundances may shed light on the chemical composition and evolutionary history of such systems (Nelemans et al. 2010).

2.4.2   High-speed Spectroscopy in Quiescence

Here, we discuss the phase-resolved spectroscopy undertaken at the Keck Observatory (see Table 2.3). The spectra were reduced using optimal extraction (Horne 1986) as implemented in the Pamela code (Marsh 1989) as well as the Starlink packages kappa, figaro, and convert. For these exposures, wavelength calibration exposures were taken at the beginning, middle, and end of each set of observations using the Hg, Cd, and Zn lamps for the blue CCD and the Ne and Ar lamps for the red CCD. Wavelength calibration for individual spectra was interpolated between these calibration spectra. We present a co-added spectrum in Figure 2.7.

We use a technique similar to previous analyses of AM CVn system phase-resolved

Table 2.3.   Phase-resolved spectroscopy of PTF1J0719+4858 using Keck-I/LRIS

UT Date	CCD	Disp. Elem.	Bins[a]	Slit (″)	Exposures
2011 Mar 04	Blue	600/4000	4×4	1.5	$37 \times 180\,\text{s}$
2011 Mar 04	Red	600/7500	4×4	1.5	$35 \times 180\,\text{s}$
2011 Mar 12	Blue	600/4000	4×2	0.7	$32 \times 180\,\text{s}$
2011 Mar 12	Red	600/7500	4×2	0.7	$30 \times 180\,\text{s}$

[a]Spectral $\times$ spatial
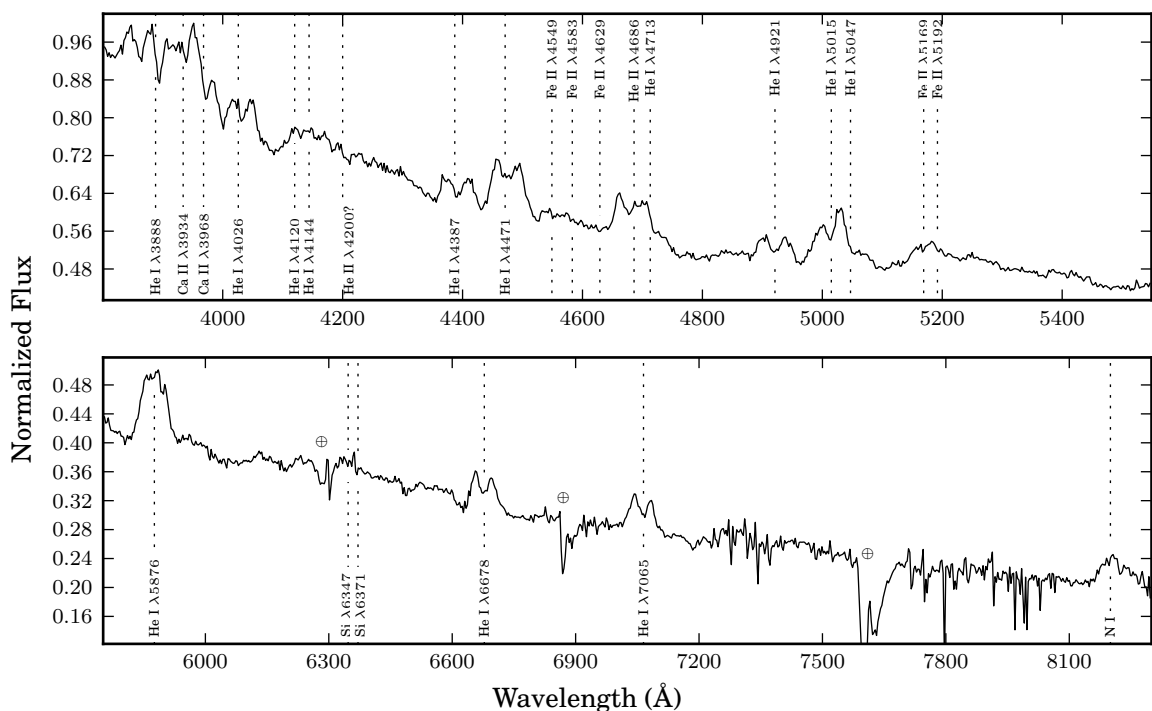
Figure 2.7 Co-added Keck-I/LRIS quiescence spectrum of PTF1J0719+4858. A total of 72 exposures of 180 s were co-added for the blue side. For the red side, 62 exposures of 180 s were median co-added to remove cosmic ray effects. Strong helium lines are evident, along with Fe II and Si $\lambda 6347 + 6371$. A broad emission feature of N I is also present at $\sim 8200\,\text{Å}$.
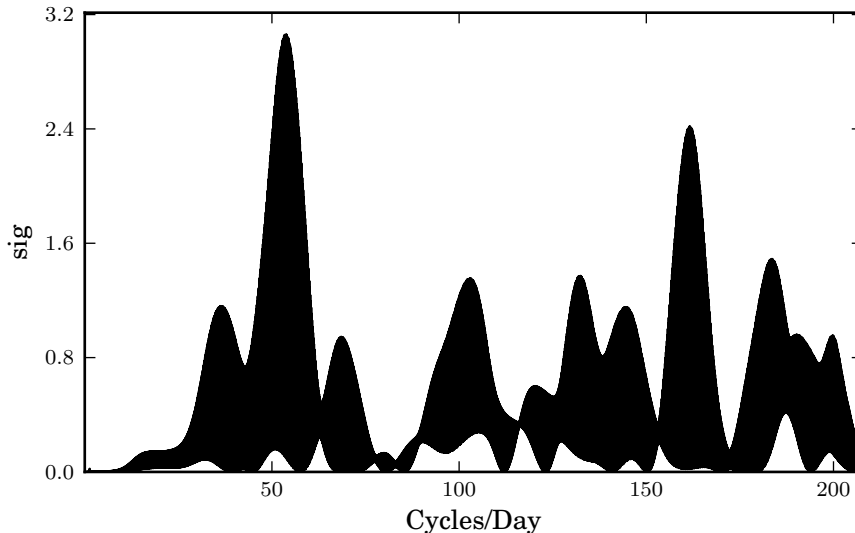
Figure 2.8 Significance spectrum of helium emission line flux ratios obtained from Keck-I/LRIS phase-resolved spectroscopy on 2011 March 4/12 (generated by SigSpec).

spectra, first developed by Nather et al. (1981), to establish the orbital period. Each spectrum was re-binned to the same wavelengths and the location of individual emission lines were identified. Because of the large number of cosmic rays on the red side despite processing with L.A. Cosmic (van Dokkum 2001), we concentrated on the blue side and used the helium lines at $4026\,\text{Å}$, $4387\,\text{Å}$, $4471\,\text{Å}$, $4686\,\text{Å}$, $4921\,\text{Å}$, and $5015\,\text{Å}$. The lines from each exposure were re-binned and co-added to produce a summed He emission line. We then subtracted the red 40% of the line from the blue 40% of the line, and divided by the continuum. This produced a time series of flux ratios, which we analyzed using SigSpec. We identified a period of $1606.2 \pm 0.9\,\text{s}$ with a "sig" of 3.1. The statistical significance spectrum is in Figure 2.8.

While not a very high confidence level, we believe the above period is, in fact, the orbital period, for two reasons. First, the period found is within the error bars of the previously discussed quiescent photometric period (see Section 2.3.3). Second, the movement of the disk's hotspot can be identified by creating a phase-binned, trailed spectrum of the He emission line. The rotation of the disk produces an "S-wave" that has been observed previously in known systems (e.g. Roelofs et al. 2005; Rau et al. 2010). In the case of PTF1J0719+4858, this S-wave is very weak, but still discernible. We present the trailed spectrum in Figure 2.9.

This is not the first system where the S-wave was difficult to detect. As reported in
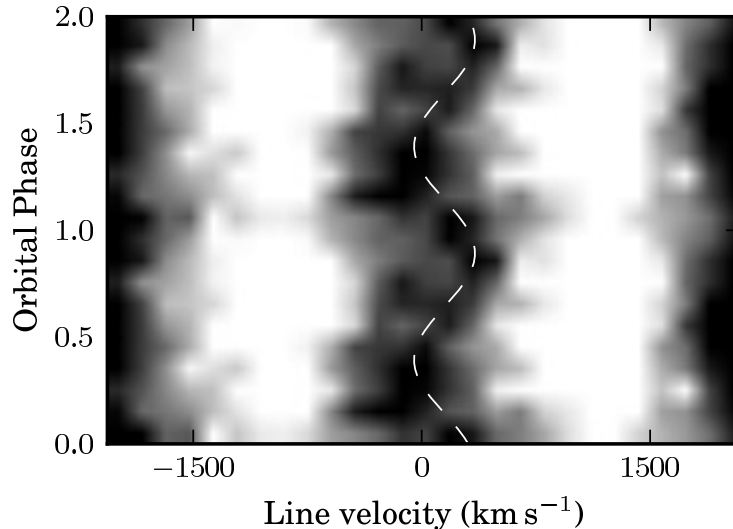
Figure 2.9 Phase-folded, trailed spectrum of the combined He emission lines visible on Keck-I/LRIS's blue CCD. The period is set to 1606.2 s. The "S-wave", marked by a dashed line, is faint but present. Variation in gray scale indicates relative flux densities. The two white columns are the double-peaked structure of the He emission lines. The start of the first night of observations, at HJD = 2455624.81212, was used as the zero phase.

Roelofs et al. (2009), an S-wave in SDSSJ0804+1616 was not found in one of two sets of spectra. Further observations are required to establish whether PTF1J0719+4858 has similar variability in the strength of the S-wave or if it is simply a weak feature.

2.5 Discussion

2.5.1 Comparison of Long-term Light Curve with that of Other AM CVn Systems

We broadly group the known outbursting AM CVn systems into two categories: those having super-outbursts that occur at least every three months and those with less frequent super-outbursts. The latter group has either poorly determined or undetermined recurrence times. We summarize their properties in Table 2.4.

It appears that these sources can be cleanly divided by orbital period, with the break between 1606 s and 1699 s. For the first group, the recurrence times are fairly well determined and appear to correlate with the orbital period. The second group is more difficult to understand, primarily due to a lack of known recurrence times. The one published recurrence time, for SDSSJ0926, is very poorly determined (Copperwheat et al. 2011). However, there

Table 2.4.   Properties of known outbursting AM CVn systems

Object	Orbital Period (s)	Super-outburst Recurrence Time (days)	Δmag	References
CR Boo	1471	46.3[a]	4.5	1, 2
KL Dra	1500	50	4.2	3
V803 Cen	1596	77	4.6	4, 5
PTF1J0719+4858	1606	65–80	3.5	this paper
SDSS J0926+3624	1699	104–449	3.3	6
CP Eri	1701	. . . [c]	3.2	7, 8
2003aw	2028	. . . [c]	4.8	9, 10
2QZ J1427-01	2194[b]	. . . [c]	5.3	11
SDSS J1240-0159	2241	. . . [c]	4.5	12, 13, 14
SDSS J0129+3842	2274[b]	. . . [c]	4.6	15, 16
SDSS J2047+0008	. . .	. . . [c]	~ 6	17

[a]Reported as 46.3 d in Kato et al. (2000), but reported as variable in Kato et al. (2001) based on additional data

[b]Superhump period

[c]These systems have no published recurrence time, but it is believed to be significantly longer than 3 months

References. — (1) Kato et al. (2000); (2) Kato et al. (2001); (3) Wood et al. (2002); (4) Nogami et al. (2004); (5) Roelofs et al. (2007b); (6) Copperwheat et al. (2011); (7) Abbott et al. (1992); (8) Groot et al. (2001); (9) Nogami et al. (2004); (10) Roelofs et al. (2006a); (11) Woudt et al. (2005); (12) Roelofs et al. (2005); (13) P. Woudt (2005, priv. comm.); (14) Shears et al. (2011); (15) Anderson et al. (2005); (16) Shears et al. (2011); (17) Anderson et al. (2008)

does appear to be a clear gap between the determined recurrence times of PTF1J0719+4858 and much more poorly determined recurrence time of SDSSJ0926+3624, and we question whether this difference in recurrence time is purely a result of the increased orbital period (and thus decreased mass transfer rates) or if different parameters also play a role (such as the mass of the primary and/or the entropy of the secondary).

We can draw parallels to the much more common CVs. The class of CVs most like outbursting AM CVn systems are the SU UMa-type CVs, which also exhibit both normal outbursts and super-outbursts with superhumps (Warner 1995). SU UMa-type systems typically have super-outburst recurrence times of several hundred days and orbital periods between 90 and 120 minutes (Osaki 1996), but have been found to have two extreme cases. The ER UMa-type systems have recurrence times between 19 and 45 days (Buat-Ménard & Hameury 2002), while WZ Sge-type systems have recurrence times of decades and lower orbital periods of 80–90 minutes. The long recurrence times of WZ Sge-type systems are explained by the lower mass transfer rates of WZ Sge-type systems, as a result of their more evolved state (CVs are believed to have negative $\dot{P}$, as opposed to AM CVn systems; Osaki 1996).

In Kato et al. (2000), CR Boo was proposed to be the helium equivalent of an ER UMa-type CV. However, given that all four of the frequently outbursting systems appear to have fairly similar behavior, we believe that this is typical behavior for AM CVn systems with these orbital periods, as opposed to an extreme case. On the other hand, the recurrence times of the longer period outbursting AM CVn systems indicate that these systems are more akin to the WZ Sge-type CVs. This is consistent with the assumption that AM CVn systems have positive $\dot{P}$ and thus have lower mass transfer with greater orbital periods. Additional discoveries of AM CVn systems, as well as better, more systematic observations of known systems, are necessary to understand the reality of the difference in recurrence times.

2.5.2   Origin of Photometric Variability in Quiescence

The high-cadence photometric observations discussed in Section 2.3.3 and labeled as HC3 were coincident with the phase-resolved spectroscopy discussed in Section 2.4.2, providing us with an opportunity to determine the source of the observed photometric variability. We present a binned, phase-folded photometric light curve in Figure 2.10, together
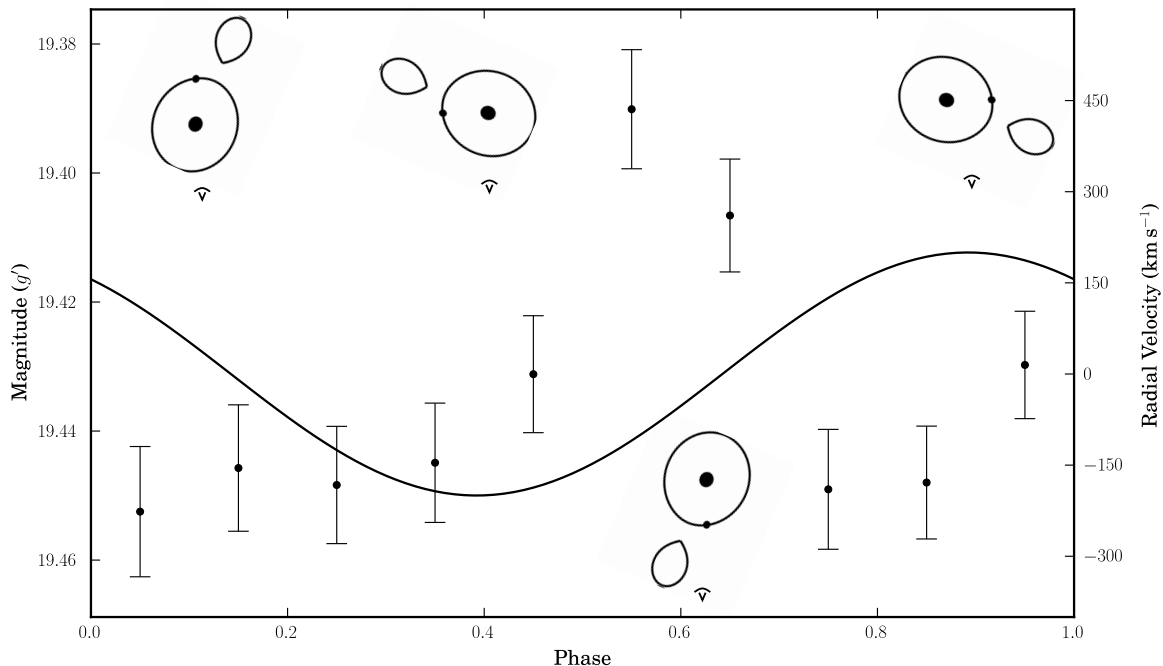
Figure 2.10 Phase-binned light curve taken on 2011 March 4 using the P60. Eighty-seven 60 s exposures were binned into 10 bins with a zero phase of HJD = 2455624.81212, the start of the phase-resolve spectroscopy, and the spectroscopically derived period of 26.77 minutes. Overplotted is the S-wave found in Section 2.4.2. The rough orientation of the binary is shown with drawings at the four extreme points of the orbit, along with the position of the observer.

We see that the increase in brightness is coincident with the radial velocity of the hot spot being roughly zero and the time period preceding it, indicating that the hot spot and the previously-heated disk edge are the likely source of the increased brightness.

with the radial velocity of the hot spot. The binning provides an increase in the signal-to-noise and gives a roughly 5σ detection. We remind the reader that HC3 was observed in quiescence, during which time superhumps are not believed to occur in either AM CVn systems or CVs.

The increase in brightness immediately follows the blueshifted portion of the radial velocity curve and is coincident with a lack of radial velocity. This indicates that the photometric variability in PTF1J0719+4858 is caused by the hot spot and the associated heated edge of the disk being closest to the observer (see drawings in Figure 2.10). We assume here that the S-wave is, in fact, caused by the hot spot.

AM CVn system variability in quiescence has been observed for other non-eclipsing systems such as CR Boo (Provencal et al. 1997) and KL Dra (Wood et al. 2002), but no study has been done of the origin. However, such studies for CVs have linked the hot spot

to the observed photometric variability (e.g. Schoembs & Hartmann 1983).

The concern with this explanation is the lack of precision in the photometric data and the lack of time resolution as a result of the binning. This also makes it difficult to compare Figure 2.10 to observations of other AM CVn systems or CVs. However, we believe that there is sufficient data to link the quiescent variability to the location of the hotspot relative to the observer.

2.5.3   Potential for Future Discoveries with PTF

How many additional AM CVn systems might be discovered by PTF? First, we estimate the fraction of all AM CVn systems that are outbursting. Consider a simple model of a single system's evolution by assuming that gravitational wave radiation and angular momentum loss from mass transfer are solely responsible for the evolution of the orbital period (Paczyński 1967; Nelemans et al. 2001). Then, using typical mass values for an AM CVn system at its minimum period ($0.6 M_\odot$ and $0.25 M_\odot$, although similar values do not significantly affect the results) we find that an AM CVn system spends $\sim 0.5\%$ of its life between orbital periods of 20 and 27 minutes (the frequent outbursters) and $\sim 3.3\%$ of its life between orbital periods of 27 and 40 minutes (the less frequent outbursters). We use these numbers as a simple estimate of the percentage of AM CVn systems that are outbursting.

We now estimate the number of systems PTF could discover. Given that AM CVn systems have outbursts with $\Delta \mathrm{mag} \gtrsim 3$, we conservatively assume that any outbursting system with a quiescent magnitude of $\lesssim 23$ can be detected in outburst by PTF. We assume a scale height of $300\,\mathrm{pc}$ (Roelofs et al. 2007d) and a scale length of $2.5\,\mathrm{kpc}$ (Sackett 1997) in the Galaxy and an AM CVn system space density of $\rho_o = 3.1 \times 10^{-6}\,\mathrm{pc}^{-3}$ (the observed space density based on pessimistic population models from Roelofs et al. 2007d). Given that the systems are in quiescence, we further assume that the accretor provides all of the system's luminosity, and use Equation (5) from Roelofs et al. (2007d), which is a parametrization of Figure 2 in Bildsten et al. (2006), to calculate the absolute magnitudes of the AM CVn systems. This likely means that our estimate is conservative since the disk is known to provide part of the luminosity ($\sim 30\%$ for SDSSJ0926+3624; see Marsh et al. 2007) in quiescence. We find that there are approximately $\frac{1.3\,\mathrm{systems}}{100\,\mathrm{deg}^2}$ with orbital periods between 20 and 40 minutes and at $20^\circ < |b| < 60^\circ$ (the galactic latitudes for most of PTF's observations). Given PTF's footprint of $10{,}000\,\mathrm{deg}^2$, we estimate that PTF might detect up

to 136 such systems. However, the uncertainty in the AM CVn system population density estimates likely means that this number is only accurate to within a factor of 10.

However, the apparent long-outburst recurrence times of longer-period systems will make these much more difficult to detect. If we consider only those systems with frequent outbursts and thus orbital periods between 20 and 27 minutes, we find that there are up to 18 such systems. Given the recurrence times of 45–80 days, the presence of normal outbursts in at least two systems, and the super-outburst duty cycle of 30%–50%, it is very likely that all 18 systems can be detected as part of the PTF transient search.

We note that searches in lower galactic latitudes make detection much more likely. The population distribution of outbursting AM CVn systems almost doubles between $20° < |b| < 25°$ and $15° < |b| < 20°$. Although the analysis of lower-latitude data is more difficult due to the larger number of sources overall, it still presents the best opportunity to discover a large number of AM CVn systems.

Despite the exciting possibilities of using synoptic surveys to search for outbursting systems with quiescent magnitudes up to $R \sim 23$–25 (and even deeper for future surveys), we caution that confirmation of these systems will be difficult. The established method for finding orbital periods is via phase-resolved spectroscopy, requiring large telescopes and short exposure times for even fairly bright objects. Even objects with a quiescent magnitude of $R \sim 23$ cannot be observed in such a fashion with today's telescopes. Instead, such systems can be observed in outburst. The hot spot has been observed in high state AM CVn systems (Roelofs et al. 2006b) and it is likely that it can be seen in the high state of outbursting systems as well. Additionally, as demonstrated with PTF1J0719+4858 and other AM CVn systems, photometric periods can be obtained from both superhumps and (potentially) in quiescence, providing a good estimate of the orbital period.

2.6 Summary

We have presented extensive photometric and spectroscopic observations of PTF1 J071912.13+485834.0. We have observed the system in both quiescence and outburst, observing the strong emission lines and a weak photometric period in the former, and absorption lines and detectable superhumps in the latter. From the phase-resolved spectroscopy, we have identified a weak, albeit detectable, signal in the spectrum that indicates

an orbital period of 1606.2 ± 0.9 s. These data have, in combination with the simultaneous high-cadence photometry, allowed us to determine the possible source of the quiescent photometric variability. We have also looked at the long-term light curve and found a variable super-outburst recurrence time, as well as regularly occurring normal outbursts. Based on the identified spectroscopic period, the double peaked emission lines in quiescence, and its photometric behavior, we classify PTF1J0719+4858 as an AM CVn system.

PTF1J0719+4858 has the longest orbital period of known, frequently outbursting AM CVn systems. We have calculated that PTF has the capability to significantly increase the number of such systems and potentially find many more systems with less regular outbursts. Additional discoveries would expand our understanding of both the structure and evolution of AM CVn systems and their population density.

Chapter 3

The Palomar Transient Factory Photometric Pipeline*

3.1   Introduction

The Palomar Transient Factory (PTF; Law et al. 2009; Rau et al. 2009) is a wide-area, synoptic, optical survey that uses the Palomar $48''$ Schmidt telescope. Each individual exposure covers $7.26\,\mathrm{deg}^2$ of the sky and typical exposure times are $60\,\mathrm{s}$. The cadences of the PTF survey are dependent on the active project, but are predominantly 3–5 days.

The PTF camera is composed of a set of eleven functioning CCDs. Two of these detectors are of a different composition than the remainder and are more sensitive to longer wavelengths. The PTF uses two primary filters: a Mould R filter and a SDSS g' filter. A separate Hα survey uses two narrowband filters. The majority of the PTF's observations are taken in the R filter.

At present, two pipelines process PTF exposures. The real-time transient pipeline uses difference imaging to detect new transient events (Gal-Yam et al. 2011) and prioritizes processing speed over photometric quality. In contrast, the photometric pipeline, discussed in this chapter, is targeted to the precise measurement of stellar sources. An overview of the PTF survey parameters is presented in Section 7.2.1.

3.2   The Image Processing Pipeline

The PTF IPAC Image Processing pipeline performs image-level processing and calibration on the raw images downloaded from the PTF camera. Here, I provide a brief overview of this process. A more detailed description will appear in Laher et al. (in prep).

Raw images must be calibrated using a bias and flat field. The former is generated from the average of a series of zero-second exposures taken at the beginning of each night. The

---

*A version of this chapter will appear as part of a future paper on the PTF photometric pipeline.

latter is generated combining all exposures taken on a given night and using a given filter after masking source detections. Astrometric calibration is performed using the SCAMP (Bertin 2006) package. In cases when SCAMP is not able to find an astrometric solution, a second attempt is made using the ASTROMETRY.NET (Lang et al. 2010) package.

Source detection and flux measurement is performed using the SEXTRACTOR package (Bertin & Arnouts 1996). Although the flux of each source is measured in several ways by SEXTRACTOR, the MAG_AUTO algorithm is used for all photometric calibration and scientific work. We note that this algorithm does not always pick the optimal aperture for fainter sources (Ofek et al. 2012) but is a good automated estimate for both point sources and extended sources in varying atmospheric conditions.

Absolute photometric calibration is performed relative to the SDSS photometric survey. Since the PTF often observes fields outside of the SDSS footprint, those fields observed on a given night by the PTF that are in the SDSS footprint are fit using time of night, airmass, and other parameters. This is then used to generate zero-points for each individual exposure. Full details are provided in Ofek et al. (2012). While this algorithm does provide a calibration good to 2–3%, it assumes stable photometric conditions and does not perform well on nights with variable conditions.

Each exposure is assigned several IDs and has several quality metrics calculated. Of particular importance for this discussion is the PTF pointing, composed of the filter (R or g'), field, and CCD (0–11, excluding 3) IDs. PTF fields are typically based on a tiled grid of the sky although specialized fields do exist for certain projects. Limiting magnitude calculations from the image processing pipeline are generated based on a theoretical estimate,

$$S_{lim} = \frac{\mathrm{SNR}^2 + \mathrm{SNR} \times \sqrt{4\pi f_{bkg} G\alpha(1.25s)^2 + 4N_{read}^2 + \mathrm{SNR}^2}}{2\alpha G} \tag{3.1}$$

$$M_{lim} = \mathrm{ZP} - 2.5 \log_{10} \frac{S_{lim}}{t_{exp}}, \tag{3.2}$$

where SNR is the desired signal-to-noise ratio limit of detection, f_{bkg} is the median background flux, G is the detector gain, α is set to 0.97 and is the fraction of a Gaussian point spread function (PSF) within 1.25FWHM, s is the seeing in arcseconds, N_{read} is the read noise of the detector, ZP is the zero point of the exposure (in magnitudes), and t_{exp} is the exposure time. S_{lim} is the flux limit of detection while M_{lim} is the corresponding limiting

magnitude. While this limiting magnitude measurement works well for images with a correct zero-point, it can be invalid if the zero-point is poorly calculated, as is often the case for exposures in poor conditions.

3.3   Source Detection Matching and Reference Catalogs

The Image Processing Pipeline (Section 3.2) operates at the exposure level. For studying the time variability of sources, light curves must be constructed. This requires matching detections of the same astrophysical source on multiple exposures and applying a relative photometric calibration.

3.3.1   Reference Image Generation

Source detection matching is performed by co-adding exposures to construct a "reference" image and catalog. Reference images are generated from the best exposures at each PTF pointing. We select these exposures by first removing any exposure with seeing $>4''$, a missing or atypical absolute zero point calibration (as defined by the color terms in the fit; see Ofek et al. 2012), or a theoretical limiting magnitude brighter than 20.

We require that the limiting magnitude of the co-added image generated from the remaining exposures be at least 21.7. This limiting magnitude is generated from Equation 3.2, but substituting the sum of the individual-exposure background levels, the mean of the seeing estimates, and the sum of the individual zero-points (converted first into flux) for the appropriate values. The co-addition is performed by calibrating the astrometry of each exposure relative to the other exposures (as opposed to an external catalog) using SCAMP (Bertin 2006), removing spherical distortion from each image using SWARP (Bertin et al. 2002) such that one pixel in either axis is one arcsecond on the sky, and co-adding the exposures using a weighted mean. Bad pixels are masked for each individual exposure prior to co-addition, and each exposure is scaled to a reference zero-point. Source detection and flux measurement on the generated images is performed using SEXTRACTOR (Bertin & Arnouts 1996). An example of a reference image vs. an individual exposure is shown in Figure 3.1.

Few PTF fields have sufficient exposures to construct a reference image with a depth significantly fainter than $R \sim 23.5$. In Figure 3.2, we show the number of images necessary

Figure 3.1 A comparison of a single PTF exposure (left) taken in very good conditions with a theoretical limiting magnitude of 21.7 and a reference image (right) of the same field with a theoretical co-added limiting magnitude of 23.0. A significantly larger number of sources are visible on the reference image.

to obtain a reference image to a particular depth.

3.3.2 Source Detection Matching

Source detection matching is performed by comparing the sources detected on an individual exposure to the reference catalog for that pointing. We refer to the individual sources in the reference catalog as reference sources. The closest detection on an individual exposure within $1.5''$ of a reference source is matched to the source. If a detection is not matched to a reference source, it is marked as a "transient" source and linked to any previously detected transient source within $1.5''$. We show the scatter of position measurements in a typical PTF field in Figure 3.3.

We note that this process is not perfect. Two issues in particular have been frequently noticed with de-blending of close astrophysical sources by SEXTRACTOR. For areas with several close sources, changing seeing conditions between exposures will result in SEXTRACTOR treating two or more close sources either as a single source or as individual sources. In this case, the light curve of such sources will typically show two magnitudes. One is from the exposures where the sources are combined and one is from exposures where the seeing is good enough to differentiate the sources.
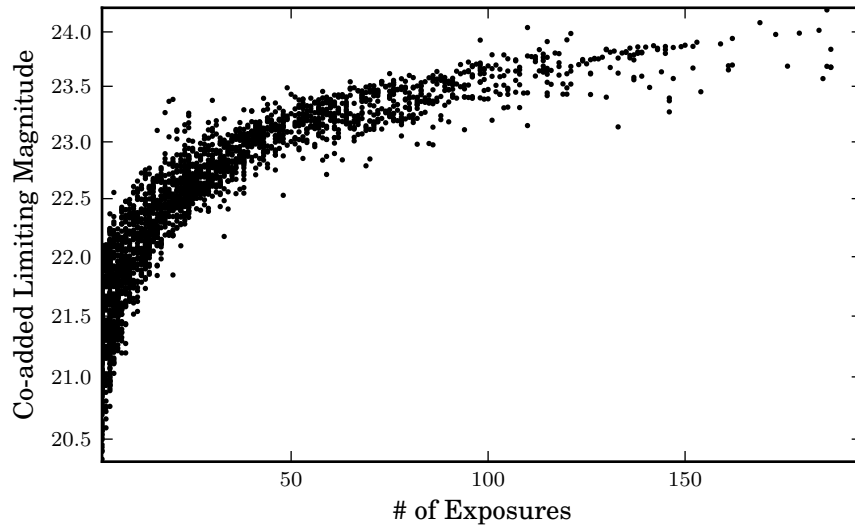
Figure 3.2 The limiting magnitude of a reference images versus the number of exposures used to make the reference image. This is different from the total number of exposures for a particular field and does not include exposures with poor calibrations. The majority of PTF fields have fewer than 60 exposures.
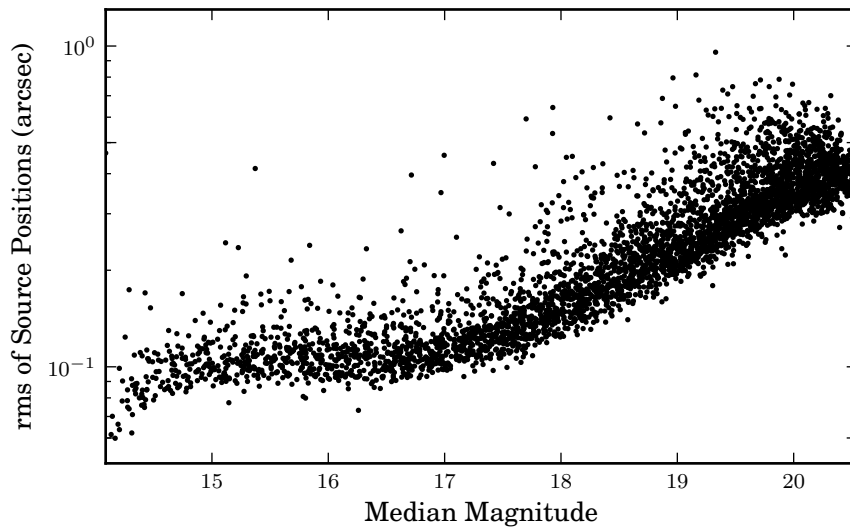
Figure 3.3 The rms of source positions measured for individual sources on a typical field vs. median magnitude of the source. Precision is $\sim 0.1''$ at the bright end and approaches $0.5''$ at the faint end. Source matching is performed with a radius of $1.5''$.

The second significant issue occurs when a relatively faint source is within few arcminutes of a saturated star. Often, the faint star is not detected by SEXTRACTOR as a separate source on the reference catalog, but is detected as a separate source on individual exposures. It is thus treated as a transient by the matching pipeline. Although increasing the aggressiveness of the de-blending algorithm results does fix such problems, it also significantly increases the number of fake sources identified.

3.4 Relative Photometry

Once light curves are constructed, we can calculate relative photometric corrections for each exposure taken of a particular PTF pointing. The algorithm used is based on that presented in Section 2.3.1. Here, we describe the additional steps taken to identify calibration sources for each PTF pointing and the procedure used to remove any negative effects on the calibration due to exposures taken in poor conditions.

We perform relative photometric calibration on each individual pointing separately. Although flux measurements of the same source taken on different CCDs appear to have differences of less than 1%, we do not yet perform a global calibration that corrects for any differences in the response of each individual CCD.

Calibration of a pointing begins with the separation of "good" exposures from "bad" exposures. Bad exposures are those with no absolute photometric calibration, fewer than half of the median number of sources from all exposures of the pointing, or with a high systematic error. We define the systematic error to be the robust standard deviation of the residuals of the measurements of bright sources ($14.3 < m < 15.8$) from the median magnitude based on all exposures. We define the robust standard deviation to be $0.741(75^{\text{th}}\text{percentile} - 25^{\text{th}}\text{percentile})$. The high systematic error for each pointing is the smallest value of n for which at least half of exposures have systematic errors below (0.01×2^n) mag. For most pointings, the high systematic error is 0.01.

Calibration sources are selected by identifying the brightest 400 sources that have detections in all good exposures. We calculate the zero-points for the good exposures by using the aforementioned relative photometry algorithm in an iterative fashion so as to remove sources with variability in their light curves (whether real or fake). For each iteration, we apply the newly-calculated zero-point offsets to the measurements on each exposure, con-
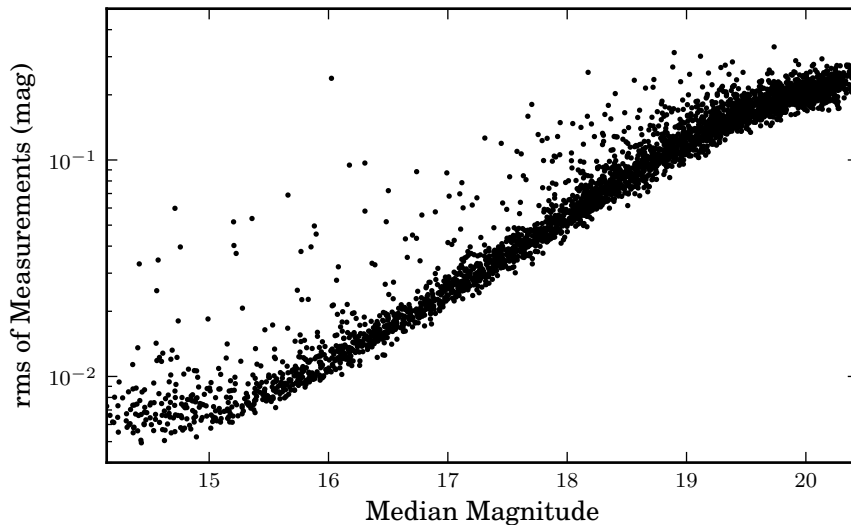
Figure 3.4 The photometric performance of a typical pointing for PTF in the R-band filter (g'-band performance is similar). The systematic limit is <1% at $R \sim 14.5$ and photometry at the faint end has an error of $\sim 0.2\,\mathrm{mag}$.

struct light curves of the calibration sources, and, for each $0.2\,\mathrm{mag}$ bin, remove any sources with a photometric rms of $>3\sigma$ as compared to other sources in the bin. This process typically removes 10–20% of sources.

The calibration sources selected by the iterative process are then used to generate a final set of relative zero-point corrections and mean magnitudes for the sources. Bad exposures are calibrated by fixing the value of the mean magnitudes and only finding the zero-point corrections. This ensures that the best calibration is found for the good exposures while still calibrating all exposures. We do not apply any de-trending to the exposures but do include a reference magnitude, which is the median photometrically-calibrated magnitude of each source. Final measurement errors are calculated by combining the measurement error provided by SEXTRACTOR, the error of the fit (typically zero), and the systematic error of each exposure.

A fairly typical example of the photometric performance is presented in Figure 3.4. This algorithm provides precision of 6–8 mmag at the bright end and corrects for the poor performance of the absolute photometric calibration algorithm in poor weather. Performance is consistent across all pointings, and is discussed further in Section 7.2.1.2.

The calibration algorithm is implemented in CYTHON[1] with data storage in PYTABLES[2].

---

[1] http://www.cython.org
[2] http://www.pytables.org

The large amount of data precludes processing completely in memory. The least-squares-fit solutions for the relative photometry calibration are found using a sparse algorithm as implemented in the SCIPY.SPARSE.LINALG.LSQR package[3].

3.5 Conclusions

The PTF photometric pipeline provides well-calibrated light curves over a large area of the sky using fully automated absolute and relative photometric calibration algorithms. Despite the lack of an all-sky photometric survey and ever-changing weather conditions, the combination of these calibrations is able to provide high-quality data. The next significant improvement will be the inclusion of PSF flux measurements, which should both remove some of the artifacts from aperture photometry, and allow the PTF to probe $\sim 0.5\,$mag deeper.

---

[3]`http://www.scipy.org`

Chapter 4

Five New Outbursting AM CVn Systems Discovered by the Palomar Transient Factory[*]

David Levitan[1], Thomas Kupfer[2], Paul J. Groot[1,2], Shrinivas R. Kulkarni[1], Thomas A. Prince[1], Gregory V. Simonian[1], Iair Arcavi[3], Joshua S. Bloom[4], Russ Laher[5], Peter E. Nugent[4,6], Eran O. Ofek[3],Branimir Sesar[1], and Jason Surace[5]

[1] Division of Physics, Mathematics, and Astronomy, California Institute of Technology, Pasadena, CA 91125, USA.

[2] Department of Astrophysics/IMAPP, Radboud University Nijmegen, PO Box 9010, NL-6500 GL Nijmegen, the Netherlands.

[3] Department of Particle Physics and Astrophysics, Weizmann Institute of Science, Rehovot, 76100, Israel.

[4] Department of Astronomy, University of California, Berkeley, CA 94720-3411, USA.

[5] Spitzer Science Center, MS 314-6, California Institute of Technology, Pasadena, CA 91125, USA.

[6] Computational Cosmology Center, Lawrence Berkeley National Laboratory, 1 Cyclotron Road, Berkeley, CA 94720, USA.

Abstract

We present five new outbursting AM CVn systems and one candidate discovered as part of an ongoing search for such systems using the Palomar Transient Factory (PTF). This is the first large-area, systematic search for AM CVn systems using only large-amplitude photometric variability to select candidates. Three of the confirmed systems and the candidate system were discovered as part of the PTF transient search. Two systems were found as part of a search for outbursts through the PTF photometric database. We discuss the observed characteristics of each of these systems, including the orbital periods of two systems. We also consider the position of these systems, selected in a color-independent survey, in color-color space and compare to systems selected solely by their colors. We find that the colors of our newly discovered systems do not differ significantly from those of previously known systems, but significant errors preclude a definitive answer.

4.1 Introduction

AM CVn systems are rare, ultra-compact, semi-detached white dwarf binaries with periods ranging from 5 to 65 minutes. First proposed as a class of binary systems over 40 years ago by Smak (1967), fewer than ten additional systems were discovered in the following 30 years. The availability of wide-area surveys – first photometric, then spectroscopic, and now synoptic – has resulted in the discovery of over 20 systems in just the last decade, yet their rich and complex phenomenological behaviour and evolutionary history has limited our understanding of these degenerate post-period minimum binaries. AM CVn systems are believed to be one possible outcome of double degenerate white dwarf evolution, along with R CrB stars, massive single white dwarfs, and type Ia supernovae (Webbink 1984; Nelemans et al. 2001). They are extremely important as strong low-frequency Galactic gravitational wave sources (e.g., Nelemans et al. 2004; Roelofs et al. 2007d; Nissanke et al. 2012) and are the source population of the proposed ".Ia" supernovae (Bildsten et al. 2007). However, the lack of an accurate population density has complicated their use for understanding these phenomena. We refer the reader to Nelemans (2005) and Solheim (2010) for general reviews.

The first 11 AM CVn systems were serendipitous discoveries. Several were initially of interest as supernova candidates (e.g., Jha et al. 1998; Wood-Vasey et al. 2003). The avail-

ability of the Sloan Digital Sky Survey (SDSS) and, specifically, its spectroscopic database, led to the first systematic search for AM CVn systems and yielded 7 new systems based on their distinctive helium emission lines and lack of hydrogen (Roelofs et al. 2005; Anderson et al. 2005, 2008). However, the SDSS spectroscopic database is not complete and spectroscopic targets are selected based on complex color criteria and fiber availability. Roelofs et al. (2009) noticed that the known AM CVn systems are clustered in a relatively sparse area of the color-color space and proposed a spectroscopic survey of all SDSS sources inside a pre-determined color cut. Although predictions of up to a total of 50 systems in the SDSS were made (based on Roelofs et al. 2007d), the survey, now wrapping up, has found fewer than 10 additional systems (Roelofs et al. 2009; Rau et al. 2010; Carter et al. 2013a).

Although successful, such color-selected spectroscopic surveys are both resource intensive and inherently biased to the previously known population. AM CVn systems have similar colors to other blue objects, including white dwarfs (particularly DB white dwarfs) and QSOs. Expanding the color selection to a wider box appears to offer a significant increase of the number of candidates with few gains in the number of discovered AM CVn systems. A way to further down-select candidates, or completely change the selection criteria, is thus necessary.

AM CVn systems are thought to have distinctly different phenomenology dependent on their orbital periods. Believed to be binaries hosting degenerate mass donors that have evolved through a period minimum, their orbital periods increase as angular momentum is lost to gravitational wave radiation. The most recently formed systems, with periods below $\sim 20\,\mathrm{min}$, are in a constant state of high mass transfer from the donor to the optically thick accretion disc. They have been referred to as "high" state systems and exhibit properties similar to dwarf novae cataclysmic variables in outburst, including superhumps and absorption line spectra (e.g., Roelofs et al. 2006b, 2007b; Fontaine et al. 2011a).

The oldest systems – those with orbital periods over $\sim 40\,\mathrm{min}$ and thus low mass transfer rates – are characterized by their lack of photometric variability and strong helium emission lines from the optically thin disc. Spectroscopic surveys are primarily sensitive to systems with these emission lines.

Between these two extremes are the "outbursting" systems, thought to have orbital periods between roughly 20 and 40 minutes. These systems are characterized by their changes between a high state and a low state, which results in both a luminosity change

of 3–5 magnitudes and (typically) a change in the spectral features from absorption lines to emission lines. In each state, they generally take on the properties of that state, with the significant addition of photometric variability in the low state for some of the systems. This variability was tied to the orbital period by Levitan et al. (2011), but any link between the photometric and spectroscopic variability remains to be confirmed by observations of additional systems. Outbursts typically last on the order of days to weeks, and are recurrent on timescales of a few months to over a year (Kato et al. 2000; Ramsay et al. 2012). Large-area synoptic surveys are most sensitive to these outbursting systems and the first system from such a survey was reported by Levitan et al. (2011) using the Palomar Transient Factory (PTF; Law et al. 2009).

In this paper, we continue the survey work started in Levitan et al. (2011) and report on the discovery of an additional five AM CVn systems and one faint candidate as part of the PTF AM CVn System Key Project. This search is the first systematic, large-area color-independent search for AM CVn systems that relies solely on their large-amplitude, photometric variability to identify candidates.

We introduce the PTF in Section 5.2 and describe our AM CVn system detection strategy and data reduction processes. We report on our discoveries in Section 4.3, including both photometric measurements of the individual systems and period analysis based on phase-resolved spectroscopy. In Section 4.4 we discuss the features of these systems and compare their colors to the color selection criterion used in the aforementioned spectroscopic survey.

4.2   Source Detection and Analysis Process

The PTF[1] uses the Samuel Oschin 48″ Schmidt telescope at the Palomar Observatory to image up to $\sim$2,000 deg^2 of the sky per night to a median depth on dark nights of $R\sim$20.6 or $g'\sim$21.3 (Law et al. 2009; Rau et al. 2009). The cadence of observations is not uniform and has varied from 90 s to 5 d, depending on the observational program conducted at the time.

Two pipelines process PTF data. The "transient" pipeline uses difference imaging for the rapid discovery of transient events. Exposures are automatically reduced and processed

---

[1]http://www.astro.caltech.edu/ptf

within a few hours of acquisition and candidate events, identified using difference photometry, are analysed by both automated routines and humans (Law et al. 2009). Conversely, the "photometric" pipeline is designed for accuracy, not speed. In this pipeline, exposures are processed after the end of the night using aperture photometry (Laher et al. in prep). Instrumental magnitudes are calibrated to SDSS and instrumental effects, airmass, and background are de-trended (Ofek et al. 2012). Finally, light curves are generated using relative photometry algorithms (Levitan et al. in prep). From this photometric database, we select sources for follow-up observations. Most sources selected as part of this search were identified as cataclysmic variables (CVs) and are detailed in Groot et al. (in prep).

We refer to the AM CVn systems presented in this paper as either "transient" discovered or "photometrically" discovered. The former are those initially selected as supernova candidates and classified as part of the PTF supernova search. "Photometrically" identified systems were found by scanning through light curves for outbursts. These systems were selected by searching for outbursts of 2 mag above the median magnitude that have a second measurement at least 1 d later that is 5σ brighter than the median.

4.2.1   Data Reduction Procedures

All PTF light curves presented in this paper were processed through the photometric pipeline referred to earlier. The relative photometry algorithm used for the data in this paper (both PTF and targeted observations) is a matrix-based least squares algorithm. The algorithm was described briefly in Ofek et al. (2011) and Levitan et al. (2011). Further details and the specific application to the PTF data will be in Levitan et al. (in prep). We note that the systematic uncertainty limit of the PTF relative photometry is approximately 6–8 mmag (based on bright stars with $14.5 < m_R < 16$). Errors of $\sim$0.1 mag are achieved at $m{\sim}19$ and $\sim$0.2 mag at $m{\sim}21$.

The spectroscopic data were reduced using either standard IRAF tasks or using optimal extraction (Horne 1986) as implemented in the PAMELA code (Marsh 1989) as well as the STARLINK packages KAPPA, FIGARO, and CONVERT. The spectra acquired for the phase-resolved spectroscopy were all reduced using the latter. Spectra obtained from the red side of Keck-I/LRIS were processed with L.A. COSMIC (van Dokkum 2001) due to the large number of cosmic rays. Photometric data from the Palomar 200″ (P200) and the Nordic Optical Telescope (NOT) were reduced using standard bias-subtraction and flat-

fielding techniques. PSF photometry as implemented in either DAOPHOT or AUTOPHOTOM was used for measurements and absolute calibration was done by comparing with SDSS measurements in the same filter.

4.2.2 Period Analysis

For two of the systems, we attempted to measure the orbital period by looking for the "S-wave" using the method in Nather et al. (1981). The short orbital periods of AM CVn systems require short exposures, and, for these faint systems, 5–10 h of time on a 8–10 m telescope. The S-wave is thought to be caused by the orbital motion of the accretion disc bright spot, formed by the impact of transferred mass hitting the disc (e.g., Warner 1995). For each spectrum obtained, we summed the flux for $1000 \, \mathrm{km \, s^{-1}}$ on either side of the strongest lines and divided the two measurements. These set of ratios were analysed for each system using a Lomb-Scargle periodogram as implemented in Richards et al. (2011).

The verification of the orbital period was done in two ways. First, the strongest emission lines were co-added for each individual spectrum and converted into a trailed, phase-binned spectrum. This is essentially a two-dimensional representation with wavelength/velocity on one axis and time/phase on the other. In this image, we expect to see a sinusoidal S-wave from the hotspot on top of the disc emission as a result of Doppler shift. The particular lines used varied for each system.

To further verify the orbital period, we transformed the phase-binned spectrum into a Doppler tomogram (Marsh & Horne 1988). Doppler tomograms are essential in the study of semi-detached systems since they concentrate orbital velocity variations in a single location on a velocity map. The phase, radial velocity, and intensity data were used to produce an image in (K_x, K_y) velocity space. $(K_x, K_y) = (0, 0)$ is the location of the centre of mass. For semi-detached systems, four components are typically seen:

1. The accretor. For AM CVn systems, the absorption line features of the accretor itself are masked by the emission lines from the accretion disc and thus not visible in the Doppler tomogram. However, a narrow emission line feature referred to as the "central spike" is visible on some typically longer-period systems and is believed to be on or near the accretor (see e.g., GP Com; Morales-Rueda et al. 2003). The extreme mass ratio of AM CVn systems results in the accretor having a low velocity.

2. The accretion disc will extend from a relatively low velocity corresponding to the Keplerian orbital velocity of the outer edge of the disc to the much higher Keplerian orbital velocity at the radius of the white dwarf.

3. The donor star will have a lower velocity than the outer edge of the accretion disc. From Keplerian orbital mechanics,

$$v_{\mathrm{don}} = \left(\frac{2\pi G}{P_{\mathrm{orb}}}\right)^{1/3} \sqrt{\frac{M_{\mathrm{acc}}}{(M_{\mathrm{acc}} + M_{\mathrm{don}})^{1/3}}},$$

where v_{don} is the velocity of the donor, G is the gravitational constant, P_{orb} is the orbital period of the system, M_{acc} is the mass of the accretor, and M_{don} is the mass of the donor. If we set, for example, $M_{\mathrm{acc}} = 0.85 M_\odot$ and $M_{\mathrm{don}} = 0.035 M_\odot$, as found for the eclipsing AM CVn system SDSSJ0926+3624 in Copperwheat et al. (2011), we find that $v_{\mathrm{don}} \approx 700\,\mathrm{km\ s}^{-1}$. However, the donor is typically not seen in AM CVn systems due to its much lower luminosity relative to the accretor and disc. The sole exception thus far is the $5.4\,\mathrm{min}$ orbital period system HM Cnc (Roelofs et al. 2010).

4. The hotspot is expected to be on the inner edge of the accretion disc on the Doppler tomogram, at a relatively constant velocity. The location relative to the accretor is dependent on the size of the disc, but, for longer-period systems, is typically on the opposite side of the centre of mass in (K_x, K_y) space. The identification of a well-defined hotspot in the Doppler tomogram is a requirement to establish the orbital period (e.g., Roelofs et al. 2006b).

4.3   AM CVn Systems

We summarize the newly discovered AM CVn systems in Table 4.1. Hereafter, we will refer to all systems using the shorter PTF1JHHMM+DDMM convention as opposed to their full coordinates[2]. All observations are summarized in Table 5.1. The PTF light curves for all discovered systems are in Figure 4.1. We determined that these systems are AM CVn systems based on the presence of helium, the lack of hydrogen, and the observed outbursts.

---

[2]Non-transient sources in PTF are identified using the conventional IAU name format in the PTF1 catalog, a preliminary version of the final PTF catalog. This is different from the PTF transient convention that identifies events by the year and a character sequence.

Table 4.1. PTF-discovered AM CVn system properties

System	Discovery Pipeline	Period (min)	Outburst Mag[a]	Quiescent Magnitudes			
				u'	g'	r'	i'
PTF1 J043517.73+002940.7[b]	Transient[c]	34.31 ± 1.94	18.4 (R)	22.14 ± 0.11	22.28 ± 0.04	22.45 ± 0.04	22.60 ± 0.10
PTF1 J085724.27+072946.7	Transient[c]	⋯	19.5 (R)	21.68 ± 0.02	21.68 ± 0.01	21.74 ± 0.02	21.74 ± 0.04
PTF1 J094329.59+102957.6	Photometric	30.17 ± 0.65	16.9 (R)	20.51 ± 0.01	20.71 ± 0.01	21.09 ± 0.02	21.17 ± 0.05
PTF1 J152310.71+184558.2	Transient[c]	⋯	17.6 (R)	23.28 ± 0.12	23.48 ± 0.05	23.34 ± 0.06	23.14 ± 0.08
PTF1 J163239.39+351107.3[b,d]	Transient[c]	⋯	17.9 (g')	22.74 ± 0.14	22.99 ± 0.07	22.98 ± 0.06	⋯
PTF1 J221910.09+313523.1	Photometric	⋯	16.2 (g')	20.50 ± 0.03	20.66 ± 0.06	20.90 ± 0.03	20.94 ± 0.02
PTF1 J071912.13+485834.0[e]	Transient	26.77 ± 0.02	15.56 (g')	⋯	⋯	⋯	⋯

Note. — Quiescent magnitudes are from P200/LFC images and are not de-reddened.

[a]This is the brightest detection in PTF in either R or g' but is likely not the actual peak magnitude.

[b]Also identified as a CV candidate by the Catalina Real-Time Transient Survey (Drake et al. 2009): PTF1J0435+0029 = CSS090219:043518+00294; PTF1J1632+3511 = CSS110507:163239+351108.

[c]PTF transient names: PTF1J0435+0029 = PTF11avm; PTF1J0857+0729 = PTF11aab; PTF1J1523+1856 = PTF10noc; PTF1J1632+3511 = PTF11dkq.

[d]This is an AM CVn system candidate. See discussion in Section 4.3.5.

[e]Originally published in Levitan et al. (2011). Included here for reference as a PTF-discovered AM CVn system.

Table 4.2.   Details of observations of PTF-discovered AM CVn systems

System	Setup	UT Date	State	Gratings/Grisms	Exp. Time (s)
PTF1J0435+0029	P200/DBSP	2011 Mar 10	Outburst	B: 600/4000, R: 158/7500	600
...	Keck-I/LRIS	2011 Mar 12	Outburst	B: 400/3400, R: 400/7500	800
...	Keck-I/LRIS	2011 Mar 26	Quiescence	B: 400/3400, R: 400/7500	1080
...	Keck-I/LRIS	2011 Oct 29[a]	Quiescence	B: 600/4000, R: 600/7500	$180\,\mathrm{s}\times81$
...	P200/LFC	2012 Nov 22	Quiescence	Imaging (u', g', r', i')	480, except u' : 900
PTF1J0857+0729	KPNO 4-m/RC	2011 Feb 01[a]	Outburst	316/4000	1800
...	NOT/ALFOSC	2011 Feb 02	Outburst	#11 (200/5200)	120
...	P200/LFC	2011 Nov 30	Quiescence	Imaging (g')	$45\,\mathrm{s}\times80$
...	NOT/ALFOSC	2012 Feb 28	Quiescence	Imaging (g')	$60\,\mathrm{s}\times110$
...	P200/LFC	2012 Nov 22	Quiescence	Imaging (u', g', r', i')	300, except u' : 600
PTF1J0943+1029	Keck-I/LRIS	2011 Oct 29	Quiescence	B: 600/4000, R: 600/7500	1200
...	Keck-I/LRIS	2011 Dec 25[a]	Quiescence	B: 600/4000, R: 600/7500	$180\,\mathrm{s}\times80$
...	Keck-I/LRIS	2011 Dec 31[a]	Quiescence	B: 600/4000, R: 600/7500	$180\,\mathrm{s}\times25$
...	P200/LFC	2012 Nov 22	Quiescence	Imaging (u', g', r', i')	300, except u' : 600
PTF1J1523+1845	Keck-I/LRIS	2010 Jul 07	Outburst	B: 400/3400, R: 400/7500	200
...	Keck-I/LRIS	2010 Jul 08[a]	Outburst	B: 400/3400, R: 400/7500	300
...	P200/LFC	2012 Jan 30	Quiescence	Imaging(u', g', r', i')	360, except u' : 540
PTF1J1632+3511	Keck-II/DEIMOS	2011 Jul 05[a]	Unknown	600ZD (600/7500)	900
PTF1J2219+3135	Keck-I/LRIS	2011 Nov 25[a]	Quiescence	B: 400/3400, R: 400/7500	1200
...	P200/LFC	2012 Nov 22	Quiescence	Imaging (u', g', r', i')	300, except u' : 600

[a]Indicates that this exposure (or the co-add of the exposures) is shown in this paper.

Note. — The following is a list of used telescopes/instruments:

P200/DBSP: Palomar 200″ telescope with the Double Spectrograph (Oke & Gunn 1982).

Keck-I/LRIS: Keck-I 10-m telescope with the Low Resolution Imaging Spectrometer (Oke et al. 1995; McCarthy et al. 1998).

KPNO 4-m/RC: KPNO 4-m Mayall telescope with the RC Spectrograph.

NOT/ALFOSC: 2.5-m Nordic Optical Telescope with the Andalucia Faint Object Spectrograph and Camera.

P200/LFC: Palomar 200″ telescope with the Large Format Camera.

Keck-II/DEIMOS: Keck-II 10-m telescope with the Deep Imaging Multi-Object Spectrograph (Faber et al. 2003)
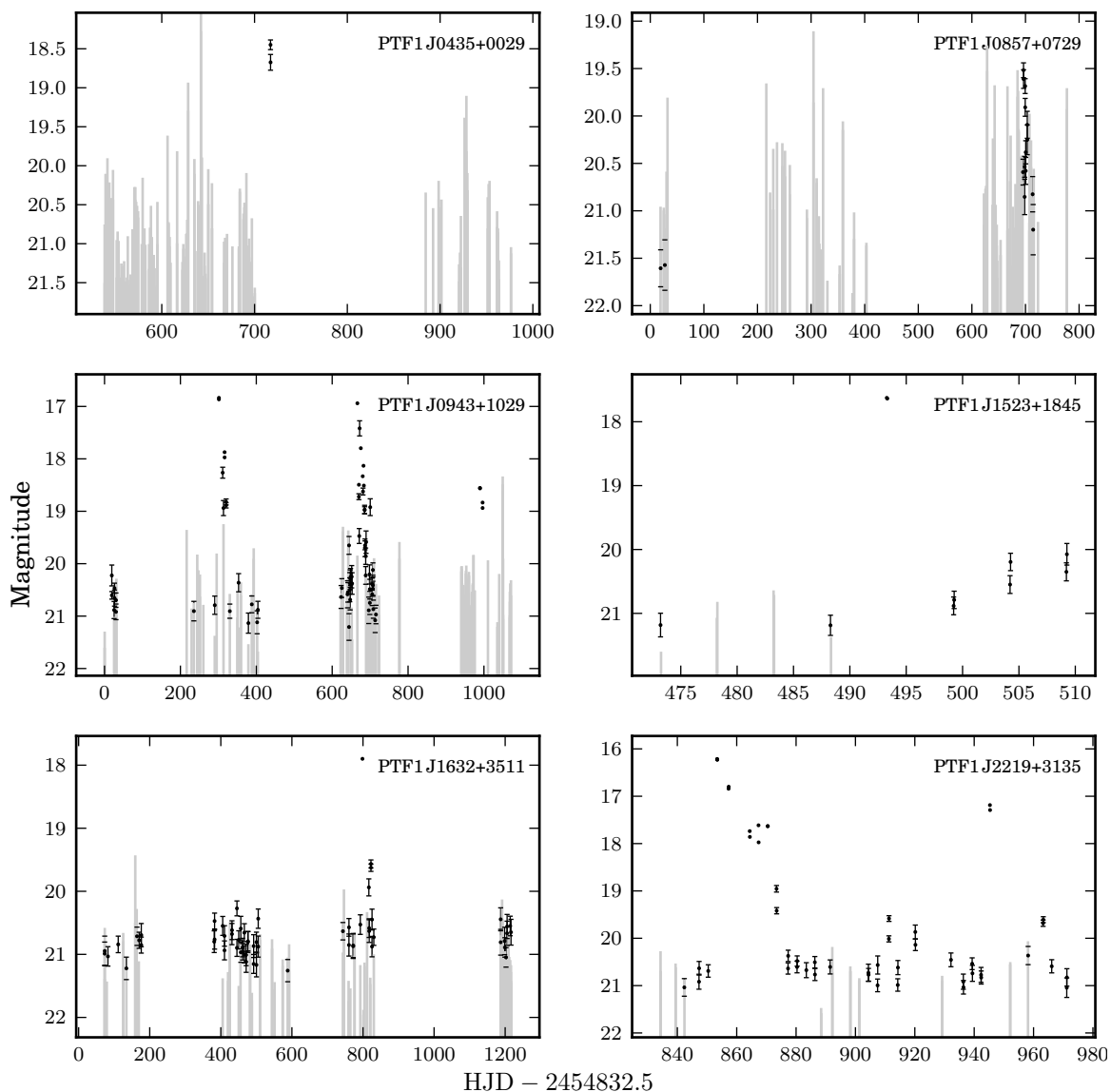
Figure 4.1 Light curves of all systems presented here. All data are from the PTF photometric pipeline. Error bars are shown for those observations with errors >5%. Non-detections are indicated using gray lines – the top of the line is the 3σ limiting magnitude as derived from the seeing, background, and CCD characteristics. Dates shown are relative to 01 Jan 2009. All data taken for each system by the PTF are shown except for PTF1J1523+1845, for which there were 12 prior non-detections to limiting magnitudes of ~21 over the 400 days before the data shown. We do not differentiate between R and g' data here, although the vast majority is R.
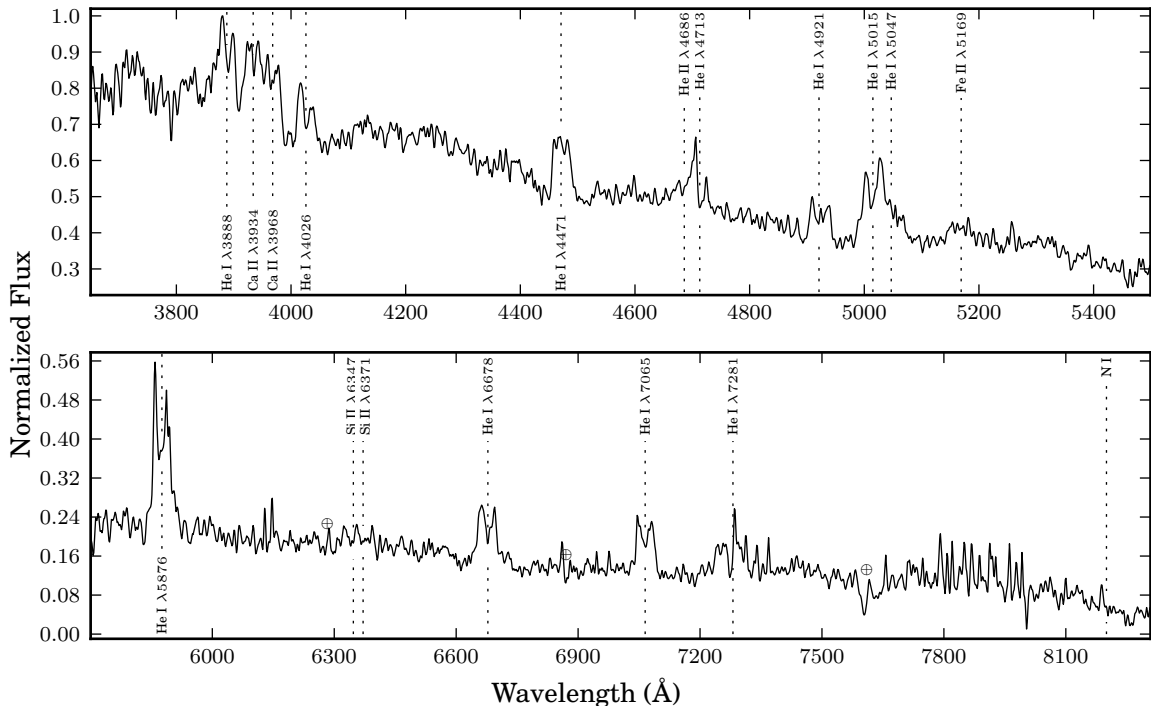
Figure 4.2 A spectrum of PTF1J0435+0029 obtained from the ∼4 h of co-added exposures of 2011 Oct 29.

4.3.1   PTF1 J043517.73+002940.7

PTF1J0435+0029 was detected in outburst by the transient pipeline on 2011 Feb 16 and identified as a candidate of interest by the Galaxy Zoo Supernovae project (Smith et al. 2011). Only two detections were made as the field was not observed again until the following season. Follow-up classification spectra on 2011 Mar 10 and 2011 Mar 12 showed a mostly featureless continuum spectrum. However, a spectrum taken on 2011 Mar 26 showed helium emission lines consistent with those of known AM CVn systems.

On 2011 Oct 29, we obtained 5.18 h of phase-resolved spectroscopy. We present the co-added spectrum in Figure 4.2. We analysed this data as described in Section 4.2.2 and present the periodogram of the flux ratios in Figure 4.3. The periodogram shows a peak at 34.31 min, but one that is broad due to the short baseline. The uncertainty of period measurement was estimated using a simple Monte Carlo simulation. For each iteration of the simulation, we selected 105 exposures at random, allowing for repetition, and calculated the periodogram. We estimate the error to be 1.94 min which is the standard deviation in the period estimates of 1000 such iterations. This is consistent with the FWHM of the

peak, which is 1.75 min. The more complicated error estimate used for PTF1J0943+1029 (see Section 4.3.3) could not be used here due to the lack of a strong signal.

We trailed, binned, and folded the spectrum in an attempt to confirm the S-wave visually. This, as well as a Doppler tomogram, is also presented in Figure 4.3. Figure 4.4 shows a comparison of the S-wave at the stated orbital period to those generated with two other example periods: 29.99 min and $P_{orb} + 1.94$ min. The former is the next highest peak on the periodogram. The latter is one standard deviation away from the highest peak and would not be expected to show any signal if the periodogram is valid. There is no S-wave present at the alternate periods, despite the relatively high peak at 32.99 min in the periodogram. Similar plots at other possible orbital periods likewise show no signs of an S-wave.

The proposed orbital period is in the same range as that of other known AM CVn systems with similar photometric behaviour. Levitan et al. (2011) and Ramsay et al. (2012) noted that systems with infrequent outbursts are associated with longer orbital periods. The outburst on 2011 Feb 16 was the only observed outburst of PTF1J0435+0029 in PTF and there have been two recorded outbursts in the Catalina Real-Time Transient Survey (Drake et al. 2009) – one roughly coincidental with that observed by the PTF, and one ∼750 d prior. We thus expect the system to have an orbital period between ∼27 min and ∼40 min (the longest observed period for outbursting systems). The faintness of the S-wave is not completely surprising since other systems (e.g., SDSSJ0804+1616; Roelofs et al. 2009) have also been observed to have very weak S-waves at times.

We conclude our discussion of PTF1J0435+0029 with some remarks on the characteristics of its spectrum. The spectrum of PTF1J0435+0029 is particularly notable in this set of AM CVn systems for the absence of N I (see Figure 4.2 and Table 4.4.1). This lack of N I likely points to a different donor composition than the other systems presented here. Specifically, the presence of N I has been linked to a highly enriched CNO cycle in He-WD donors, whereas the abundance decreases in He-star donors because of α-capture on N (Nelemans et al. 2010). Thus this system may have evolved from the He-star donor evolutionary track as opposed to the detached white dwarf binary track.

4.3.2   PTF1 J085724.27+072946.7

PTF1J0857+0729 was discovered in outburst by the transient pipeline on 2011 Jan 27. A classification spectrum taken on 2011 Feb 01 showed distinct helium emission lines, which
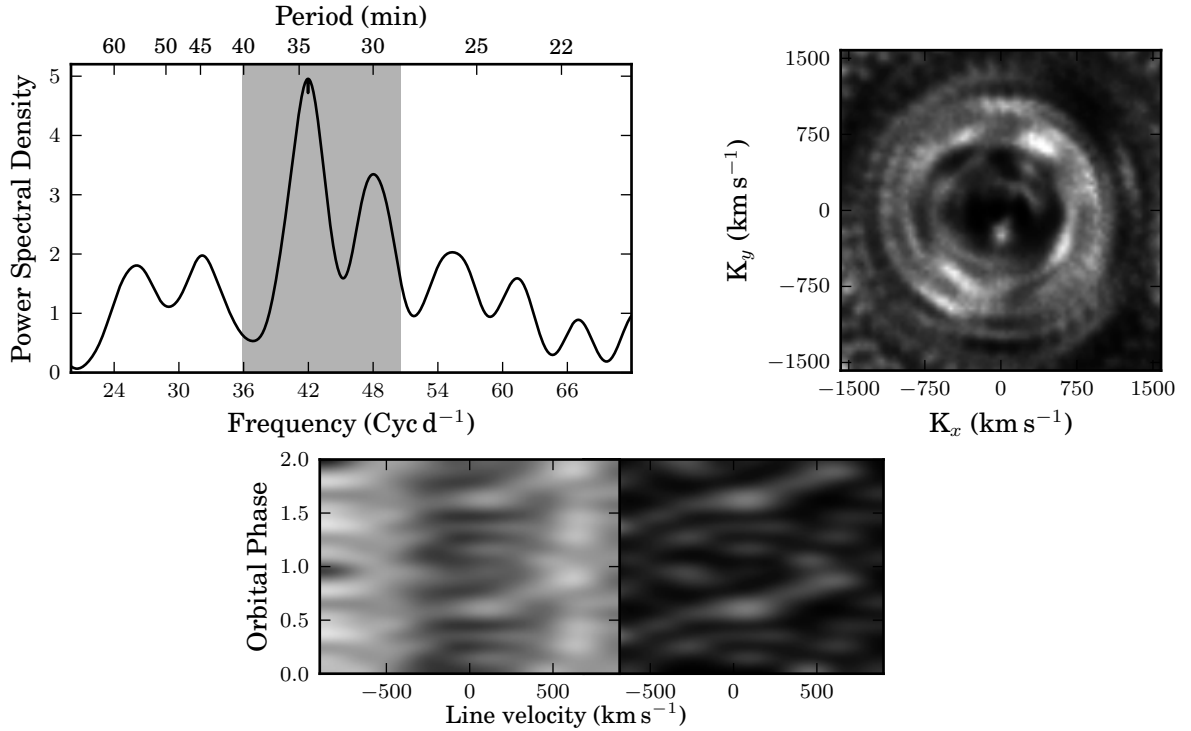
Figure 4.3 **Top Left:** Periodogram of the co-added He I line flux ratios from 5.18 h of PTF1J0435+0029 observations. The calculation of these flux ratios is described in Section 4.2.2. The He I lines at $\lambda\lambda 3888, 4026, 4471,$ and 5015 were used to calculate the flux ratios for this system. The 3σ confidence interval is shaded.
Bottom: The binned, trailed spectra of PTF1J0435+0029 using the co-added He I lines at $\lambda\lambda 4026, 4471, 4713, 4921, 5015, 5875, 6678,$ and 7065 folded at 34.31 min. This corresponds to the peak of the periodogram. An arbitrary zero phase of $HJD = 2455863.91002$ was used, coinciding with the start of the observations. The version on the left retains the disc emission while the version on the right removes the disc emission by subtracting the median of each column.
Top Right: A Doppler tomogram of PTF1J0943+1029 constructed from the same emission lines as the S-wave, plotted to highlight the peak believed to be the hotspot at $(K_x, K_y) \approx (380, 655)\,\mathrm{km\,s^{-1}}$ (the upper right part of the image). An arbitrary zero phase of $HJD = 2455863.91002$ was used, coinciding with the start of the observations.
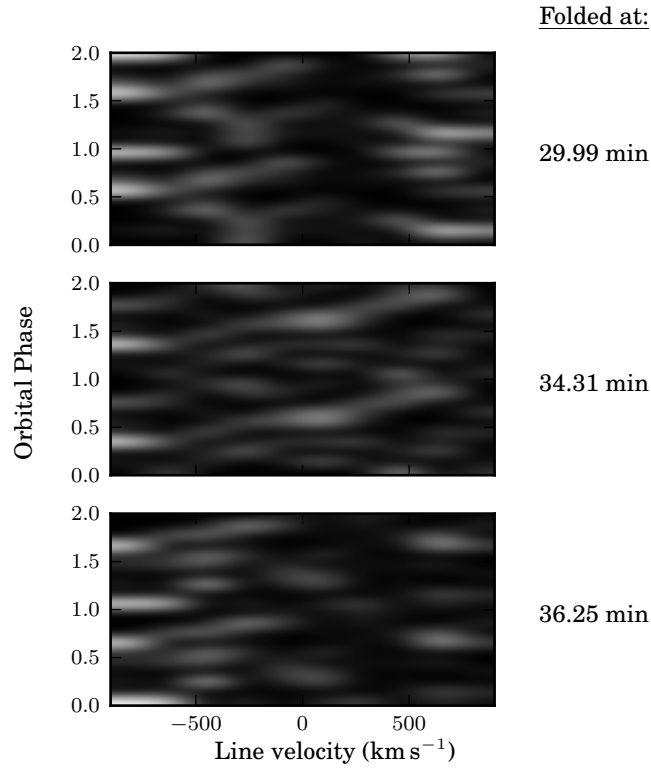
Figure 4.4 A comparison of the binned, trailed spectra of PTF1J0435+0029 using the co-added He I lines at $\lambda\lambda 4026, 4471, 4713, 4921, 5015, 5875, 6678$, and 7065 folded, from top to bottom, at $29.99\,\mathrm{min}$, $34.31\,\mathrm{min}$, and $36.25\,\mathrm{min}$. These correspond to the second most significant peak of the periodogram, the proposed orbital period, and the period at the upper end of the error estimate, respectively. An arbitrary zero phase of $HJD = 2455863.91002$ was used for all three plots, coinciding with the start of the observations. The median of each velocity bin was subtracted to remove the contribution from the accretion disc. Only the plot at $34.31\,\mathrm{min}$, the proposed orbital period, shows a discernible S-wave; plots at other periods show noise and no signal.
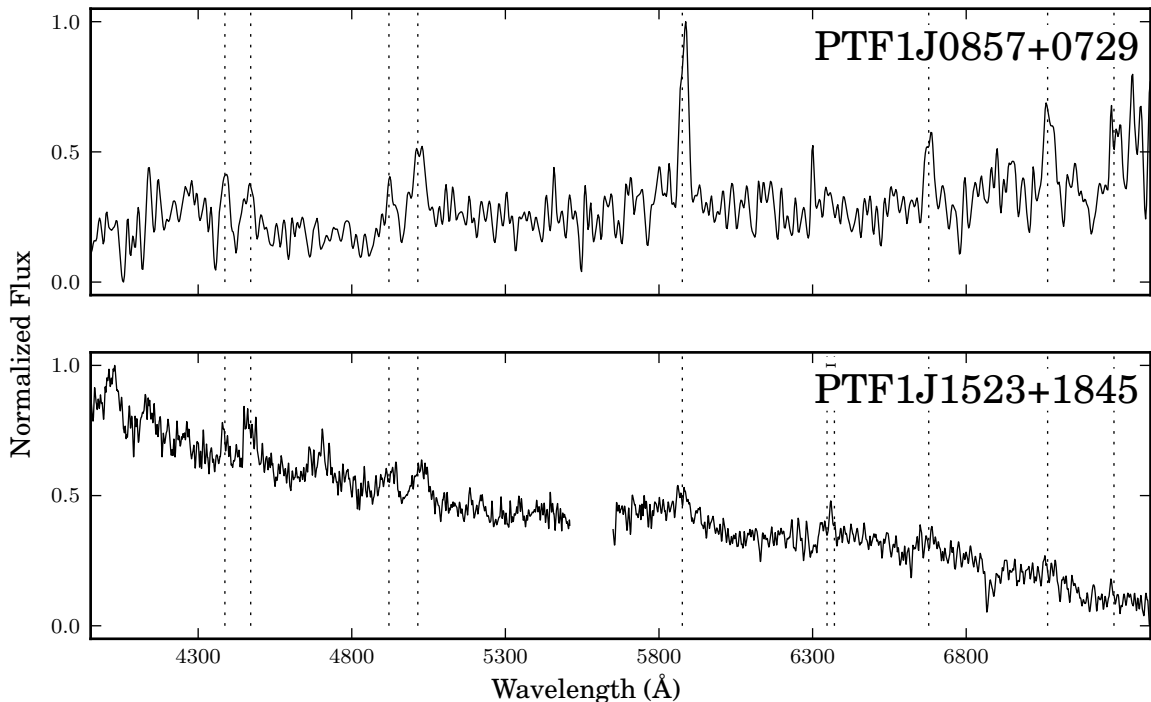
Figure 4.5 Spectra of PTF1J0857+0729 and PTF1J1523+1845 taken in outburst. Prominent He I lines at $\lambda\lambda 4387, 4471, 4921, 5015, 5875, 6678, 7065$, and 7281 are marked with dashed lines, as well as Si II for PTF1J1523+1845. The specific observations used are marked in Table 5.1. Spectra were Gaussian smoothed by 5 pixels. We particularly note the presence of emission lines and no absorption lines in both systems, something that has not been observed previously in AM CVn system outburst spectra.

were confirmed with a second spectrum the following night (see Figure 4.5).

In CVs, the presence of emission lines in outburst is indicative of a high inclination, and thus often eclipsing, system (e.g., Warner 1995). Previously, all AM CVn systems spectroscopically observed in outburst showed absorption lines (e.g., Roelofs et al. 2007b). We obtained a two-hour light curve at the P200 on 2011 Nov 30 (45 s exposure time; 24 s dead time) and another two-hour light curve at the NOT on 2012 Feb 28 (60 s exposure time; 5 s dead time) to search for eclipses. AM CVn systems are expected to have very short eclipses on the order of a minute (e.g., Copperwheat et al. 2011), so short exposures times are necessary.

The individual photometric measurements had errors of $\sim 3\%$ and $\sim 5\%$, respectively. Periodograms constructed from these light curves showed no significant period, although the light curves did show variability with an amplitude of $0.1 - 0.15$ mag. Lack of data precludes a definitive determination, but this is consistent with the amplitude of periodic

variability found in other quiescent AM CVn systems (e.g., Provencal et al. 1997). None of the photometric measurements were fainter than 0.1 mag below the median magnitude and thus we conclude that no eclipses were detected.

We next consider whether eclipses may have been missed due to dead time between exposures. We assume that the eclipse duration is 60 s with steep ingress and egress and a worst case scenario where the dead time is exactly in the middle of the eclipse. Given the possible variability observed and the short observing times, we define an eclipse to be a measurement at least 0.3 mag ($2 - 3\times$ the variability) below the median. We calculate that in this worst case scenario, eclipses of $\gtrsim 1.0$ mag should have been visible in the P200 data and eclipses of $\gtrsim 0.8$ mag should have been visible in the NOT data. Thus, any eclipses missed are relatively shallow.

4.3.3   PTF1 J094329.59+102957.6

PTF1J0943+1029 was discovered as part of the photometric database search (see light curve in Figure 4.1). An initial classification spectrum showed strong helium emission lines. We obtained a total of 5.45 h of phase-resolved spectroscopy of PTF1J0943+1029 on 2011 Dec 25 and 2011 Dec 31 using Keck-I/LRIS. We present the co-added spectrum in Figure 4.6.

This data were analysed for the orbital period. The peak of the periodogram is at 30.35 min (Figure 4.7), and an S-wave and Doppler tomogram generated at this period show a strong signal (Figure 4.8). The number of strong aliases adjacent to the peak frequency make a good error estimate crucial.

To obtain an estimate of the error, we exploited the properties of the Doppler tomograms. As discussed in Section 4.2.2, the hotspot should be concentrated in a single spot on the Doppler tomogram. Hence, the correct orbital period should correspond to the Doppler tomogram with the sharpest hotspot. We define this to be the hotspot with the smallest FWHM, using a two-dimensional Gaussian model. We note that this method could not be used reliably for PTF1J0435+0029 due to the much worse signal-to-noise in that data.

We calculated 1,000 Doppler tomograms for periods between 27.2 min and 33.5 min in ~ 0.1 min steps (43 to 53 cyc/d in 0.1 cyc/d steps) and measured the FWHM of the hotspot in each using a two-dimensional Gaussian fit. To estimate the error, for each of 1,000 iterations, we drew 100 FWHM measurements from the range of 46 to 50 cyc/d and fit
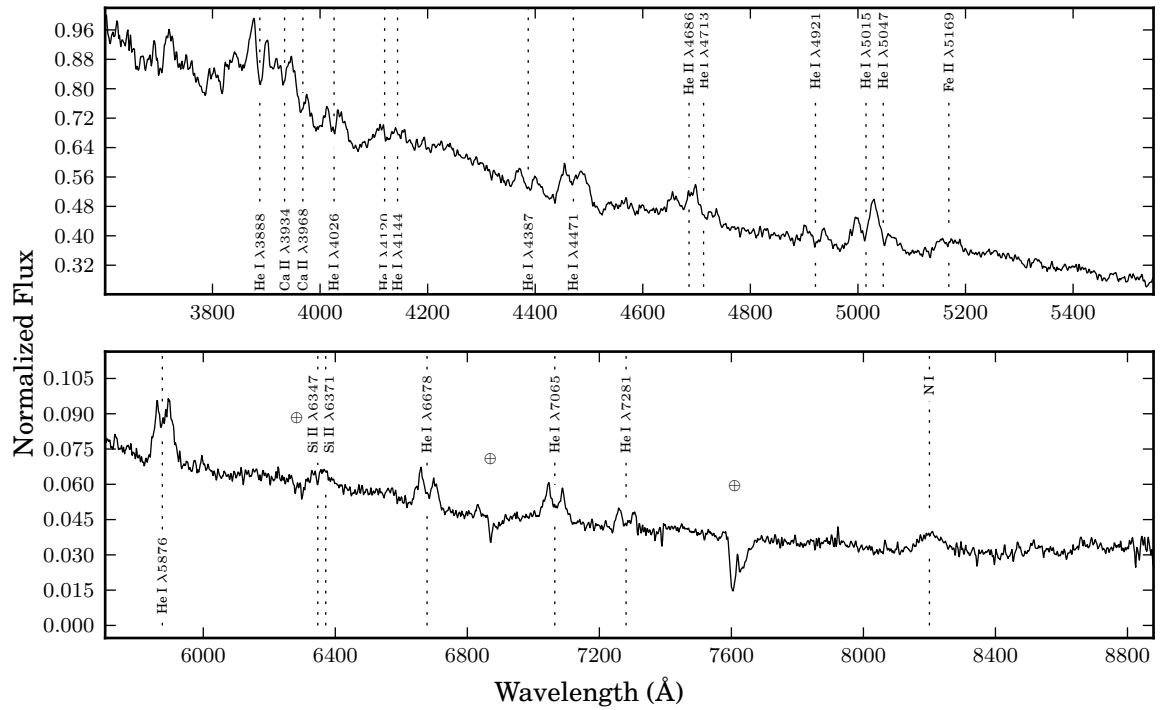
Figure 4.6 A spectrum of PTF1J0943+1029 in quiescence. The blue (top) spectrum is a co-add of the ∼4 h observed on 2011 Dec 25. The red (bottom) spectrum is a co-add of the ∼1.5 h observed on 2011 Dec 31.

a parabola to the measurements. This limited range was required to eliminate inaccurate measurements due to multi-peak "spots" outside of this range that gave inaccurate, small FWHM measurements.

This simulation found a median period of $30.17 \pm 0.65\,\mathrm{min}$, within one sigma of the peak of the periodogram. We plot all FWHM's and the best fit using all points in Figure 4.7. The error estimate of this simulation is consistent with a visual inspection of S-waves and Doppler tomograms around the peak of the periodogram. Given the error and the visual representations of the orbit in Figure 4.8, we conclude that the median period from this simulation is the orbital period of the system.

4.3.4 PTF1 J152310.71+184558.2

PTF1J1523+1845 was discovered in outburst on 2010 Jul 7 as part of the transient search. Spectra taken on 2010 Jul 7 and 2010 Jul 8 showed He I emission lines (see Figure 4.5). This makes it the second known outbursting AM CVn system to exhibit emission lines in outburst. Extensive follow-up on this system was not performed, due to its faint nature $(g' > 23)$.

4.3.5 PTF1 J163239.39+351107.3

PTF1J1632+3511 was discovered in outburst on 2011 May 11 and a spectrum was obtained on 2011 Jul 5. This source is extremely faint $(g' \approx 23)$ and is located adjacent to a significantly brighter galaxy. We present the spectrum in Figure 4.9. The spectrum shows He I $\lambda 5875$ emission, possible He I $\lambda 6678$ and He II $\lambda 4686$ emission, and no trace of H lines. We exclude it as a possible supernova from the He I lines at $z = 0$. Based on the evidence, we conclude that PTF1J1632+3511 is a likely AM CVn system, but a higher signal-to-noise spectrum is required before this can be established with certainty.

4.3.6 PTF1 J221910.09+313523.1

PTF1J2219+3135 was discovered as part of the photometric database search (see Figure 4.1 for the light curve and Figure 4.10 for the identification spectrum). The relatively low-quality identification spectrum has a particularly interesting set of lines. Specifically, several lines redward of Fe II $\lambda 5169$ at $\lambda 5276$ and $\lambda 5317$ have only been observed in V406 Hya (Roelofs et al. 2006a) $(P_{\mathrm{orb}} = 33.8\,\mathrm{min})$ and SDSSJ0804+1616 (Roelofs et al. 2009)
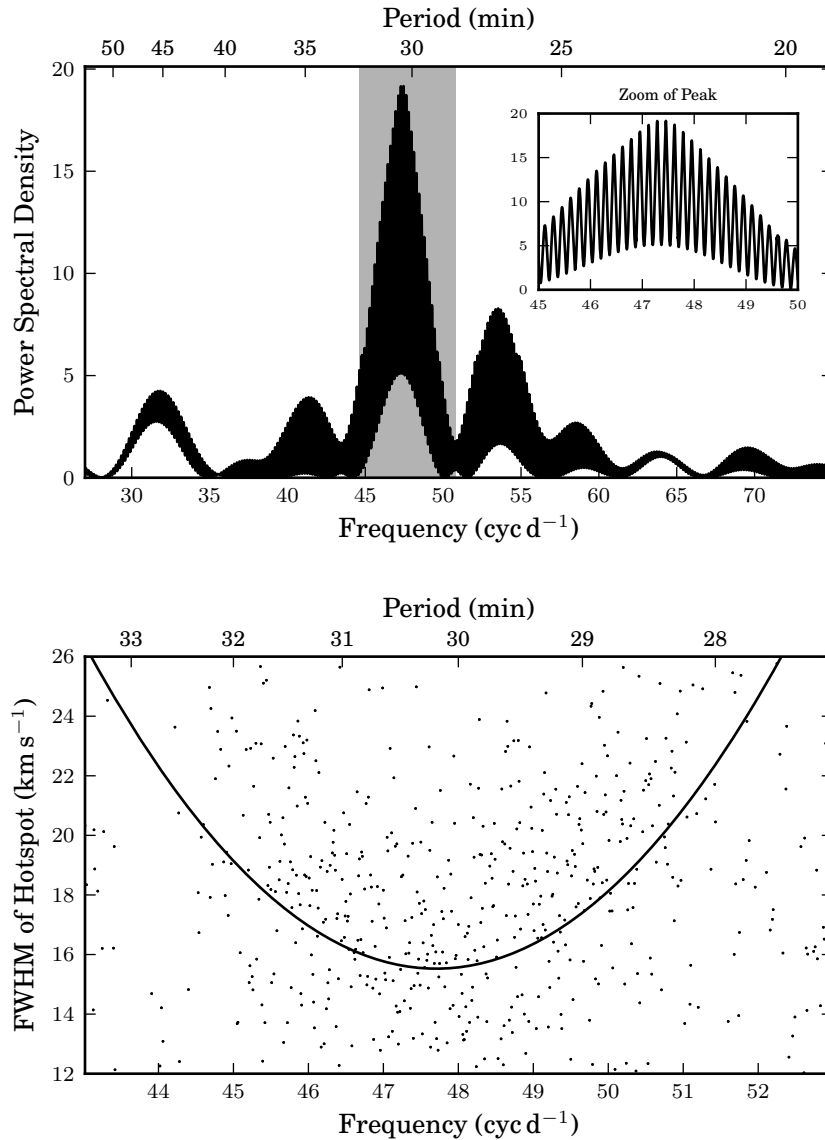
Figure 4.7 **Top:** Periodogram of the flux ratios of PTF1J0943+1029. There are no strong peaks outside of the frequency range shown here. The peak is at 30.35 min. The He I lines at $\lambda\lambda 3888, 4026, 4471,$ and 5015 were used to calculate the flux ratios for this system. The shaded region represents the 3σ confidence interval around the proposed orbital period. **Bottom:** The FWHMs of the hotspots in 1,000 Doppler maps calculated at a range of periods. The solid line is the best fit of a quadratic equation. Its minimum of 30.17 min is within one sigma of the peak of the periodogram.
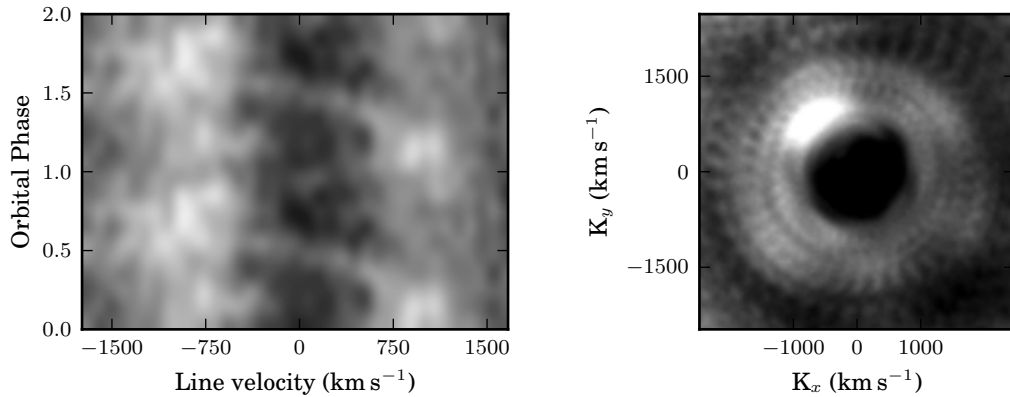
Figure 4.8 **Left:** The S-wave used to visually confirm the period of PTF1J0943+1029. The He I lines at $\lambda\lambda 3888, 4026, 4471, 4713, 4921,$ and 5015 and the He II line at $\lambda 4686$ were folded at a period of 30.35 min to generate the image. The S-wave was phase-binned into 10 bins with a zero phase of HJD = 2455920.962.

Right: Doppler tomogram of PTF1J0943+1029 using the He I $\lambda\lambda 4027, 4471, 4713, 4921,$ and 5015 and He II $\lambda 4685$. The zero phase here is the same as for the S-wave.
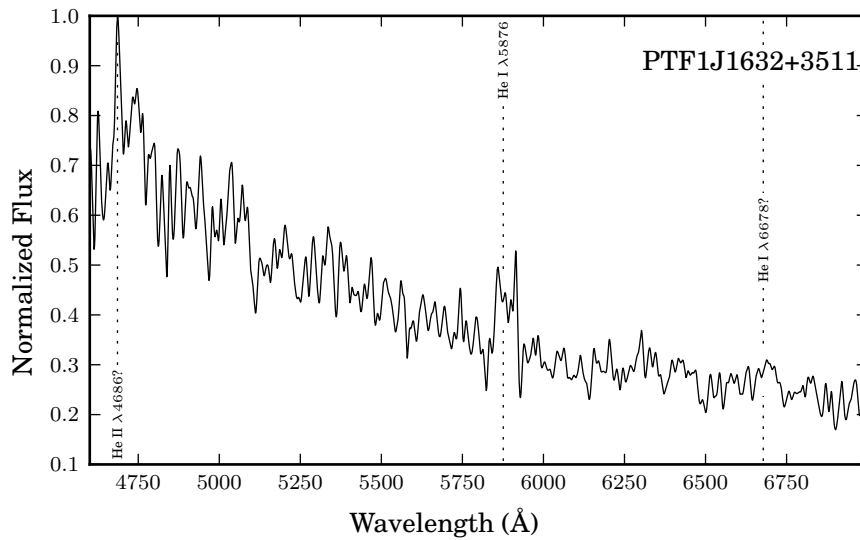
Figure 4.9 Classification spectrum of PTF1J1632+3511 taken on 2011 Jul 5. The system is assumed to be either in or near quiescence. The closest PTF photometric measurement on 2011 Jul 11 has no detection to a limiting magnitude of 20.67. The poor quality of the spectrum precludes us from classifying this as an AM CVn system. However, after Gaussian smoothing by 10 pixels we can identify He I $\lambda 5875$ emission, possible He I $\lambda 6678$ and He II $\lambda 4686$ emission, and no evidence of H.
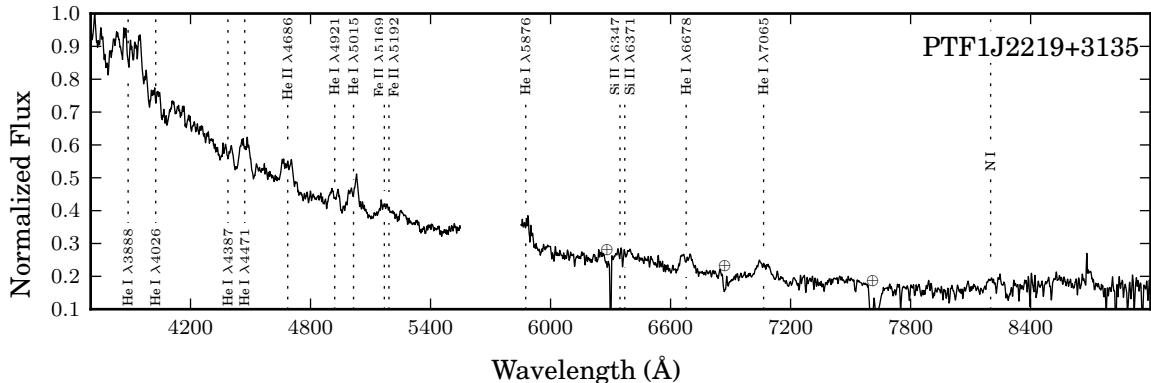
Figure 4.10 Classification spectrum of PTF1J2219+3135 taken in quiescence. The prominent He and metal lines are marked (see Section 4.4.1).

$(P_{\mathrm{orb}} = 44.5\,\mathrm{min})$. These may also be Fe II, but such lines are unusual. Note that unique identification of weak features is made more difficult due to the large width of the lines due to Doppler broadening of the rotating accretion disc.

4.4   Discussion

4.4.1   Spectral Features

We present equivalent widths for lines in each of the five systems presented here in Table 4.4.1. In this section, we compare the features of the systems with relatively high signal-to-noise: PTF1J0435+0029, PTF1J0943+1029, and PTF1J2219+3135. As expected, the spectra of the systems in this sample show signs of having shorter orbital periods than those detected in the SDSS. Particularly, we note the lack or relative weakness of the absorption wings surrounding the He emission lines. These absorption wings are from the WD primary and are expected to be less visible in shorter period systems if the mass transfer rate monotonously decreases with increasing orbital period, since this will create a relatively luminous accretion disc with respect to the luminosity of the accretor. We also see the presence of Ca II H & K in all three systems, which has been seen in shorter period systems such as V406 Hya (Roelofs et al. 2006a), but is less prevalent in longer period systems (those with $P_{orb} > 50\,\mathrm{min}$; Roelofs et al. 2005; Kupfer et al. in prep).

Of particular interest for the general study of AM CVn systems is the identification of the donor and therefore the evolutionary history of these systems. Marsh et al. (1991) predicted the Si II emission at $\lambda 6346$ and $\lambda 6371$ and Fe II emission at $\lambda 5169$ to be the

Table 4.3. Equivalent widths of prominent lines of PTF-discovered systems

Line	PTF1J0435+0029	PTF1J0857+0729	PTF1J0943+1029	PTF1J1523+1845	PTF1J2219+3135
Ca II 3933/3968	blended with He	X	blended with He	X	blended with He
He I 4026	-4.6 ± 0.7	X	X	-3.7 ± 0.9	-5.1 ± 0.8
He I 4388	X	... b	-2.3 ± 0.3	-1.2 ± 0.5	-1.7 ± 0.2
He I 4471	-10.0 ± 0.7	-13 ± 5.1	-10.4 ± 0.3	-5.7 ± 0.7	-6.6 ± 0.2
He II 4685/4713	-6.4 ± 0.8	X	-9.6 ± 0.4	-5.7 ± 0.9	-3.5 ± 0.3
He I 4921	-7.9 ± 0.7	-10.6 ± 5.4	-1.6 ± 0.3	-2.5 ± 0.7	-4.8 ± 0.2
He I 5015/5047	-10.0 ± 0.6	-34.9 ± 5.9	-17.1 ± 0.4	-5.5 ± 0.8	-9.1 ± 0.2
He I 5875	-49.8 ± 2.0	-62.9 ± 5.6	-21.8 ± 0.6	-7.4 ± 0.7	X
He I 6678	-33.1 ± 2.0	-19.6 ± 5.6	-14.1 ± 0.6	-4.2 ± 0.8	-10.7 ± 0.2
He I 7065	-29.8 ± 1.9	-26.6 ± 5.1	-15.0 ± 0.7	... b	-15.1 ± 0.3
He I 7281	-28.4 ± 2.4	X	-9.3 ± 0.6	X	... a
Fe II 5169	-0.8 ± 0.7	X	-4.8 ± 0.3	... b	-9.8 ± 0.2
Si II 6347/6371	... b	X	-6.5 ± 0.7	-3.8 ± 0.6	-9.5 ± 0.3
N I 8184/8188/8200	X	... c	-7.8 ± 0.7	... a	-3.6 ± 0.9

Note. — Lines marked with X indicates that this line is not detectable above the noise level of the spectrum obtained.

[a]Line present but contaminated with atmosphere.

[b]Line present but insufficient SNR to measure.

[c]Spectrum does not extend to this wavelength.

strongest lines in helium dominated optically thin accretion discs. They will be important to determine the initial metallicity in follow-up work as iron and silicon are not supposed to be affected by nuclear synthesis processes in AM CVn systems. Those features are well observed in other outbursting AM CVn systems, including V406 Hya (Roelofs et al. 2006a) and CP Eri (Groot et al. 2001). Here, we find the presence of Si II and Fe II in all three systems. However, as noted earlier, N I is uniquely missing in PTF1J0435+0029, indicating the donor is more likely to have evolved from a He-star. PTF1J0943+1029 and PTF1J2219+3135, on the other hand, are more likely to have a He WD as the donor star.

4.4.2   Comparison of System Colors

The release of the SDSS data revolutionized the study of AM CVn systems. Initially, seven systems were discovered via a search for He emission lines in the SDSS database (Roelofs et al. 2005; Anderson et al. 2005, 2008). Subsequently, a spectroscopic survey of a color-selected sample from SDSS has been carried out and six more systems were found (Roelofs et al. 2009; Rau et al. 2010; Carter et al. 2013a). However, both of these studies have used colors to select systems for spectroscopic observation. In the case of the general SDSS survey, various criteria are used to select follow-up targets while the dedicated AM CVn search used a color cut based on the colors of known AM CVn systems.

The sample here, together with PTFJ0719+4858 presented by Levitan et al. (2011), is unique as the first sample of AM CVn systems discovered systematically by their large-amplitude photometric variability as opposed to their spectral characteristics (and equivalently colors). It thus allows us to consider the completeness of the color-selection criteria developed in Roelofs et al. (2009).

We note that these criteria target only quiescent systems since the spectra and colors of AM CVn systems do change during outburst. Given that the SDSS survey is expected to be most sensitive to longer-period systems and that these are believed to make up the vast majority of the population, this is a valid assumption. However, although our colors of PTF-discovered systems are from the quiescent states, our better sensitivity to shorter-period systems may result in slightly different colors.

The quiescent magnitudes in each filter were presented in Table 4.1 and we plot the colors of our sources, together with known AM CVn systems and background sources in Figure 4.11. The colors of the PTF-discovered systems are from the quiescent state; those

of previously known systems are determined from the SDSS photometry and may or may not be in quiescence. However, given that these are all longer-period systems, it is highly likely that almost all are in quiescence. We do not include PTF1J1635+3511 in this plot since it is only a candidate. Additionally, it is likely contaminated with the nearby galaxy, especially at the redder wavelengths.

We find that the PTF-discovered systems generally fall within the color cut. One system, PTF1J1523+1845, does show colors outside of the color cut, but, given its faintness, additional measurements should be made to verify this. Given these results, we urge caution in narrowing the color cut, as suggested by Carter et al. (2013a), to avoid missing redder AM CVn systems. However, both additional systems and further measurements are necessary before concluding whether outburst-identification is sensitive to a population substantially different than the SDSS color-selected sample.

4.5 Conclusions

We present five new AM CVn systems and one new AM CVn candidate, which were identified by their characteristic He I and He II emission lines and lack of H. We further present spectroscopic measurements of three of these systems, finding their orbital periods to be consistent with other AM CVn systems. Two of the systems presented here have the unique characteristic of strong emission lines while in outburst, often seen in eclipsing cataclysmic variable systems. We tested whether one of these systems is eclipsing but did not find evidence to support this hypothesis. Finally, we compared the spectroscopic and photometric features of these systems to other known AM CVn systems.

Figure 4.11 The color-color diagrams for AM CVn systems, including background SDSS-detected systems. AM CVn system are marked as black squares. Those labelled with a letter and with error bars are from this paper; those without are previously known systems with SDSS colors. Shaded areas indicate the density of the background systems – darker areas indicate a denser area in color-color space. The lines delineate the color cut from Roelofs et al. (2009). We have corrected for extinction in the same way as Roelofs et al. (2009), but note that the distances to AM CVn systems are relatively small (Roelofs et al. 2007a) and thus the reddening is likely overestimated (Schlegel et al. 1998; Roelofs et al. 2009). The PTF-discovered systems tend to lie close to the color cut, but their exact position is uncertain due to large error bars.

Chapter 5

PTF1 J191905.19+481506.2 — A Partially Eclipsing AM CVn System Discovered by the Palomar Transient Factory[⋆]

David Levitan[1], Paul J. Groot[1,2], Thomas Kupfer[2], Bruce Margon[3], Thomas A. Prince[1], Shrinivas R. Kulkarni[1], Gregg Hallinan[1], Leon K. Harding[1], Gillian Kyne[4], Russ Laher[5], Eran O. Ofek[6], René G. M. Rutten[7], Branimir Sesar[1], and Jason Surace[5]

[1] Division of Physics, Mathematics, and Astronomy, California Institute of Technology, Pasadena, CA 91125, USA.

[2] Department of Astrophysics/IMAPP, Radboud University Nijmegen, PO Box 9010, NL-6500 GL Nijmegen, the Netherlands.

[3] Department of Astronomy and Astrophysics, University of California, 1156 High Street, Santa Cruz, CA 95064, USA.

[4] Centre for Astronomy, School of Physics, National University of Ireland, Galway, Ireland.

[5] Spitzer Science Center, MS 314-6, California Institute of Technology, Pasadena, CA 91125, USA.

[6] Department of Particle Physics and Astrophysics, Weizmann Institute of Science, Rehovot, 76100, Israel.

[7] GRANTECAN S.A. Cuesta de San José, s/n - 38712 - Breña Baja - La Palma, España.

[⋆]A version of this chapter is in preparation for submission to the *The Astrophysical Journal*.

Abstract

We report on PTF1 J191905.19+481506.2, a newly discovered, partially eclipsing, outbursting AM CVn system found in the Palomar Transient Factory synoptic survey. This is only the second known eclipsing AM CVn system. We use high-speed photometric observations and phase-resolved spectroscopy to establish an orbital period of $22.4559(3)$ min. We also present a long-term light curve and report on the normal and super-outbursts regularly seen in this system, including a super-outburst recurrence time of $36.8(4)$ d. We use the presence of the hot spot eclipse to place upper and lower limits on the inclination of the system, discuss the number of known eclipsing AM CVn systems versus what would be expected, and consider the implications of the weak hot spot identified in phase-resolved spectroscopy.

5.1 Introduction

AM CVn systems are rare, ultra-compact, semi-detached, white dwarf binaries with periods ranging from 5 to 65 minutes. While they were first identified over 40 years ago by Smak (1967), it has only been in the last decade that the number of known systems has risen above ten. Yet despite the recent discovery of almost 25 additional systems, their rich and complex phenomenological behavior has limited our understanding of this class of post-period minimum binaries. They are considered to be the helium analog of cataclysmic variables (CVs) and are important as strong, low-frequency Galactic gravitational wave sources (Nelemans et al. 2004; Roelofs et al. 2007d; Nissanke et al. 2012), the source of the proposed ".Ia" supernovae (Bildsten et al. 2007), and one of the believed end-points of binary white dwarf evolution (Nelemans et al. 2001). However, many questions about these unique systems remain, including their population density, their evolutionary pathways, and the interactions between the two components, including the He-rich accretion disk. We refer the reader to Nelemans (2005) and Solheim (2010) for general reviews.

As semi-detached binaries, AM CVn systems are believed to have a relatively massive, degenerate accretor and a much less massive (semi-)degenerate donor. The most important first measurement of AM CVn system structure is an orbital period measurement, which is typically accomplished by obtaining a series of short exposure spectra, known as phase-

resolved spectroscopy, and identifying the change in flux caused by the movement of the "hot spot" (Nather et al. 1981). This hot spot is the result of the matter transferred from the donor hitting the accretion disk. Since the hot spot is on the outside of the accretion disk and is stationary in the binary frame, its movement reveals the orbital period.

However, to use the velocity information contained in phase-resolved spectroscopy to its fullest one needs to know the system's inclination with respect to our line of sight. It is only for those systems showing eclipses that a full determination of the system's parameters (e.g., component masses, inclination, period, etc...) can be obtained. Eclipses also allow for the extremely precise measurement of the orbital period change. For example, the orbital period of the double-detached, white-dwarf binary SDSSJ0651+2844 was measured to be decreasing by Hermes et al. (2012). To date, only one known AM CVn system has been observed to have an eclipse, SDSSJ0926+3624 (Anderson et al. 2005; Copperwheat et al. 2011), but no period derivative has yet been determined.

AM CVn systems have been observed to have three relatively distinct phenomenological states. Systems with $P_{orb} < 20\,\mathrm{min}$ have been observed in a "high" state, characterized by optically thick accretion disks and absorption-line spectra. In contrast, systems with $P_{orb} > 40\,\mathrm{min}$, are observed to have emission-line spectra from what are believed to be optically thin accretion disks and are said to be in quiescence (though see Woudt et al. 2013 and Chapter 6 for an example of a longer period system that has been observed to outburst). Neither shows photometric variability over $0.5\,\mathrm{mag}$.

Between these orbital period limits are outbursting systems, which are observed to have dwarf nova-type outbursts of 3–6 mag as well as variability at the 10% level in both quiescence and outburst (e.g., Patterson et al. 1997). Recent studies have shown that the frequency of these outbursts decreases as the orbital period increases (Levitan et al. 2011; Ramsay et al. 2012, Chapter 6).

The population density of AM CVn systems has not been conclusively determined: population synthesis estimates of the space density (Nelemans et al. 2001) have not been observationally confirmed by color-selected samples (Roelofs et al. 2007d; Carter et al. 2013a). The latest results of Carter et al. (2013a) suggest a space density of $(5 \pm 3) \times 10^{-7}\,\mathrm{pc}^{-3}$, a factor of 50 lower than the population synthesis estimates by Nelemans et al. (2001). The reason for this discrepancy is currently unknown. We note that these color-selected samples are mostly sensitive to longer period systems.

Over the last two years, we have conducted a search for outbursting AM CVn systems using the Palomar Transient Factory[1] (PTF; Law et al. 2009; Rau et al. 2009) large-area synoptic survey, in part, to use a different approach to the discovery of AM CVn systems that does not rely on their colors. The PTF uses the Palomar 48″ Samuel Oschin Schmidt telescope to image up to $\sim 2,000 \, \mathrm{deg}^2$ of the sky per night to a depth of $R \sim 20.6$ or $g' \sim 21.3$. After identifying outbursting systems, we obtain classification spectra. To date, this survey has identified >200 cataclysmic variables (CVs; Groot et al. in prep),six new AM CVn systems, and one extremely faint AM CVn candidate (Levitan et al. 2011, 2013).

In this paper, we present PTF1 J191905.19+481506.2 — a new AM CVn system discovered by the Palomar Transient Factory. This system is particularly interesting because:

- of the presence of shallow eclipses, making it only the second known eclipsing AM CVn system.

- its orbital period is the shortest known of outbursting AM CVn systems.

We note that while this system is in the Kepler field, it, unfortunately, falls into a gap between the detectors of the *Kepler* satellite. Thus, high-cadence observations are only possible from the ground at this time.

This paper is organized as follows. In Section 5.2 we discuss our data reduction and analysis methods. In Section 5.3 we present both short-term and long-term photometric and spectroscopic data and perform a period analysis. We consider the super-outburst recurrence time of the system, its geometric structure, and the rate of eclipsing AM CVn systems in Section 7.5. We summarize in Section 5.5.

5.2 Data Acquisition, Reduction, and Analysis

5.2.1 Photometric Data

The initial discovery of PTF1 J191905.19+481506.2, hereafter PTF1J1919+4815, as an outbursting compact binary candidate was made using the PTF. Two pipelines process PTF data. The "transient" pipeline uses difference imaging to identify possible transients in real-time (Gal-Yam et al. 2011). In contrast, the "photometric" pipeline prioritizes photometric

---

[1]http://ptf.caltech.edu/

accuracy at the cost of processing time and uses aperture photometry to measure fluxes. This paper uses data from the latter.

The photometric pipeline applies standard de-biasing, flat-fielding, and astrometric calibration to raw images Laher et al. (in prep). Absolute photometric calibration to the few percent level is performed using a fit to SDSS fields observed in the same night (Ofek et al. 2012). Additional relative photometric calibration is applied to improve precision to 6–8 mmag at the bright end of $R \sim 14$ and 0.2 mag at the faint end of $R \sim 20.6$. This algorithm is described, in part, in Section 5.2.1.1 and in Chapter 7.

While the initial identification of the system as an outbursting, compact binary candidate was done using data from the aforementioned pipeline, the crowded nature of the field requires PSF photometry for optimal results. We therefore re-processed the PTF images using the same pipeline as described in Section 5.2.1.1.

Dedicated long-term monitoring was obtained using the Palomar 60″ (P60) telescope. The P60 automated pipeline, which includes automated de-biasing, flat-fielding, and astrometric calibration, is described in Cenko et al. (2006).

High-cadence observations were obtained from two sources. The first observations were made using the Lick 3-m Shane telescope with the Kast imaging spectrograph in imaging mode. We inserted a g' filter into the user filter wheel, replaced the dichroic with a mirror, and used a clear window instead of a grism. This provided an approximately $2' \times 2'$ field of view in a single filter with a dead time of 3.0 s between exposures utilizing the fast CCD read-out mode and disabling auto-erase of the CCD. Data were de-biased and flat-fielded using standard routines and astrometrically calibrated using the STARLINK package AUTOASTROM.

More recent high-cadence observations were obtained with the Caltech High speed Multicolor camERA (CHIMERA), recently developed for the Palomar 200″ (5.1 m) telescope's (P200) prime focus. Incoming light is split using a dichroic element onto two cameras, first passing through a g' filter on one side and an r' or i' filter on the other. The instrument can interchangeably make use of either Andor NEO sCMOS cameras or Andor iXon 897 Ultra EM-CCD cameras, depending on the requirements (field of view, cadence, red versus blue response) for each program.

For this paper, we use only g' data captured by an Andor EM-CCD. This camera, when installed in CHIMERA, provides a $2' \times 2'$ field of view with $0.35''$ pixel^{-1} plate scale.

Exposures were de-biased and flat-fielded using standard routines. Photometric calibration was performed as described in Section 5.2.1.1, with the exception that the photometric measurements were made using the APPHOT package in IRAF.

5.2.1.1 Photometric Calibration

Photometric measurements for the PTF, P60, and Lick data presented here were made using PSF photometry using the AUTOPHOTOM package. Photometric calibration was performed for all photometric data using a least-squares matrix algorithm described in Ofek et al. (2011) and Levitan et al. (2011). The algorithm is similar to that in Honeycutt (1992), but allows for a simultaneous fit to reference magnitudes, providing both absolute and relative calibration in one step. The absolute calibration for this data was performed relative to USNO B-1.0 and is accurate to 0.3 mag (Monet et al. 2003). We note that the same algorithm is used for the photometric PTF pipeline, except that the photometric PTF pipeline is based on photometric measurements from Sextractor (Bertin & Arnouts 1996).

5.2.2 Spectroscopic Data

Spectroscopic data were acquired from a number of telescopes and instruments; all were long-slit spectrographs. The observations are detailed in Section 5.3. The initial identification spectra obtained using the P200 were reduced using standard IRAF routines. All follow-up phase-resolved spectroscopic data were reduced using optimal extraction (Horne 1986) as implemented in the PAMELA code (Marsh 1989) as well as the STARLINK packages KAPPA, FIGARO, and CONVERT. Spectra obtained from the red side of Keck-I/LRIS were processed with L.A. COSMIC (van Dokkum 2001) due to the large number of cosmic rays.

5.2.3 Period Estimation

We use Lomb-Scargle periodograms (Scargle 1982; we use an implementation by Richards et al. 2011) to identify periods in the data. Error estimation is performed using a Monte Carlo approach. For each data set of length N points, we draw N points at random, allowing for repetition. We then generate a Lomb-Scargle periodogram for the selected points and find the peak. This method allows us to randomly vary both the length of the data set and the points from which a period is calculated. We repeat this process 500 times, and take
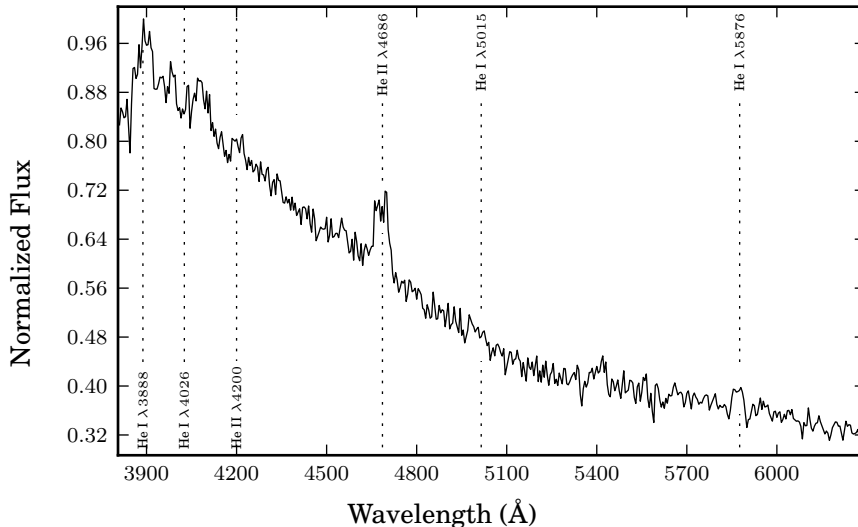
Figure 5.1 The classification spectrum of PTF1J1919+4815 obtained using the DBSP instrument on the Palomar 200″. Significant lines are identified. The absence of Balmer-series lines and the presence of He lines indicated that this was a likely AM CVn system. In contrast with the quiescent spectra of AM CVn systems, very few He I lines show significant emission, most notably He I λ5875, while He II λ4686 is very strong.

their robust standard deviation, defined as $\sigma_{\rm rob} = 0.741(75^{\rm th} \text{ percentile} - 25^{\rm th} \text{ percentile})$, as an estimate of the error.

5.3   Observations and Period Analysis

PTF1J1919+4815 was detected as a possible transient on 2011 July 11. A spectrum obtained at the Palomar 200″ (P200) on 2011 July 23, likely while the system was still in outburst, showed a strong He II 4686 emission line, but no other significant spectral lines (Figure 5.1). A second spectrum taken on 2011 August 03 detected the system while it was in a much fainter state, resulting in much lower signal-to-noise with few discernible lines. The combination of the crowded field (relative to the PTF's pixel scale of $1.01'' \, \text{pix}^{-1}$) and lack of a clear spectral signature led to the object being left for future study.

In 2011 December, PTF1J1919+4815 was identified as a candidate outbursting source as part of the PTF search for outbursting sources (Levitan et al. 2013, Groot et al. in prep). The combination of no Balmer lines and the presence of He II in the initial spectrum, as well as the outbursting behavior, led to its initial classification as an AM CVn system candidate. The likelihood that PTF1J1919+4815 was a short-period system made phase-
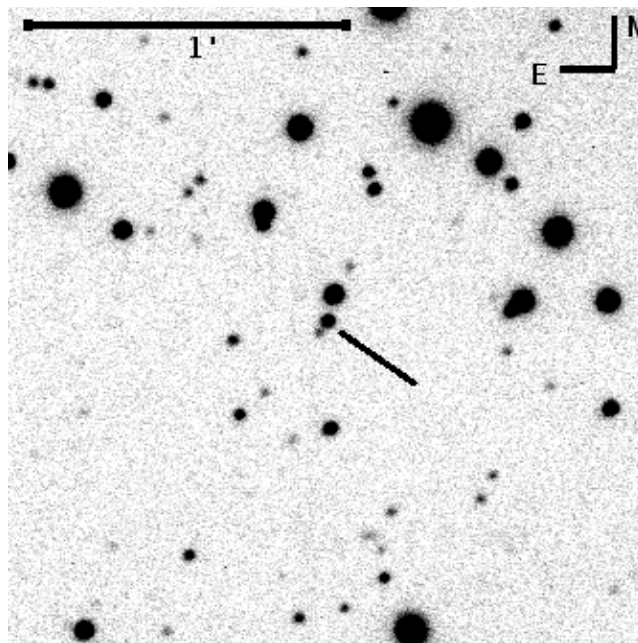
Figure 5.2 A $2' \times 2'$ finding chart of PTF1J1919+4815 based on a 5 min exposure with a g' filter obtained using the P200 while the system was in quiescence. The target is very close to two unrelated stars: a relatively bright star to the northwest and a very faint star to the southeast. The brighter neighbor is too far away to have a significant impact on our data, while careful photometry and the faint nature of the second neighbor should avoid any contamination.

resolved observations necessary to understand its nature.

Between 2012 May and 2013 April, we obtained both high speed photometry (Section 5.3.1) and phase-resolved spectroscopy (Section 5.3.2). Simultaneously, we began long-term photometric monitoring of PTF1J1919+4815 (Section 5.3.3). A summary of all non-PTF observations is presented in Table 5.1. A finding chart, useful given the crowded nature of the field, is in Figure 5.2. A long-term light curve of PTF1J1919+4815, indicating the times of the higher-cadence observations described below, is presented in Figure 5.3. Most data presented here is publicly available on the PTF website.

5.3.1 High-cadence Photometric Observations

We begin by presenting the high-cadence photometric observations, as these provide the most unambiguous measurements of PTF1J1919+4815's geometric configuration. In 2012 May, June, and July we obtained several series of exposures with the Lick 3-m Shane telescope using a g' filter with 15–30 s
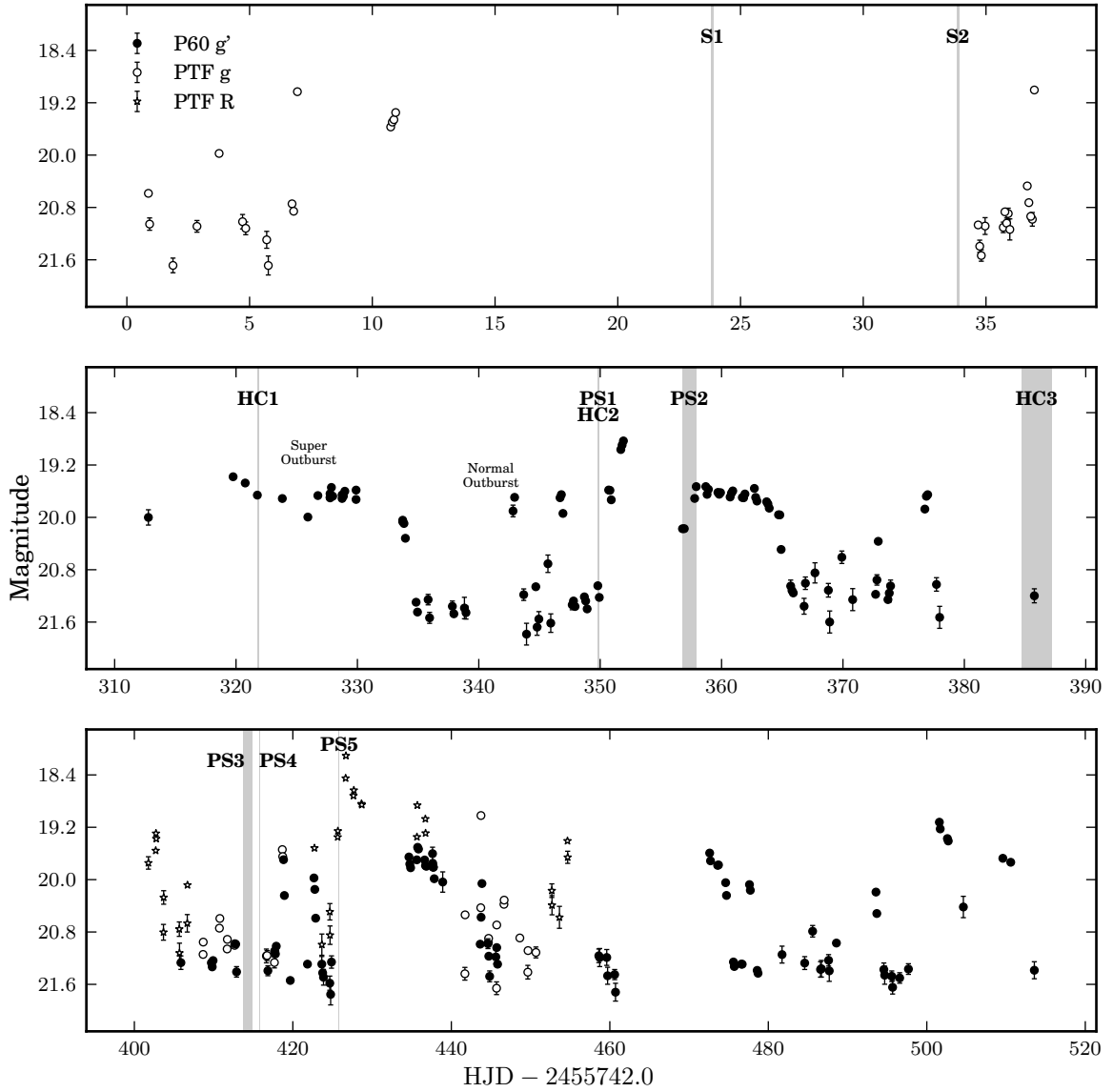
Figure 5.3 A long-term light curve of PTF1J1919+4815, with data from P60 g', PTF R-band, and PTF g'-band. Error bars are only shown for those detections with $\sigma > 0.075$ mag. We label examples of a super outburst and a normal outburst. We also indicate the times of follow-up observations using highlighted areas and labels — HC indicates high-cadence photometry, S indicates a single spectrum, and PS indicates phase-resolved spectroscopy. More information on the follow-up observations is in Table 5.1.

The data from the three telescope and filter combinations were not jointly calibrated. This decision was made since all data were calibrated against an external source (USNO-B 1.0 B-band for g' observations and R-band for R observations) and for the g' data sets are very similar (within 10%). For the large variability highlighted here, additional calibration is not necessary.

Table 5.1. Details of observations of PTF1J1919+4815

Designation	UT Date	State	Telescope	Setup	# of Exp.	Exp. Time (s)
S1	2011 Jul 22	Outburst	P200/DBSP	B: 600/4000, R: 158/7500	1	1200
S2	2011 Aug 02	Quiescence	P200/DBSP	B: 600/4000, R: 158/7500	1	900
S3	2012 Feb 01	Quiescence	P200/DBSP	B: 600/4000, R: 316/7500	1	1480
HC1	2012 May 16	Outburst	Lick/Kast	Imaging (g')	201	30
PS1	2012 Jun 13	Quiescence	Keck/LRIS	B: 600/4000, R: 600/7500	B: 81, R: 76	120
HC2	2012 Jun 13	Quiescence	Lick/Kast	Imaging (g')	203	30
PS2	2012 Jun 20	Outburst	GTC/Osiris	R1000B	40	120
...	2012 Jun 21	Outburst	GTC/Osiris	R1000B	21	120
HC3	2012 Jul 18	Quiescence	Lick/Kast	Imaging (g')	575	15
...	...	...	...	...	100	30
...	2012 Jul 19	Quiescence	Lick/Kast	Imaging (g')	55	30
...	2012 Jul 20	Quiescence	Lick/Kast	Imaging (g')	257	30
PS3	2012 Aug 16	Quiescence	Keck/LRIS	B: 600/4000, R: 600/7500	B: 75, R: 69	120
...	2012 Aug 17	Normal Outburst	Keck/LRIS	B: 600/4000, R: 600/7500	B: 84, R: 78	120
PS4	2012 Aug 18	Quiescence	Gemini/GMOS-N	B600	103	125
PS5	2012 Aug 28	Outburst	Gemini/GMOS-N	B600	110	125
...	2013 Apr 04	Outburst	P200/CHIMERA	Imaging (g')	954	5

Note. — The telescopes/instruments referenced above are as follows:
Gemini/GMOS-N: Gemini North 8-m telescope with the GMOS-N imaging spectrograph (Hook et al. 2004)
GTC/OSIRIS: GranTeCan 10.4-m telescope with the OSIRIS imaging spectrograph (Cepa 1998)
Keck-I/LRIS: Keck-I 10-m telescope with the Low Resolution Imaging Spectrometer (Oke et al. 1995; McCarthy et al. 1998)
Lick/Kast: Shane telescope at the Lick Observatory with the Kast imaging spectrograph (Miller et al. 1988; Miller & Stone 1992)
P200/DBSP: Palomar 200″ telescope with the Double Spectrograph (Oke & Gunn 1982)
P200/CHIMERA: Palomar 200″ with the Caltech High-speed Multi-color CamERA (Section 5.2.1).

exposures. The 3-month baseline of these observations provides the best estimate for a period. However, the relatively long exposure times result in a poor time resolution relative to the short orbital period of AM CVn systems. Our more recent data set, from the P200 telescope with the CHIMERA instrument, has similar signal-to-noise per exposure but with only 5 s integrations and effectively no dead time between exposures. This light curve is ideal for studying the intra-orbital photometric variability of PTF1J1919+4815, but its short length of only ∼1 hr precludes its use for a period determination. We use the latter data set to show the presence of an eclipse (Section 5.3.1.1) and the former data set to identify the precise orbital period (Section 5.3.1.2).

5.3.1.1 CHIMERA Light Curve

We present the CHIMERA light curve in Figure 5.4. At the time of observation, PTF1J1919+4815 was in outburst, and shows the characteristic superhumps seen in other outbursting AM CVn systems (see, e.g., Figure 4 of Wood et al. 2002). Superhumps are believed to be caused by deformation of the disk while the system is in outburst, and typically have periods a few percent longer than the orbital period (Warner 1995). The most prominent features noticeable besides the superhump sawtooth shape are the three "dips" in luminosity for each orbit of PTF1J1919+4815. We now consider the nature of these dips.

We begin by considering the dip which occurs shortly before peak luminosity for each superhump cycle. If one were to remove the other two dips and draw a straight line from peak luminosity to minimum luminosity, then this last dip constitutes the last portion of the sawtooth shape. Hence, we do not believe it to have a geometrical cause beyond the superhump phenomenon itself.

We now turn our attention to the remaining two dips. The presence of one dip with a ≤5% decrease (labeled as "superhump dip" in Figure 5.4) has been observed in other AM CVn systems (e.g., CR Boo and V803 Cen both show such features; Patterson et al. 1997, 2000), but its cause is unknown. However, a second decrease of any kind has not been observed in other systems except SDSSJ0926+3624 (Copperwheat et al. 2011, hereafter C11), the first-discovered eclipsing AM CVn system. Hence, we conclude that the dip near the peak of the superhump is a feature intrinsic to the superhump itself, while the second dip is an eclipse, likely of the hot spot. This conclusion is supported by additional data we
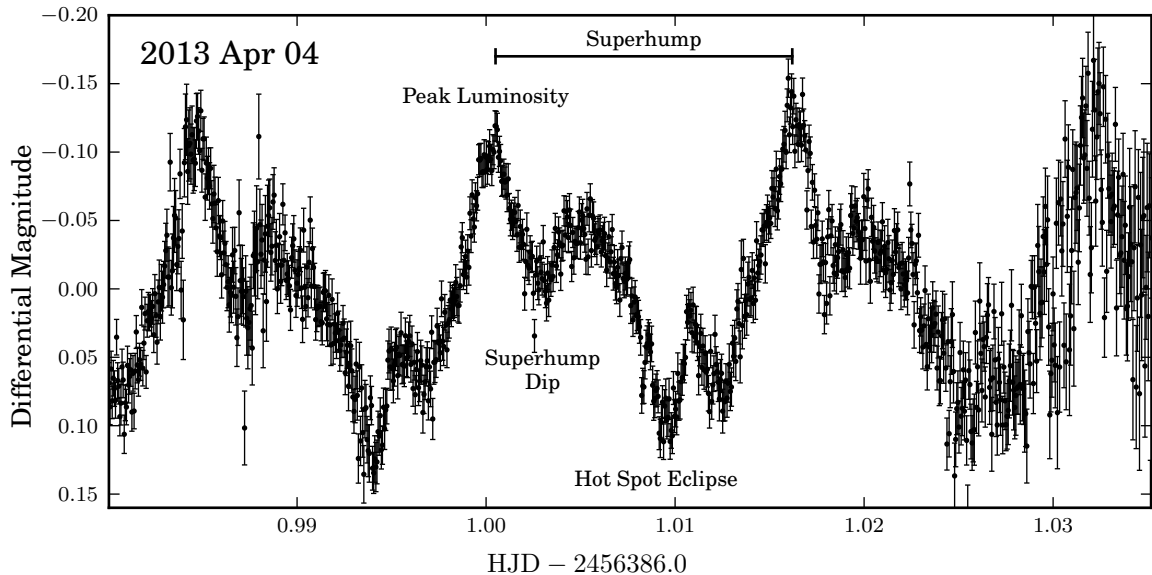
Figure 5.4 The light curve of PTF1J1919+4815 taken using the CHIMERA instrument on 2013 Apr 4. The high time resolution (5 s exposures and effectively no dead time between exposures) resolves many features of the photometric variability; prominent features are labeled. PTF1J1919+4815 was in outburst at the time of observation, and thus shows a superhump structure as well as the eclipse of the hot spot. The increased scatter towards the end of the observations is due to the brightening sky.

acquired from the Shane telescope, which we discuss in Section 5.3.1.2.

The CHIMERA light curve indicates only a single eclipse, with a relatively symmetric ingress and egress. We did consider the possibility that the third dip, which we earlier identified as part of the sawtooth pattern, is an eclipse of the hot spot, making the earlier dip an eclipse of the white dwarf. However, the separation of $\sim$4 min between these two dips means that the donor would have to eclipse the hot spot at an orbital phase of $\sim$0.2, something that is highly unlikely.

In addition to the prominent dips, we also highlight the presence of significant variability on the 1–2 min timescale, particularly immediately after the superhump dip. The source of this variability is unknown and further observations are necessary to ensure that it is, in fact, real. Such variability has also been observed in CVs and is referred to as "flickering" (Warner 1995).

5.3.1.2 Lick Light Curves

The data we obtained from the Lick Shane telescope, while of coarser time resolution, is particularly useful for period analysis due to its long baseline. We present light curves,

Lomb-Scargle periodograms, and folded light curves in Figures 5.5 and 5.6 for the nights of 2012 May 16 and 2012 July 20, respectively. For the data from each night, we subtracted a first order linear fit to remove any roughly linear effects. The remaining nights show similar characteristics to these, and are both included in the overall period analysis in Section 5.3.1.3. All light curves are available on the PTF website.

Both the 2012 May and 2012 July data show variability with an amplitude of $\sim$0.15 mag, including both a small increase in luminosity as well as the eclipse feature. The eclipse is of similar depth to that seen in the CHIMERA data. We believe that the luminosity increase in the 2012 July data is a result of the hotspot rotating into view, as has been shown for CVs (e.g., OY Car; Schoembs & Hartmann 1983) and AM CVn systems. Levitan et al. (2011) explicitly showed the link between the hot spot and the variability for PTF1J0719+4858, but the variability in quiescence has been observed in several AM CVn systems (e.g., Patterson et al. 1997; Wood et al. 2002).

The origin of the 2012 May variability is more difficult to determine. PTF1J1919+4815 was in outburst at the time the data was obtained (see Figure 5.3) and this would typically indicate the presence of superhumps (as seen in the CHIMERA data; see Section 5.3.1.1). Superhumps, however, typically have a period slightly longer than the orbital period (Patterson et al. 2005) and hence should be out of phase with the eclipse.

In this case, the eclipse in the 2012 May data is at the same phase with respect to the luminosity increase as in the 2012 July data. With fewer than two hours of data, it is impossible to measure the period of the variability with sufficient precision to distinguish between the orbital period and any slightly longer superhump period. Hence, we cannot say whether this variability is from the hot spot (thus indicating the lack of superhumps for part of the outburst; see, e.g., C11) or a chance superposition of the orbital period and the superhump period (as can be seen, for example, in Figure 3 of C11 for SDSSJ0926+3624).

5.3.1.3 Orbital Period Analysis

We stress that while the eclipse feature is certainly not strong, it is stable and repeating over data sets obtained with two different telescopes and over a time span of over 10 months, as well as in both quiescent and outburst states of PTF1J1919+4815. We thus conclude that this is an eclipse of the hot spot and proceed with a period analysis.

Outbursting AM CVn systems have been observed to show photometric variability at
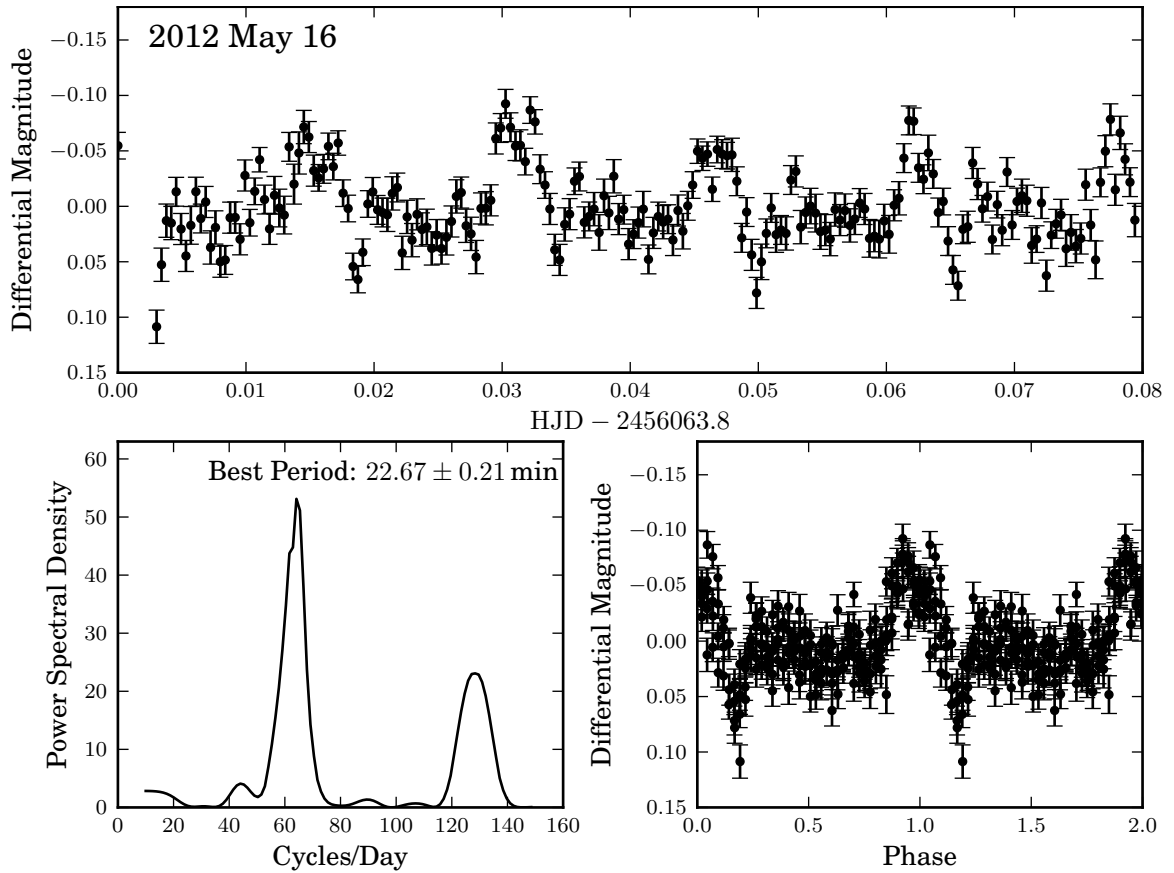
Figure 5.5 A high-cadence light curve of PTF1J1919+4815 observed by the Lick 3-m on 2012 May 16. The top panel is the light curve, the bottom-left panel is a periodogram of the light curve, and the bottom-right panel is the light curve folded on the best period. The eclipse is clearly visible in the data presented here. It is unknown whether the variability is due to superhumps or the hot spot.
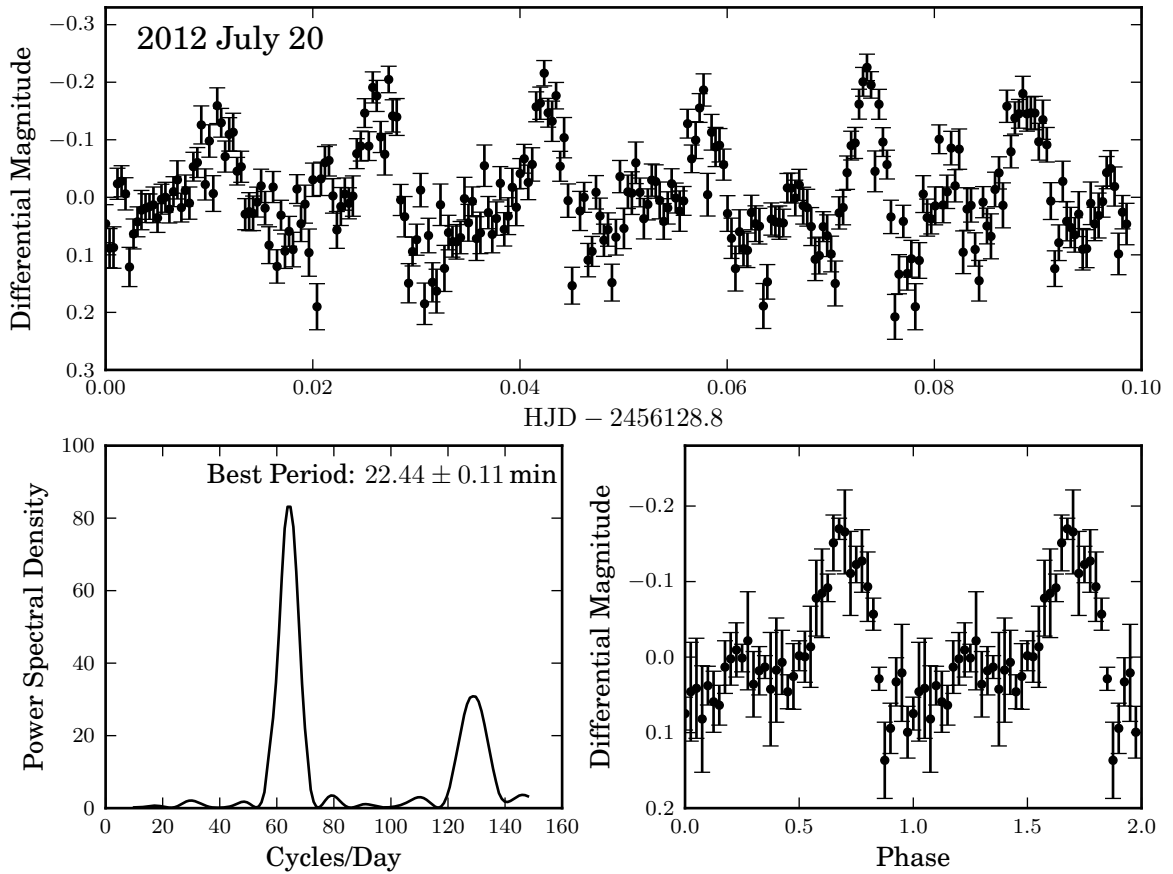
Figure 5.6 A high-cadence light curve of PTF1J1919+4815 observed by the Lick 3-m. This light curve is from 2012 July 20. The top panel is the light curve, the bottom-left panel is a periodogram generated from the light curve, and the bottom-right panel is the light curve phased-binned on the best period. This light curve was taken while the system was in quiescence, and shows the quiescent variability seen in other systems and believed to be directly related to the orbital period (Levitan et al. 2011). The data from 2012 July 18 and 19 are similar.
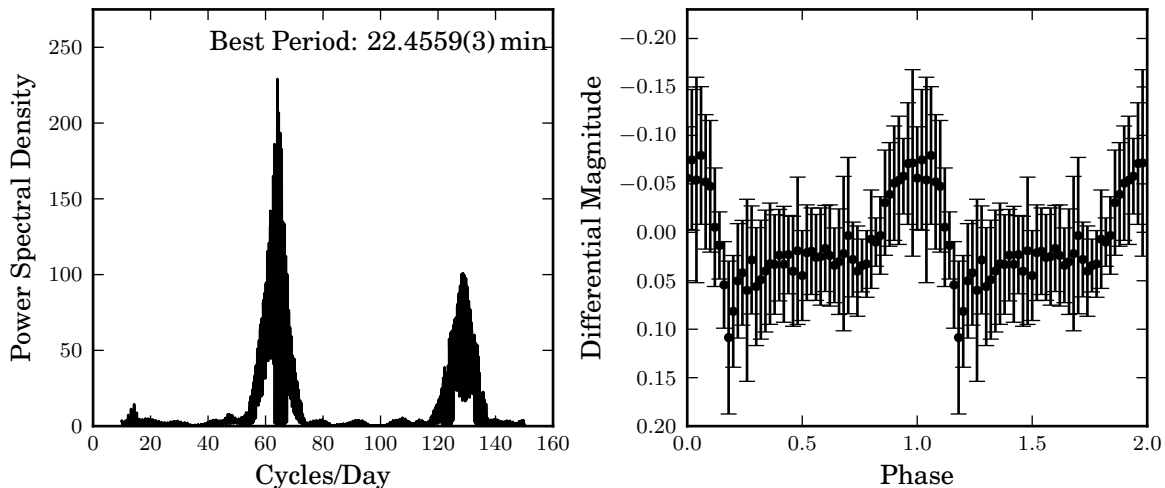
Figure 5.7 A periodogram and phase-binned light curve of all observations of PTF1J1919+4815 on the Lick-3m. The light curve is folded at a period of 22.4559 min, the highest peak in the periodogram. The eclipse is visible at an orbital phase of ∼1.2.

two periods, one in outburst (from the superhumps) and one in quiescence (likely from the hot spot; Levitan et al. 2011). We begin our analysis with the 2012 July data, which, being in quiescence, should show variability at the orbital period of the system. The best periods obtained from the individual light curves were 22.41 ± 0.05 min and 22.44 ± 0.11 min for the nights of 2012 July 18 and 2012 July 20, respectively. If we analyze all the 2012 July data simultaneously, we find a best period of 22.46 ± 0.09 min. Finally, if we analyze all data from 2012 May, June, and July simultaneously, we find a best period of 22.4559(3) min. All errors are calculated from Monte Carlo simulations, as described in Section 5.2.3, and all calculations were made using the HJD's.

Given the agreement in the periods measured from these light curves, we propose 22.4559(3) as the orbital period of PTF1J1919+4815. We acknowledge that the error measurement may be overly optimistic, as it is from a Monte Carlo simulation and does not include systematic errors. However, it is consistent with the long baseline of observations and when all data is folded at this period, the eclipse is clearly visible (Figure 5.7).

5.3.2 Phase-resolved spectroscopy

We obtained phase-resolved spectroscopy on six separate nights, although the outburst state was different for almost every one of these nights (see Figure 5.3 and Table 5.1). The most common role of phase-resolved spectroscopy in ultra-compact binaries is to identify

the orbital period by looking for the "S-wave" produced by the projected motion of the hot spot (Nather et al. 1981). However, the presence of an eclipse allows us to directly measure the orbital period from the light curves, and to use phase-resolved spectroscopy for verification of the orbital period.

The S-wave is typically best visible by converting the individual spectra around He lines into velocity space, and phase-binning the spectra into a trailed spectrum. For brighter and longer-period systems, the S-wave is often visible in the folded, trailed spectra of individual lines, while for fainter and/or shorter-period systems, the S-wave is often not visible until multiple lines are combined (see, e.g., Kupfer et al. in press for examples of both).

The rapid changes between quiescent and high states in PTF1J1919+4815 (and the resulting changes in the spectrum) mean that we need to analyze these nights separately. We initially attempted to find an orbital period using the standard blue-over-red method (Nather et al. 1981), but failed to find one in any of the data sets. This was surprising, as even fainter systems with less data have had their orbital periods successfully identified. For example, Levitan et al. (2013) found a faint S-wave in a $g' > 22$ AM CVn system with a similar amount of data as what we obtained for PTF1J1919+4815.

With no strong period found in the spectra, we used the period determined from the photometry (Section 5.3.1) to plot trailed, folded spectra as well as a Doppler tomogram (Marsh & Horne 1988) for the data from each night. The latter is the best tool to confirm the presence of a hot spot, as it concentrates all flux moving at one velocity into a (K_x, K_t) projection. Only the 2012 June 13 and 2012 Aug 16 data showed an S-wave in the folded spectrum (Figure 5.8) and a hot spot in the tomogram (Figure 5.9). However, the S-wave is negative (indicating a decrease in flux) and at very low velocities, inconsistent with the velocities of a hot spot for a high, or even moderate, inclination system. The Doppler tomogram shows a strong negative flux feature consistent with the velocity of the negative S-wave, as well as a faint hot spot at a reasonably high velocity. We discuss these features further in Section 5.4.3.

5.3.3 Long-term Photometric Variability

We explore the long term photometric variability of PTF1J1919+4815 using the 355 photometric measurements over $\sim$200 d. We identify the presence of super-outbursts and the much shorter normal outbursts. The latter, in particular, appear to last $\sim$1 d and were
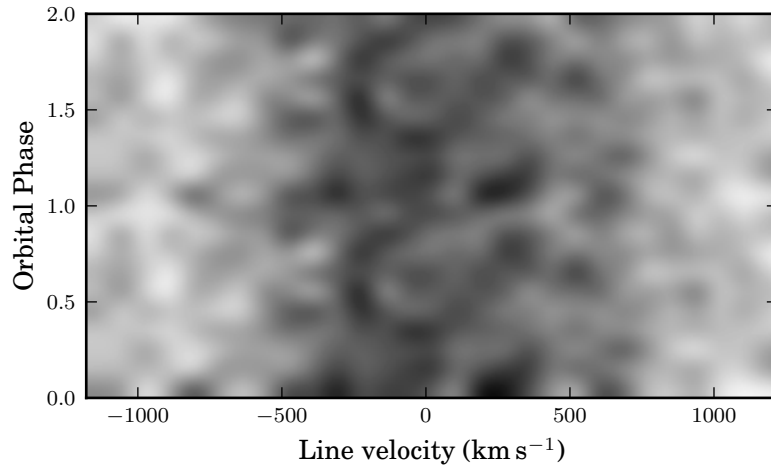
Figure 5.8 The trailed, folded spectra from 2012 June 13 and 2012 August 16 folded at a period of 22.456 min. The He I $\lambda\lambda 4387, 4471, 4921,$ and 5015 lines were used. Unlike other AM CVn systems, no strong, positive S-wave is present, but a weak negative flux S-wave is present with a low amplitude.
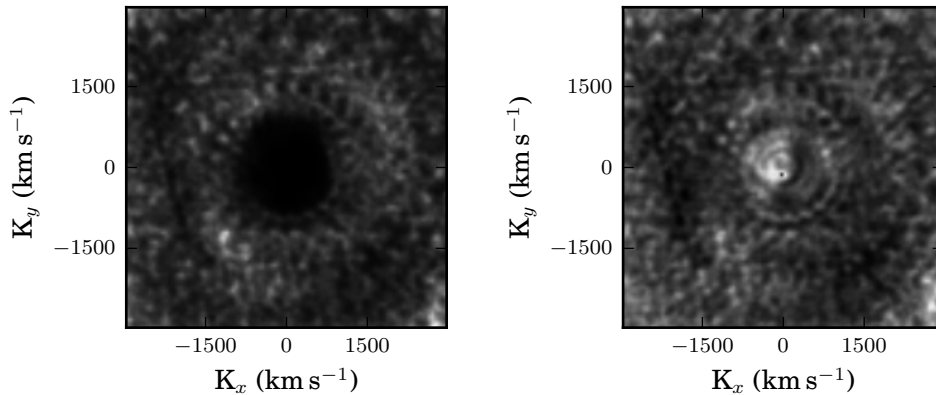
Figure 5.9 **Left:** Doppler tomogram generated from data taken on 2012 June 13 using the He I $\lambda\lambda 3888, 4026, 4921,$ and 5015 lines and the He II $\lambda 4686$ line. Doppler tomograms re-project spectroscopic data into Keplerian-velocity space — all flux from areas moving with the same velocity will be projected onto the same spot on the tomogram. This allows us to look for features such as a hot spot that would be at one velocity. For this tomogram, we identify an extremely weak hot spot in the lower-left corner. The lack of intensity is unusual for an AM CVn system.
Right: The tomogram shown above, divided by its average value. A strong source of negative flux (i.e., optically thick region) is seen at a low velocity, something that has not been seen for other AM CVn systems.

observed to occur 2–3 times between super-outbursts. We label examples of each in Figure 5.3.

We look for a super-outburst recurrence time by running a periodogram analysis of the data from the P60, consisting of data over the course of almost one year and covering approximately 5 super-outburst cycles. In Figure 5.10 we show the periodogram and a phase-folded light curve of the data. Surprisingly, when the light curve is folded at the strongest peak in the periodogram ($P_{so} = 36.8 \pm 0.4\,\mathrm{d}$), the super-outburst is well-defined, with only minor variation in its length. The duration of the super-outburst is $\sim 13\,\mathrm{d}$ and its amplitude (peak luminosity minus quiescent luminosity) is $\sim 3\,\mathrm{mag}$.

5.3.4 Median Spectra and Long-term Variability

AM CVn systems are known to have significant changes in their spectra corresponding to their different states. PTF1J1919+4815, with its frequent changes between outburst and quiescence, provides a good opportunity to consider the changes in spectra. In Figure 5.11 we present median spectra from three nights. In particular, these spectra shows the evolution of the spectrum from the emission-line spectrum that AM CVn systems exhibit in quiescence (the 2012 June 13 spectrum) to the outburst spectrum showing absorption lines (the 2012 June 20 spectrum). The figure also shows the spectrum taken on 2012 August 28, at the start of a super-outburst (see Figure 5.3), which shows a distinct lack of features. We present equivalent widths of the significant lines identified in the outburst and quiescent spectra in Table 5.2.

5.4 Discussion

In this section, we use the measurements of PTF1J1919+4815 to understand its structure and to compare this system to other known AM CVn systems. In particular, we consider the super-outburst cycle (Section 5.4.1), the system geometry (Section 5.4.2), and the hot spot and structure of PTF1J1919+4815 (Section 5.4.3). We present a summary of system properties in Table 5.3.
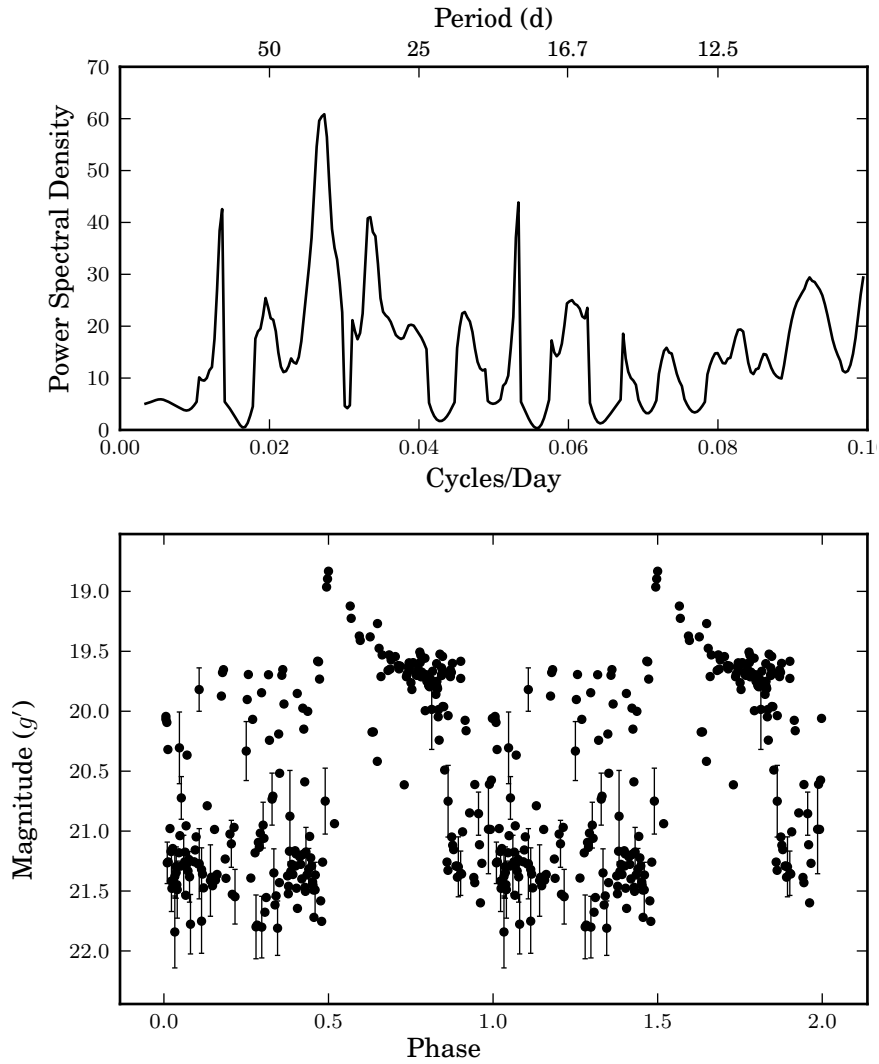
Figure 5.10 **Top:** A periodogram of the PTF1J1919+4815 long-term P60 photometry data. The highest peak is at 36.81 d.

Bottom: A light curve of the long-term P60 photometry folded at the peak period in the above periodogram. The folded light curve shows a very consistent super-outburst over the 5 super-outburst cycles ($\sim$200 d) observed. The normal outbursts, however, do not coincide with each other. Some evidence is present for "dips" during the middle of the super-outburst, as reported by (Ramsay et al. 2012). However, the dips seen here are non-coherent, and it is unknown if these dips are related to those seen by Ramsay et al. (2012). The peak of the super-outburst is set to a phase of 0.5.
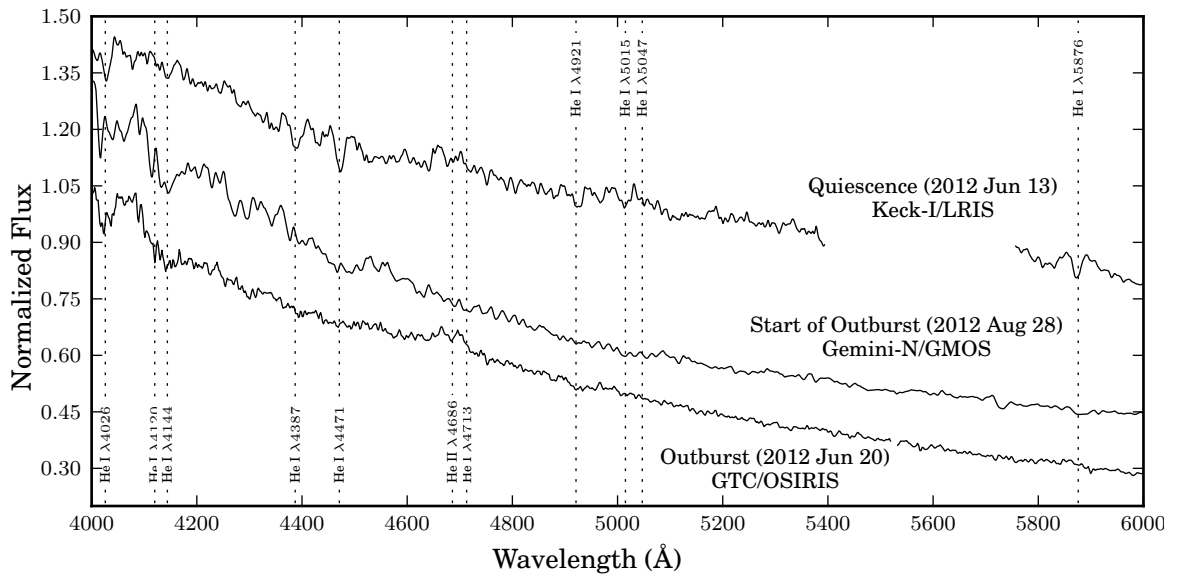
Figure 5.11 The median spectra from three nights: 2012 June 13, 2012 August 28, and 2012 June 13, arranged in this order from top to bottom. The flux of the first two spectra is shifted, respectively, 0.4 and 0.2 upwards from their normalizations. The most prominent He emission lines are shown. The first spectrum is of the system in quiescence and shows the He emission lines that AM CVns are known for. The other spectra are from the outburst state—in particular, the second spectrum shows few features and is from the initial rise to outburst, while the third spectrum is from the plateau phase and shows the absorption line features that have been observed for other systems in outburst.

Table 5.2.   Equivalent widths of prominent lines in PTF1J1919+4815

Line	Quiescence	Outburst
He I 3705	$\cdots$ [a]	4.4 ± 0.2
He I 3819	-2.7 ± 0.5	3.9 ± 0.2[b]
He I 3888	-4.9 ± 0.4	
He I 3964	-1.1 ± 0.4	6.8 ± 0.2[c]
He I 4026	$\cdots$ [a]	
He I 4120/4143	X	4.4 ± 0.2
He I 4388	-0.5 ± 0.4	1.5 ± 0.1
He I 4471	-2.2 ± 0.4	3.3 ± 0.2
He II 4685	-3.4 ± 0.4[d]	-0.5 ± 0.1
He I 4713		$\cdots$ [a]
He I 4921	$\cdots$ [a]	2.8 ± 0.2
He I 5015	-3.6 ± 0.4	1.8 ± 0.2
He I 5875	-2.7 ± 0.6	1.9 ± 0.3
He I 6678	2.6 ± 0.5	$\cdots$ [e]
He I 7065	-2.1 ± 0.5	X

Note. — Quiescent equivalent widths are measured from the medium spectrum taken on 2012 August 16. Outburst equivalent widths are measured from the median spectrum taken on 2012 August 17. An X indicates that the line is not detectable above the noise level of the spectrum obtained.

[a]Line present but insufficient S/N to measure.

[b]Combined equivalent width of He I 3819 and He I 3888.

[c]Combined equivalent width of He I 3964 and He I 4026.

[d]Combined equivalent width of He II 4685 and He I 4713.

[e]Line present but contaminated with atmosphere.

Table 5.3. System properties of PTF1J1919+4815

U^a	19.814 ± 0.048
g^a	20.155 ± 0.016
r^a	20.522 ± 0.065
i^a	20.409 ± 0.121
Orbital period	$22.4559(3)\,\mathrm{min}$
Super-outburst Recurrence Time	$36.8 \pm 0.4\,\mathrm{d}$
Super-outburst Amplitude	$\sim 3\,\mathrm{mag}$
Super-outburst Duration	$\sim 13\,\mathrm{d}$
Inclination^b	$74° < i < 78°$

[a]Photometric measurements are from the Kepler INT Survey DR2 (Greiss et al. 2012a,b) and are typical of the quiescent values for the system.

[b]These values assume that the radius of the accretion disk, $a = 0.25 R_\odot$. See Section 5.4.2 for further details.

5.4.1 Super-Outburst Recurrence Time

Levitan et al. (2011) and Ramsay et al. (2012) proposed that the super-outburst frequency of short-period outbursting AM CVn systems ($P_{orb} < 27$–$30\,\mathrm{min}$) is proportional to the orbital period. In Section 5.3.3 we showed that the super-outburst recurrence time was $\sim 37\,\mathrm{d}$. This is shorter than the system with the next shortest orbital period, CR Boo (orbital period: $24.5\,\mathrm{min}$; super-outburst length: $\sim 48\,\mathrm{d}$; Patterson et al. 1997; Kato et al. 2000), and hence, the trend appears to continue.

The most noticeable feature of the long-term light curve (see Figures 5.3 and 5.10), however, is the regularity of super-outbursts. This is in contrast to most other AM CVn systems with short orbital periods, where the super-outburst cycle length has been seen to vary by up to 15 days (10–20% of the cycle length; see Ramsay et al. 2010 and Ramsay et al. 2012 for KL Dra and Levitan et al. 2011 for PTF1J0719+4858). Our period analysis in Section 5.3.3 indicates an error in the super-outburst recurrence time of only $0.8\,\mathrm{d}$, substantially smaller than the variability seen in other systems.

On the other hand, the normal outbursts in PTF1J1919+4815 do not seem to recur at regular intervals, although this may be partially a result of few measurements since the events do not appear to last more than 1–2 d, based on the long-term light curve. The length of the normal outbursts is consistent with that observed for CR Boo (Kato et al.

2000) and PTF1J0719+4858 (Levitan et al. 2011).

5.4.2 Eclipse and Geometric Configuration

We now consider the source of the eclipse discussed in Section 5.3.1 and what we can learn from it. We believe that the source of the eclipse is not the accretor but the accretion disk hot spot. Typically, an eclipse of the accretor would produce two eclipses (see, e.g., C11) — a deep one when the donor eclipses the accretor, and a shallower one when it eclipses the hot spot. Here we only see conclusive evidence for one. We do acknowledge the possibility that both the accretor and hot spot may be eclipsed almost simultaneously (see, e.g., IP Peg; Copperwheat et al. 2010). However, the depth of PTF1J1919+4815's eclipse is only ∼10%, which is consistent with the eclipse of the hot spot seen in SDSSJ0926+3624, whereas ∼70% of the luminosity of an AM CVn system is believed to be from the accretor (C11).

The lack of an accretor eclipse prohibits the full modeling of the system. It also prevents us from measuring any change in the orbital period for this system, as the uncertainty of the disk radius and its likely change due to the presence of outbursts will overwhelm any expected change due to orbital evolution. We can, however, attempt to place limits on the inclination of PTF1J1919+4815.

To find the possible inclinations of PTF1J1919+4815, we must make assumptions about the values for the radius of the accretor and the disk and the masses of the donor and accretor. We do this by assuming that PTF1J1919+4815 is of similar evolutionary origin as the only AM CVn systems for which these parameters have been measured: SDSSJ0926+3624 ($P_{orb} = 28.558\,\mathrm{min}$; C11). We caution that AM CVn systems are believed to have several possible evolutionary pathways (Nelemans et al. 2001) and that no conclusive evidence has been found that can differentiate a system's origin (Roelofs et al. 2007a; Nelemans et al. 2010).

We must first account for the different orbital periods between SDSSJ0926+3624 and PTF1J1919+4815 and thus the mass transferred between the accretor and donor. We assume that the evolution of the systems is driven by two major components: gravitational wave radiation and mass transfer from the donor to the accretor (Faulkner et al. 1972b). From C11, the parameters of SDSSJ0926+3624 are: $M_1 = 0.85 M_\odot$, $M_2 = 0.035 M_\odot$, $R_1 = 9.7 \times 10^{-3} R_\odot$, and $P = 28.558\,\mathrm{min}$. We solve the relevant equations to find that the total

amount of mass transferred between $P = 22.456\,\text{min}$ and $P = 28.558\,\text{min}$ is $\sim 0.01 M_\odot$.

Given that the mass transfer is not large enough to significantly change the accretor's properties, we adopt the radius of the accretor from SDSSJ0926+3624 to be that of the accretor in PTF1J1919+4815. The donor's radius will be that of the Roche Lobe as a first estimate, at the given period for the given mass ratio. Using the calculated masses of PTF1J1919+4815 with the approximation in Eggleton (1983), we find that $q = 0.053$, $a = 0.25 R_\odot$, and $r_L = 0.043 R_\odot$. The last measurement needed is the radius of the disk. Based on the measurements of SDSSJ0926+2624, we assume a disk radius of $R_{disk} \approx 0.35a$. The derived values in C11 vary between observing runs, and since the size of the disk is expected to change between outburst and quiescence, we believe this is a reasonable, first assumption. We can constrain the inclination by finding for which inclinations the donor star will overlap the bright spot (assumed to be a point source) but not the accretor. Combining the radii of disk, donor, and accretor, we can constrain the inclination to $74^\circ < i < 78^\circ$.

We caution that these limits on inclination are based on a specific reference system, and we consider the impact of several parameters on the properties of the system. The upper limit on i is primarily related to the accretor and donor masses. However, their masses are constrained by the initial conditions of AM CVn system formation and as such are not likely to change significantly even with moderate changes of the initial masses. The lower bound, however, is significantly affected by the radius of the disk. If, for example, the radius of the disk was $0.5a$, the lower bound would drop to 70°. Had the inclination been greater than the upper limit here, an eclipse of the white dwarf should have been observable. Conversely, an inclination of less than the lower limit would result in no eclipse of either the hot spot or the accretor.

5.4.2.1 Number of Eclipsing AM CVn Systems

One peculiarity of the AM CVn systems is the relative scarcity of eclipsing examples. In Section 5.4.2, we constrained the inclination of PTF1J1919+4815 to the range $74^\circ < i < 78^\circ$. This indicates that in $>20\%$ of systems the accretor should be eclipsed, and an additional $\sim 7\%$ of systems should show an eclipse of the hot spot only, as is the case here. These calculations assume a random distribution of inclinations and an observed inclination distribution of $\sin(i)$. With the number of AM CVn systems rapidly approaching 40, it is somewhat surprising that only one system has shown an eclipse of the accretor and only

one other a partial eclipse. The rate of observed eclipsing systems, $\sim$5% is a factor of five lower than would be expected. Even with small-number statistics, one would expect at least 5 fully eclipsing systems. Incomplete photometry for the known systems may be a partial explanation.

5.4.3   Hot Spot and System Structure

The phase-resolved spectroscopy of PTF1J1919+4815 leads to two significant questions: what is the negative feature, and why is there no strong hot spot? We have little explanation of the former, beyond stating that if it is real, it must be an optically thick area of the system. We do know that the negative feature cannot be the donor, as the donor's velocity should be $\sim$800 km s^{-1}, while the velocity of the negative feature is <200 km s^{-1}.

The lack of a strong hot spot is consistent with other similar systems. Of the five known AM CVn systems with $20\,\mathrm{min} < P_{orb} < 27\,\mathrm{min}$, only V803 Cen (Roelofs et al. 2007b) and PTF1J0719+4815 (Levitan et al. 2011) have known S-waves, and both required combining multiple He lines to identify the S-wave despite a significant amount of data.

A more massive donor, as is expected with shorter-period systems (and, hence, younger systems), should result in a higher mass transfer rate from the donor to the disk. However, this does not guarantee a brighter hot spot. If the disk radius is the same between shorter and longer orbital period systems, then this will, in fact, produce a more luminous hot spot since more He interacting with the disk should increase the luminosity. But if the disk radius is larger due to the increased mass transfer rate, then the distance from the donor to the edge of the disk would be shorter and thus less gravitational energy will be gained by the transferred mass and later released. Hence, it is difficult to establish the cause of the decreased contrast between the disk and the hot spot.

5.5   Conclusions

We have established PTF1J1919+4815 as an eclipsing AM CVn system from its He-rich and H-deficient spectrum, its phenomenological behavior, and its photometrically determined period. Its orbital period was measured to be 22.4559(3) min, but we only found an extremely weak hot spot in the S-wave and Doppler map, for unknown reasons. PTF1J1919+4815 shows a well-defined super-outburst that is 36.8 ± 0.4 d. Such a non-

variable recurrence time is atypical for AM CVn systems. We used these measurements to constrain the inclination of the systems given assumptions about its evolution and to consider the geometric structure of the system.

Chapter 6

Long-term Photometric Behavior of Outbursting AM CVn Systems[*]

DAVID LEVITAN[1], PAUL J. GROOT[1,2], THOMAS A. PRINCE[1], SHRINIVAS R. KULKARNI[1], RUSS LAHER[3], ERAN O. OFEK[4], BRANIMIR SESAR[1], AND JASON SURACE[3]

[1] Division of Physics, Mathematics, and Astronomy, California Institute of Technology, Pasadena, CA 91125, USA.

[2] Department of Astrophysics/IMAPP, Radboud University Nijmegen, PO Box 9010, NL-6500 GL Nijmegen, the Netherlands.

[3] Spitzer Science Center, MS 314-6, California Institute of Technology, Pasadena, CA 91125, USA.

[4] Benoziyo Center for Astrophysics, Faculty of Physics, Weizmann Institute of Science, Rehovot 76100, Israel.

Abstract

The AM CVn systems are a class of He-rich, post-period minimum, semi-detached, ultra-compact binaries. We present combined photometric light curves from the LINEAR, CRTS, and PTF synoptic surveys to study photometric variability of these systems over an almost 10 yr period. In particular, these light curves provide a much clearer picture of the outburst phenomena that these systems undergo. We characterize the photometric behavior of most known outbursting AM CVn systems and establish a relation between their outburst properties and the systems' orbital periods. We also explore why some systems have only shown a single outburst so far and expand the previously accepted phenomenological states of AM CVn systems. Finally, we consider the number of AM CVn systems that should be present in CSS-like and PTF-like surveys.

6.1 Introduction

The AM CVn systems are a rare class of ultra-compact, post-period minimum stellar binaries with some of the smallest separations known. Ranging in orbital period from 5 to 65 minutes, they are believed to be composed of a relatively massive white dwarf accreting from a much lower mass (semi-)degenerate helium-transferring donor (Paczyński 1967; Faulkner et al. 1972b). We refer the reader to Nelemans (2005) and Solheim (2010) for reviews.

As a result of their semi-detached nature, most AM CVn systems show inherent photometric variability on multiple timescales, believed to be largely dependent on the orbital period and mass transfer rate of the particular system. AM CVn system phenomenological behavior has been separated into roughly two states — a "high" state corresponding to high rates of mass transfer and an optically thick disk — and a "quiescent" state corresponding to low rates of mass transfer and an optically thin disk. The former is generally associated with those systems having orbital periods $< 20\,\mathrm{min}$ and the latter with those having orbital periods $> 40\,\mathrm{min}$. High state systems exhibit superhump behavior like that found in some cataclysmic variables (CVs; Warner 1995) with photometric variability on the orbital timescale at an amplitude of $\sim 0.1\,\mathrm{mag}$ (e.g., Patterson et al. 2002).

Systems with orbital periods between $\sim 20\,\mathrm{min}$ and $\sim 40\,\mathrm{min}$ have been observed to alternate between the high and quiescent states with behavior similar to that of super-outbursts in dwarf novae and are thus called "outbursting" AM CVn systems (Ramsay et al. 2012). In outburst, these systems are typically 3–5 mag brighter than in quiescence and these outbursts have been observed to recur on timescales from $\sim 40\,\mathrm{d}$ to several years. Some systems, particularly those at the short-period end, have also shown shorter, "normal" outbursts that last 1–1.5 d and are typically seen 3–4 times between the longer "super"-outbursts (e.g., Kato et al. 2000; Levitan et al. 2011). Given the much longer cadences for the data presented here, we are interested only in super-outbursts and will refer to them as just outbursts, unless explicitly specified.

One of the outstanding problems with AM CVn systems is the lack of an observationally-verified population distribution. This is caused, in part, by the lack of known systems; the known sample remained under a dozen for over 30 years. The availability of the Sloan Digital Sky Survey (SDSS), and, in particular, its spectroscopic database, allowed for the first systematic search for AM CVn systems. Seven new systems were discovered in the

SDSS spectroscopic database from their He-rich, H-deficient spectra (Roelofs et al. 2005; Anderson et al. 2005, 2008).

Although successful, the search through the SDSS spectroscopic survey was hampered by the low spectroscopic coverage of bluer stars by the SDSS (Roelofs et al. 2007d). Roelofs et al. (2009) showed that the known AM CVn systems occupied a relatively sparse region of color-color space, and proposed to use the photometric data from the SDSS to select candidates for spectroscopic classification. Seven additional systems were found as part of this effort (Roelofs et al. 2009; Rau et al. 2010; Carter et al. 2013a).

However, despite the successful discovery of fourteen new systems from the combined SDSS searches, the population density question remains to be answered. Roelofs et al. (2007d) used the original SDSS sample of AM CVn systems to show that the population synthesis estimate by Nelemans et al. (2001); Nissanke et al. (2012) were high by an order of magnitude. The re-calibrated population density was used to predict that 40 new systems would be discovered by the follow-up project (Roelofs et al. 2009). Instead, this search yielded only seven new systems, implying that the original population estimates were a factor of 50 too high (Carter et al. 2013a). No explanation for this difference has been given in the literature.

More recently, a significant number of AM CVn systems has been found from their photometric variability using large-area synoptic surveys. In particular, the Palomar Transient Factory (PTF) has systematically identified 7 new AM CVn systems from their photometric outbursts in a color-independent manner (Levitan et al. 2011, 2013, Chapter 5).

The goal of the PTF's search for AM CVn systems is to provide a second set of systematically identified systems, determined without the use of color-selection, to verify current population models. However, in order to draw any conclusions on the population of AM CVn systems from an outburst search, the outburst phenomena itself needs to be better understood. It is believed that the outburst mechanism in AM CVn systems can be described by adjustments to the same disk instability model (DIM) as that used to model the outbursts of CVs (Lasota 2001). Recent work has, in fact, shown that the outburst in AM CVn systems can be modeled using the DIM (Kotko et al. 2012), although the changes in outburst patterns for AM CVn systems (e.g., CR Boo; Kato et al. 2000, 2001) are not yet explained.

Efforts to understand outbursts based on observations have been hampered by the lack

of long term light curves for most AM CVn systems. Ramsay et al. (2012), hereafter R12, have performed the most substantial work in this area. They used the Liverpool Telescope to monitor 16 AM CVn systems for 2.5 years. However, the use of dedicated observations provided only a short baseline, and even several known outbursting systems were not detected in outburst during their monitoring. Only a few systems have been monitored for more than a few years (most notably CR Boo; Honeycutt et al. 2013), but the variety of outbursts, as we describe in this paper, requires data for more than one system.

Earlier work on individual systems has provided some information on their outburst recurrence times. Both Levitan et al. (2011), hereafter L11, and R12 differentiated between shorter-orbital period outbursting systems ($20 \, \mathrm{min} < P_{orb} < 27 \, \mathrm{min}$) and longer-orbital outbursting period systems ($27 \, \mathrm{min} < P_{orb} < 40 \, \mathrm{min}$). They noted that the former of these groups has fairly well established recurrence times of less than a few months while the latter group has either very poorly determined recurrence times or no determined recurrence time.

Here, we extend the work of R12 by using three separate synoptic surveys to extend our baseline to almost $10 \, \mathrm{yrs}$ for many systems. This allows us, for the first time, to consider the outburst frequency of those systems outbursting only once every several years. Additionally, since we use non-dedicated observations from large-area surveys, we are able to analyze recently discovered AM CVn systems by drawing on past data for these systems. We do note that a significant disadvantage of synoptic surveys is the often erratic coverage and the much longer cadences.

This paper is organized as follows. We begin by describing the surveys, data processing, and analysis methods in Section 6.2. We review the known outbursting AM CVn systems in Section 6.3 and present our composite light curves, along with initial analysis of the outbursts. In Section 7.5, we discuss AM CVn system evolution, outburst properties, and make predictions of the observed number of systems in current synoptic surveys. We summarize our conclusions in Section 6.5.

6.2 Observations and Reduction

6.2.1 Data Sources

The observations presented in this paper come from three synoptic surveys: the Palomar Transient Factory (PTF), the Catalina Real-Time Sky Survey (CRTS), and Lincoln Near Earth Asteroid Research survey (LINEAR). In the remainder of this section, we summarize each of these surveys, including an overview of the survey parameters, details of data processing, and a discussion of the limiting magnitudes presented here for the survey. The limiting magnitudes are particularly important for this project, as most known outbursting AM CVn systems are extremely faint in quiescence.

6.2.1.1 Palomar Transient Factory

The PTF[1] (Law et al. 2009; Rau et al. 2009) used the Palomar 48" Samuel Oschin Schmidt Telescope to image $7.3 \deg^2$ of the sky simultaneously using eleven 2048×4096 pixel CCDs. The typical PTF cadence of 3–5 d was primarily chosen to discover supernovae. Certain areas of the sky have been observed with a higher cadence — from 1 day down to 10 minutes. Typically, two individual exposures separated by 30 minutes are taken every day to eliminate asteroids and artifacts. The PTF observes in either R-band or g'-band, with an $H\alpha$ survey during full moon. The 5σ limiting magnitude of the survey is $R \sim 20.6$ and $g' \sim 21.0$ with saturation around 14th magnitude. The PTF data is the best calibrated and deepest of the large-area synoptic surveys used here. However, it is also the youngest and has the least amount of data.

The PTF data are processed through the so-called photometric pipeline which uses aperture photometry and prioritizes photometric accuracy over processing speed (Laher et al. in prep). After de-biasing and flat-fielding, catalogs are generated using Sextractor (Bertin & Arnouts 1996). Photometric calibration relative to SDSS fields observed in the same night provides an absolute calibration accuracy of better than $\sim$2–3% on photometric nights, but this can be significantly inaccurate on nights with changing weather conditions (Ofek et al. 2012). Relative photometric calibration is able to correct for such changes as well as improve the precision of photometry at the bright end to 6–8 mmag and at the faint

---

[1] http://www.ptf.caltech.edu/

end to $\sim0.2\,$mag. The basic approach of the algorithm is described in Ofek et al. (2011) and Levitan et al. (2011) with PTF-specific details to be published at a future time. Although this algorithm is primarily a relative calibration algorithm, it simultaneously calibrates to an outside absolute scale. For the PTF data, we use the median value of the absolute-calibrated photometric measurements.

The photometric pipeline produces two limiting magnitude estimates for each exposure as part of the calibration process. The first estimate defines the limiting magnitude as the magnitude at which 95% of sources in a deep co-added image are present in an individual exposure. The second estimate is a theoretical estimate of the maximum magnitude at which a 5σ detection is possible. Typically, this 5σ detection limit is reached $\sim0.5\,$mag fainter than the 95% limiting magnitude estimate, but we have found it to be unreliable in poor weather conditions, in part because it relies on the zero-points calculated from the comparison to SDSS, which themselves are unreliable in poor weather.

6.2.1.2 Catalina Real-Time Transient Survey

The CRTS[2] (Drake et al. 2009) uses three separate telescopes: the Catalina Sky Survey $0.7\,$m Schmidt (CSS), the Mount Lemmon Survey $1.5\,$m (MLS), and the Siding Spring Survey $0.5\,$m Schmidt (SSS). The fields of view are, respectively, $8.1\,\mathrm{deg}^2$, $1.2\,\mathrm{deg}^2$, and $4.2\,\mathrm{deg}^2$, with corresponding limiting magnitudes in V of 19.5, 21.5, and 19.0. The majority of data currently available is from the CSS, and has a typical cadence of one set of 4 exposures per night per field separated by $10\,$min, repeated every 2 weeks.

The CRTS DR2 public release provides both the ability to see all exposures covering a given part of the sky and the ability to download light curves around a set of coordinates. We began by downloading the list of exposures at each location, as well as the light curve for the target, from the "photcat" catalog. We retained only those exposures with $1'' < FWHM < 4''$ and exposure times between $1\,$s and $120\,$s. We downloaded light curves of all objects within $\sim0.3\,\mathrm{deg}^2$ of the center of the CRTS pointing for these exposures.

Although we would prefer to estimate the limiting magnitude with the same method as that used for PTF exposures, the lack of publicly available deep co-added images from the CRTS precludes this. We thus estimate the 5σ limiting magnitude of each exposure to be the faintest star detected in this set of light curves. We then subtract $0.5\,$mag to

---

[2]http://crts.caltech.edu/

this limiting magnitude to convert this into a "95% limiting magnitude", as defined for the PTF. These estimates are typically consistent with the average limiting magnitudes of the CRTS (Drake et al. 2009).

A few of the AM CVn systems observed by the CRTS are too faint to be detected in the default "photcat" catalog. This catalog is the set of sources identified in deep co-added CRTS images, as part of the CRTS pipeline. Detections not associated with this set of sources is in the "orphancat" catalog (A. Drake, priv. comm.). In these cases, we assumed any detection in the orphancat within $3.5''$ ($\sim 1.5 \times$ the pixel scale of the CSS, similar to criteria used for PTF source association) of the target coordinates was a detection of our target.

6.2.1.3 Lincoln Near Earth Asteroid Research survey

The Lincoln Near Earth Asteroid Research survey[3] (LINEAR; Stokes et al. 2000) used two telescopes at the White Sands Missile Range for a synoptic survey primarily targeted at the discovery of near Earth objects. Each exposure covered $\sim 2 \deg^2$ to a 5σ limiting magnitude of $r' \sim 18$. Sesar et al. (2011) re-calibrated the LINEAR data using the SDSS survey, resulting in ~ 200 unfiltered observations per object (~ 600 observations for objects within $\pm 10°$ off the Ecliptic plane) for 25 million objects in the $\sim 9,000 \deg^2$ of sky where the LINEAR and SDSS surveys overlap (roughly, the SDSS Galactic cap north of Galactic latitude $30°$ and the SDSS Stripe 82 region). The photometric precision of LINEAR photometry is ~ 0.03 mag at the bright end ($r' \sim 14$) and ~ 0.2 mag at $r' = 18$ mag.

The published LINEAR data set contains information only on source detections, and provides no list of exposures for a particular field. We thus need to both determine when the target was observed, as well as the limiting magnitudes of those exposures. To identify exposures on which a particular target was not detected we downloaded light curves for all sources within $20'$ of the target. We kept only those sources that were detected on at least 90% of the exposures in which the target was detected. We identified the MJDs of all exposures on which this group of sources appeared and thus found the non-detections of the target by comparing this list to the list of target detections.

To estimate limiting magnitudes when the target was not detected, we used a similar

---

[3]Public access to LINEAR data is provided through the SkyDOT web site (`https://astroweb.lanl.gov/lineardb/`).

technique as we did with the CRTS data. Since the center of the frame coordinates is not available, we used only those stars earlier identified to be near the target. We estimate the 95% limiting magnitudes to be 0.5 mag brighter than the faintest star observed for each exposure.

6.2.1.4 Palomar $60''$ Data

Some data for CR Boo was obtained using targeted observations with the Palomar $60''$ (P60) telescope. This data was de-biased, flat-fielded, and astrometrically calibrated with the P60 Automated Pipeline (Cenko et al. 2006). Photometric measurements were made using the STARLINK package AUTOPHOTOM and calibrated using the relative photometric algorithm described in L11. The absolute scale was tied to the SDSS DR9 catalog (Ahn et al. 2012).

6.2.2 Light Curve Analysis

Although we use data from three different surveys, we decided to avoid jointly calibrating the light curves. The primary reason for this decision is that the wide-field nature of the surveys requires a large number of calibration sources. With the PTF photometric pipeline, we use 350–400 stars to calibrate light curves for each $\sim 0.7\,\mathrm{deg}^2$ section of the sky (that falling on one detector). Given our lack of access to the raw CRTS and LINEAR data sets, it would be difficult to find this many calibration sources for each target. Although it is possible to calibrate with fewer stars, the lack of filters for the CRTS and LINEAR surveys makes this calibration more difficult, since we would need to account for both different CCD response curves and the presence of filters. Regardless, our primary interest is in large-scale photometric variability relative to a quiescent magnitude, and even a difference of several tenths of a magnitude between surveys is acceptable.

6.2.2.1 Outburst Definitions

Although outbursts are often easy to identify by eye, a quantitative definition is necessary for a systematic study. We define an outburst to be ≥ 2 detections that are brighter than the quiescent magnitude by the greater of 0.5 mag or 3σ mag, where σ is the scatter of the light curve while the system is in quiescence. At least 2 of the detections must be within 15 d. While the light curve of the system satisfies both conditions, we consider it to

be in outburst. The quiescent magnitude is taken to be the median of the light curve or, for the faintest systems, from the literature. Additionally, for PTF, we confirmed all outburst detections by looking at the individual images. Neither CRTS nor LINEAR images are publicly available at the current time.

We estimate three properties for all outbursting systems presented here: the strength, duration and recurrence time. We define the strength of the outburst to be the difference between the peak luminosity observed and the quiescent magnitude. This is actually a lower limit on the strength, but without continuous monitoring it would be difficult to identify the actual peak magnitude. Our numbers are consistent with any that exist in the literature.

The outburst duration is even more difficult to determine, due to the infrequent sampling. When available, we used durations from the literature. When not available, we either estimated or placed an upper limit on the duration using our earlier definition of an outburst. For systems with multiple, relatively well-sampled outbursts, we used an average of outburst durations. For systems with only a few observed outbursts and poorly sampled data, we provided an upper limit based on the next detection not in outburst.

The most difficult to estimate is the recurrence time for those systems for which we observed multiple outbursts. Again, we used any published estimates if available, except as noted in Section 6.3.1. For systems with more than five outbursts, we used the time of the brightest measurement of each outburst, and estimated the recurrence time as the mean. We estimated the error as the scatter of those measurements around the median, and assumed that the outbursting behavior remained consistent throughout any gaps in the data. All systems showed a minimum outburst frequency between several outbursts, and we tested longer gaps with integer division to check for any observations at the predicted outburst times. Some systems (e.g., Section 6.3.1.4) showed extra outbursts that were on timescales of less than 5 d and outside of the normal pattern of detections. We assumed these to be normal outbursts and ignored them for the purposes of this estimation.

For those systems showing fewer than five outbursts, we estimated the recurrence time as the average time between outbursts. We assigned errors based on a propagation from the uncertainty of duration in the few outbursts observed. We tested whether the recurrence time could be our estimate divided by an integral value by looking for observations at the predicted times. We remark on any adjustments as part of our individual system descriptions in Section 6.3.1.

Table 6.1: Known AM CVn Systems

System[a]	Outbursting	Period (min)	Quiescence (g')	References
HM Cnc	N	5.36	21.1	1
V407 Vul	N	9.48	19.7	2
ES Ceti	N	10.3	17.1	3
KIC 004547333	N	15.9	16.1	4
AM CVn	N	17.1	14.2	5
HP Lib	N	18.4	13.5	6
PTF1 J191905.19+481506.2	Y	22.5	21.5	7
CR Boo	Y	24.5	17.4	8, 9
KL Dra	Y	25.0	19.1	10
V803 Cen	Y	26.6	16.9	11, 12, 6
PTF1 J071912.13+485834.0	Y	26.8	19.4	13
SDSS J092638.71+362402.4	Y	28.3	19.0	14, 15
CP Eri	Y	28.7	20.3	16
PTF1 J094329.59+102957.6	Y	30.4	20.7	17
V406 Hya	Y	33.8	20.5	18
PTF1 J043517.73+002940.7	Y	34.3	22.3	17
2QZ J142701.6–012310	Y	36.6	20.3	19
SDSS J124058.03–015919.2	Y	37.4	19.7	20
SDSS J012940.05+384210.4	Y	37.6	19.8	14, 21, 22
SDSS J172102.48+273301.2	Y	38.1	20.1	23, 24
SDSS J152509.57+360054.5	N	44.3	19.8	23, 22
SDSS J080449.49+161624.8	. . . [b]	44.5	18.2	25
SDSS J141118.31+481257.6	N	46.0	19.4	14
GP Com	N	46.5	15.9	26
CSS121123:045020–093113	Y	47.3	20.5	27
SDSS J090221.35+381941.9	N	48.3	20.2	23
SDSS J120841.96+355025.2	N	52.6	18.8	28, 22
SDSS J164228.06+193410.0	N	54.2	20.3	23, 22
SDSS J155252.48+320150.9	N	56.3	20.2	29
V396 Hya	N	65.1	17.3	30

Table 6.1 (cont'd)

System[a]	Outbursting	Period (min)	Quiescence (g')	References
SDSS J173047.59+554518.5	N	$\cdots$	20.1	31
SDSS J104325.08+563258.1	Y	$\cdots$	20.3	31
PTF1 J221910.09+313523.1	Y	$\cdots$	20.6	17
PTF1 J085724.27+072946.7	Y	$\cdots$	21.8	17
PTF1 J163239.39+351107.3	Y	$\cdots$	23.0	17
PTF1 J152310.71+184558.2	Y	$\cdots$	23.5	17
SDSS J204739.40+000840.1	Y	$\cdots$	24.0	28

Note. — Systems are sorted by orbital period. System with no orbital period in the literature are at the bottom and sorted by quiescence magnitude.

[a]Names given here are either the IAU variable star name or the full name given in the discovery paper. Throughout this paper, we use a shortened version of the latter.

[b]SDSSJ0804+1616 has non-outburst variability. See Section 6.3.3.

References. — (1) Roelofs et al. (2010); (2) Steeghs et al. (2006); (3) Espaillat et al. (2005); (4) Fontaine et al. (2011b); (5) Roelofs et al. (2006b); (6) Roelofs et al. (2007b); (7) Chapter 5; (8) Patterson et al. (1997); (9) Kato et al. (2000); (10) Ramsay et al. (2010); (11) Patterson et al. (2000); (12) Kato et al. (2004); (13) Levitan et al. (2011); (14) Anderson et al. (2005); (15) Copperwheat et al. (2011); (16) Groot et al. (2001); (17) Levitan et al. (2013); (18) Roelofs et al. (2006a); (19) Woudt et al. (2005); (20) Roelofs et al. (2005); (21) Shears et al. (2011); (22) Kupfer et al. (in press); (23) Rau et al. (2010); (24) T. Augusteijn (2012, priv. comm.); (25) Roelofs et al. (2009); (26) Nather et al. (1981); (27) Woudt et al. (2013); (28) Anderson et al. (2008); (29) Roelofs et al. (2007c); (30) Ruiz et al. (2001); (31) Carter et al. (2013a)

Table 6.2: Observations of AM CVn systems by synoptic surveys

System[a]	PTF[b]	CSS[b]	MLS/SSS[b,c]	LINEAR[b]
HM Cnc	58/59	$\cdots$	$\cdots$	$\cdots$
V407 Vul	$\cdots$	$\cdots$	$\cdots$	$\cdots$
ES Ceti	$\cdots$	164/235	$\cdots$	$\cdots$
KIC 004547333	117/118	31/36	$\cdots$	$\cdots$
AM CVn	103/104	$\cdots$	$\cdots$	293/293
HP Lib	$\cdots$	131/134	S: 130/130	$\cdots$
PTF1 J191905.19+481506.2	22/110	$\cdots$	$\cdots$	$\cdots$
CR Boo	31/31	286/286	$\cdots$	266/271
KL Dra	$\cdots$	$\cdots$	$\cdots$	$\cdots$
V803 Cen	$\cdots$	$\cdots$	S: 231/231	$\cdots$
PTF1 J071912.13+485834.0	250/262	281/292	$\cdots$	$\cdots$
SDSS J092638.71+362402.4	8/8	254/295	$\cdots$	77/714
CP Eri	198/300	160/228	S: 35/45	$\cdots$
PTF1 J094329.59+102957.6	71/217	50/296	M: 51/53	16/1163
V406 Hya	$\cdots$	83/262	$\cdots$	$\cdots$
PTF1 J043517.73+002940.7	2/213	7/319	$\cdots$	$\cdots$
2QZ J142701.6–012310	$\cdots$	62/298	$\cdots$	19/493
SDSS J124058.03–015919.2	$\cdots$	224/302	M: 86/86	39/529
SDSS J012940.05+384210.4	$\cdots$	74/260	$\cdots$	$\cdots$
SDSS J172102.48+273301.2	208/298	31/382	$\cdots$	0/409
SDSS J152509.57+360054.5	80/100	181/254	$\cdots$	60/231
SDSS J080449.49+161624.8	110/112	336/358	$\cdots$	$\cdots$
SDSS J141118.31+481257.6	102/111	84/121	$\cdots$	0/237
GP Com	11/12	315/315	$\cdots$	207/450
CSS121123:045020–093113	31/66	21/240	$\cdots$	$\cdots$
SDSS J090221.35+381941.9	$\cdots$	47/341	$\cdots$	0/337
SDSS J120841.96+355025.2	97/101	283/288	$\cdots$	101/290
SDSS J164228.06+193410.0	$\cdots$	1/369	$\cdots$	0/430
SDSS J155252.48+320150.9	125/242	47/297	$\cdots$	0/230
V396 Hya	54/56	46/48	S: 235/236	$\cdots$

Table 6.2 (cont'd)

System[a]	PTF[b]	CSS[b]	MLS/SSS[b,c]	LINEAR[b]
SDSS J173047.59+554518.5	$\cdots$	69/119	$\cdots$	0/535
SDSS J104325.08+563258.1	14/16	22/120	$\cdots$	34/216
PTF1 J221910.09+313523.1	49/72	53/111	$\cdots$	$\cdots$
PTF1 J085724.27+072946.7	15/126	50/349	$\cdots$	0/791
PTF1 J163239.39+351107.3	61/173	36/324	$\cdots$	0/564
PTF1 J152310.71+184558.2	10/28	2/325	$\cdots$	0/203
SDSS J204739.40+000840.1	$\cdots$	0/67	$\cdots$	0/591

Note. — Systems are sorted by orbital period. System with no orbital period in the literature are at the bottom and sorted by quiescence magnitude.

[a]Names given here are either the IAU variable star name or the full name given in the discovery paper. Throughout this paper, we use a shortened version of the latter.

[b]Survey columns are of the form '# of detections / # of observations'.

[c]Since no system has observations from both MLS and SSS, we combine these surveys into one column and indicate the appropriate survey.

6.3 AM CVn Systems and Observational Data

We present the known AM CVn systems in Table 7.2, along with with some basic system properties and information on the presence of outbursts. Table 6.2 contains information on the survey data presented here. In this paper, we present only light curves showing significant variability. Combined light curves for all systems, including those which show no variability, are available from the PTF website[4]. Here, we differentiate between three behavioral classes: those systems showing repeated outbursts, those with a single observed outburst, and those with irregular photometric behavior.

6.3.1 Regularly Outbursting Systems

In Figures 6.1, 6.2, 6.3, and 6.4 we present outburst light curves of 11 systems with multiple observed outbursts. Two systems known to outburst frequently, PTF1J1919+4815 and KL Dra, are not presented here due to lack of data in the currently discussed surveys, but we refer the reader to Chapter 5 and Ramsay et al. (2010) for detailed analysis of their light curves. We used the outburst criteria detailed in Section 6.2.2.1 to identify outbursts

---

[4]http://ptf.caltech.edu/

in a quantitative fashion, and provide summary data of the outburst characteristics in Table 6.3.1.6. We provide more in-depth discussion on selected systems below. All outburst times are relative to the start of the light curve, which is indicated in the respective figure.

6.3.1.1 CR Boo

CR Boo was found to have a 46.3 d outburst recurrence time by Kato et al. (2000), hereafter K00. However, Kato et al. (2001), hereafter K01, reported that this was not constant and that CR Boo had switched to a 14.7 d recurrence time in 2001. More recent work by Honeycutt et al. (2013), hereafter H13, presents twenty years of CR Boo photometry and also shows significant changes in its photometric behavior. The more than nine years of regular monitoring presented here provides a complementary view of CR Boo's behavior, particularly in the time period since 2004 when H13's sampling is much more irregular.

The most surprising feature of the long-term light curve presented is a clear distinction in behavior between the first $\sim$4.5 yrs and the remaining data (Figure 6.1). We will refer to these separate parts of the light curve as the "active" and "inactive" states. In the active state ($2452647 < HJD < 2454337$), CR Boo was only observed between $14 < V < 16$. In contrast, during the inactive state ($2454337 < HJD < 2456147$), CR Boo was observed near its quiescent state ($V < 16$) $\sim$50% of the time. The abrupt change in behavior is present in both the LINEAR and CSS data.

Although an obvious step is to search for periodicity in the data, the infrequent and uneven sampling of the CSS and LINEAR surveys prevents a comprehensive analysis. Without compelling evidence, even a peak with significant power in a periodogram may be false. Instead, we consider the recurrence time during CR Boo's inactive state by using a set of observations from the P60 that were taken over $\sim$160 d and with a nominal cadence of 3 d. This provides a much better data set for period analysis. The peak of the periodogram for the P60 observations is at 46.5 d. This estimate is consistent with the outburst recurrence time found by K00. We present these observations, a periodogram generated from them, and a folded light curve in Figure 6.5.

We estimate an error of 10.5 d for this period by a bootstrap process (Efron 1982). To calculate the error, we drew, at random, 68 observations from the total set of 68 observations, allowing for repetition. This randomizes both the number of observations and which observations are used. We then calculated a Lomb-Scargle periodogram (Scargle 1982) for
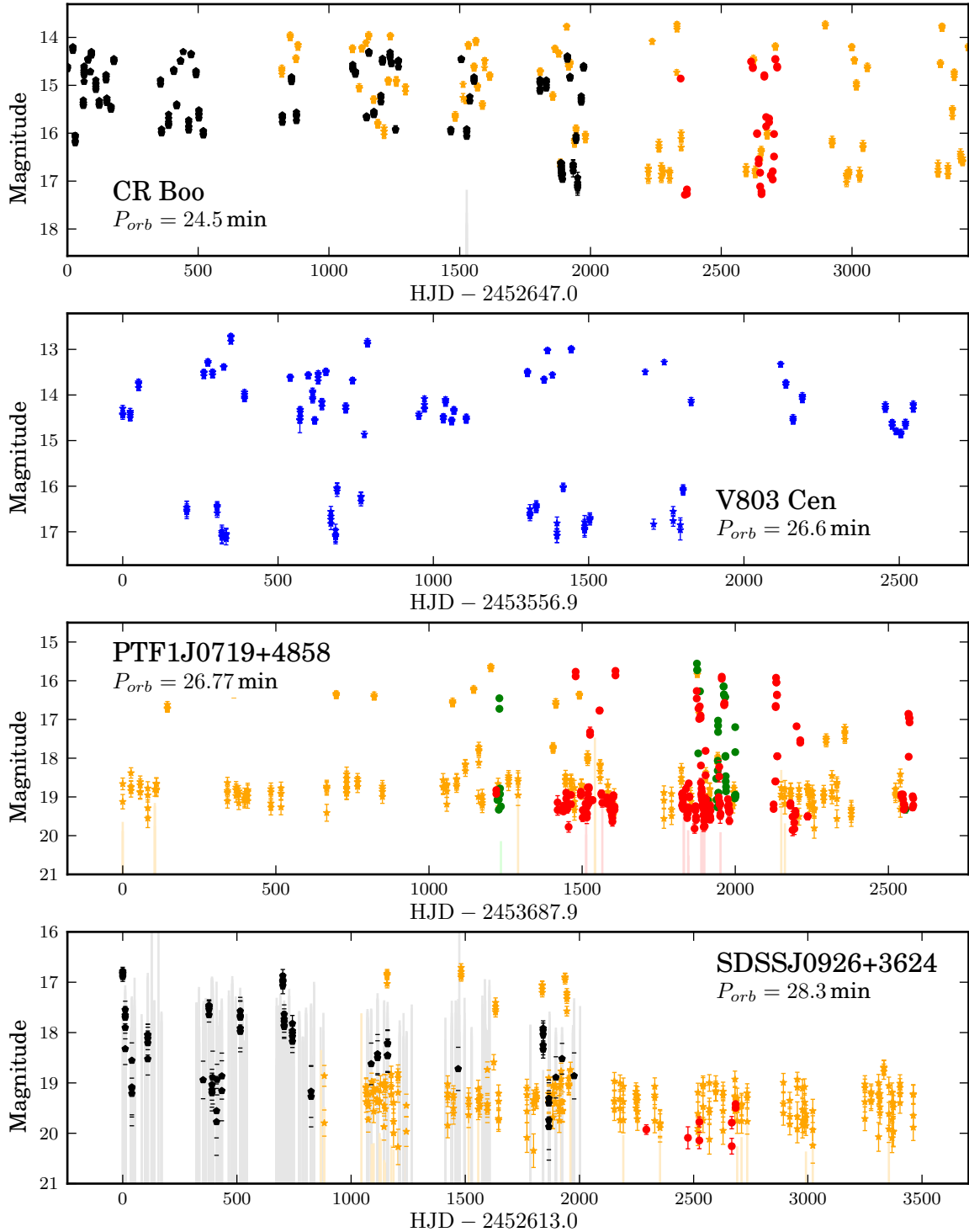
Figure 6.1 Light curves of the four shortest-period regularly outbursting AM CVn systems presented here. All show regular changes from quiescence to outburst (Section 6.3.1). In particular, we point out the significant change in the behavior of CR Boo and of SDSSJ0926+3624. The former switches from an "active" state to an "inactive" state (Section 6.3.1.1), while we have no explanation for the latter.
Legend: black = LINEAR; yellow = CSS; blue = SSS; red = PTF R; green = PTF g'. The tops of the vertical lines (color-coded to match the survey) are limiting magnitudes for non-detections.
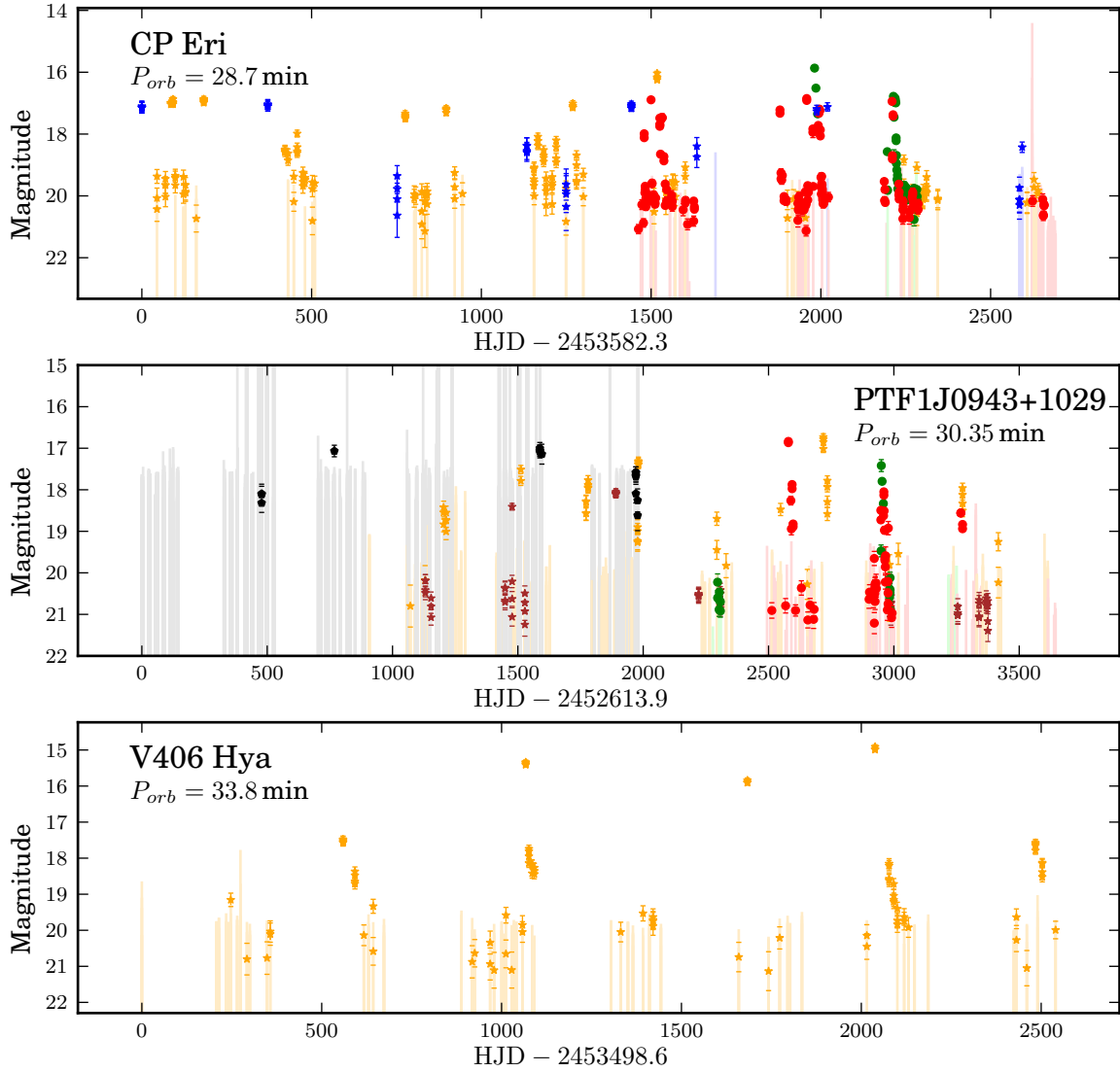
Figure 6.2 Light curves of three regularly outbursting AM CVn systems in order of P_{orb}, which all show regular changes from quiescence to outburst (Section 6.3.1). In contrast with the light curves in Figure 6.1, all systems in this figure spend the majority of their time in quiescence with only occasional outbursts. This is particularly true for V406 Hya.
Legend: black = LINEAR; yellow = CSS; blue = SSS; maroon = MLS; red = PTF R; green = PTF g'. The tops of the vertical lines (color-coded to match the survey) are limiting magnitudes for non-detections.
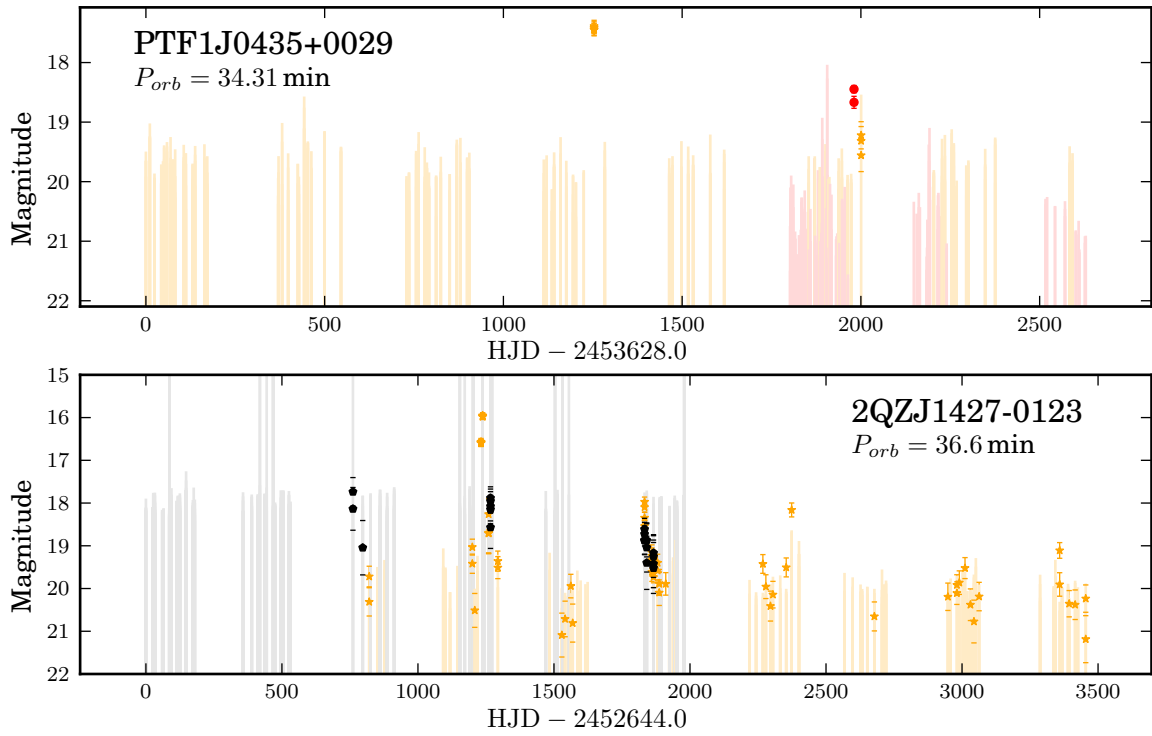
Figure 6.3 Light curves of the two longest-period, known, regularly outbursting AM CVn systems. Both systems show only a few outbursts with recurrence times of $\geq 1\,\mathrm{yr}$
Legend: black = LINEAR; yellow = CSS; red = PTF R. The tops of the vertical lines (color-coded to match the survey) are limiting magnitudes for non-detections.
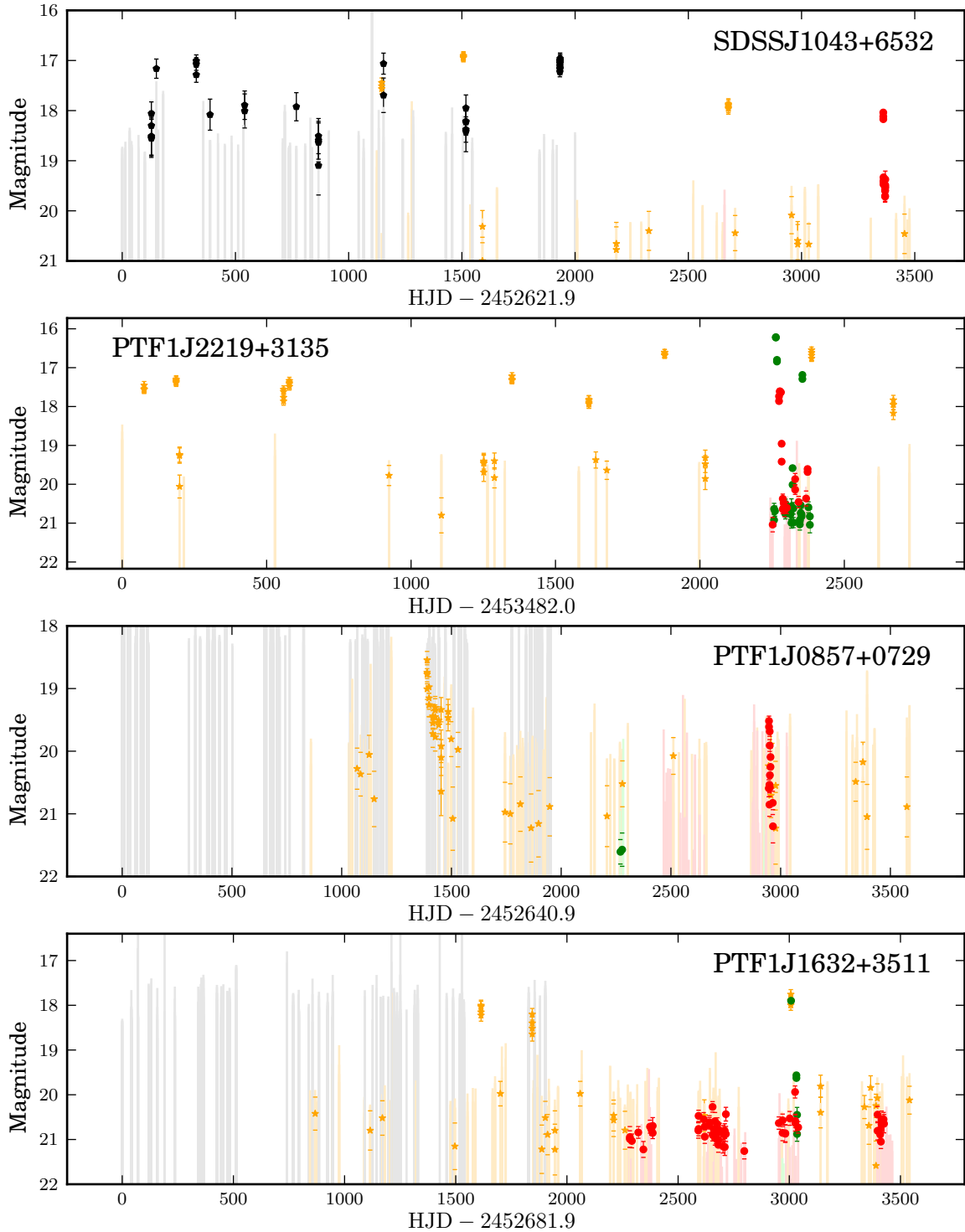
Figure 6.4 Light curves of the four regularly outbursting AM CVn systems with unknown orbital periods. We use their outburst recurrence times to estimate orbital periods in Section 6.4.2.1.

Legend: black = LINEAR; yellow = CSS; red = PTF R; green = PTF g'. The tops of the vertical lines (color-coded to match the survey) are limiting magnitudes for non-detections.
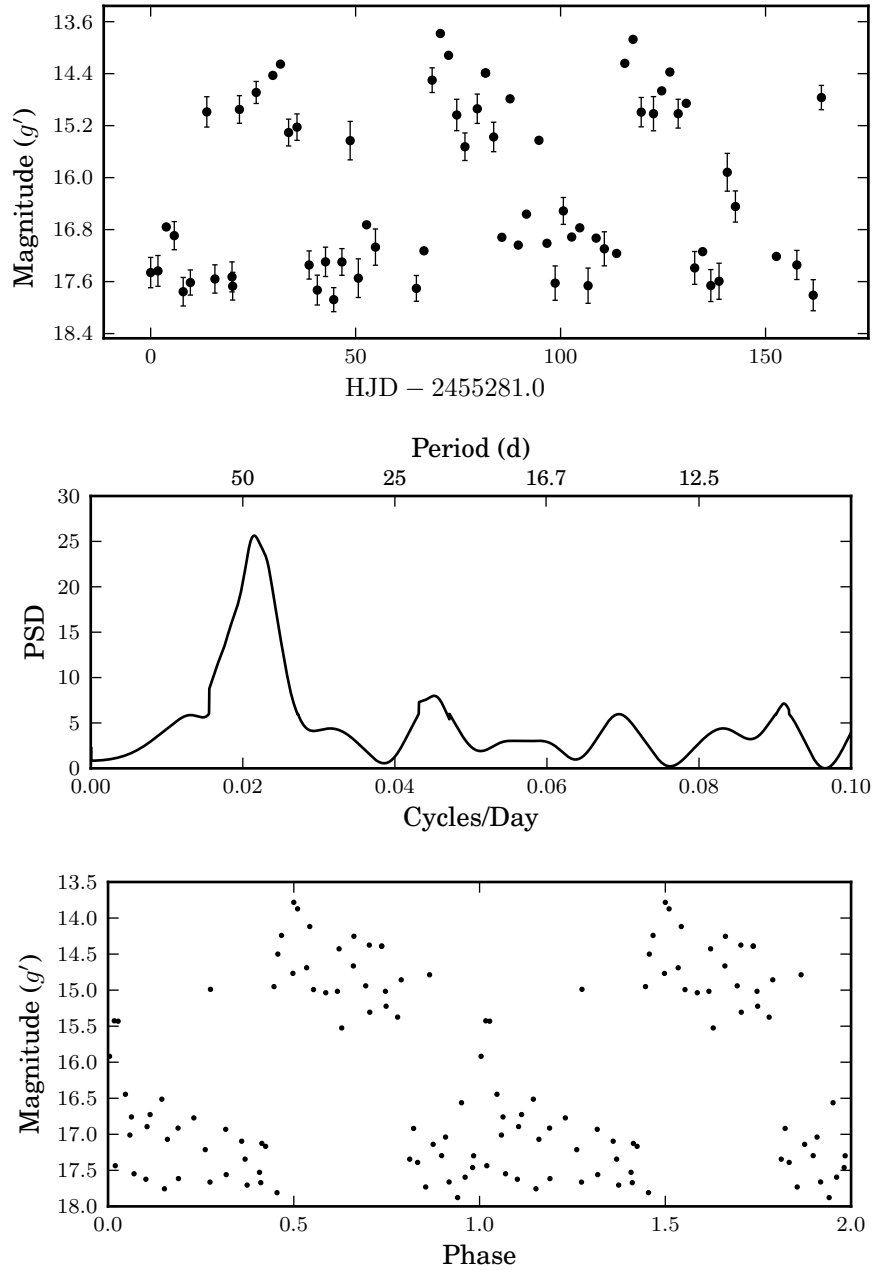
Figure 6.5 **Top:** The un-folded light curve of CR Boo taken by the P60. Three outbursts are clearly visible. We use this much higher-cadence and more regular light curve to establish that a period of ∼50 d is real.
Middle: A periodogram of the CR Boo P60 data, showing a peak at 46.5 d.
Bottom: The CR Boo P60 data light curve folded at the peak period of 46.5 d, with the peak of the outburst set to a phase of 0.5. The outburst and quiescent portions of the light curve are clearly separated.

the randomly drawn data, and recorded the peak. We repeated this process 500 times, and used the standard deviation as the error estimate.

We now use the much more extensive data for CR Boo from the LINEAR and the CSS surveys, and again compute a periodogram. Here we have a peak at $47.6\,\mathrm{d} \pm 4.8\,\mathrm{d}$. We present a periodogram and folded light curve in Figure 6.6.

The outburst recurrence time is statistically consistent between the P60 observations, the LINEAR and CSS observations, and the earlier work by K00 and H13. In particular, H13 found a dominant spacing between outbursts of $46\,\mathrm{d}$ over $20\,\mathrm{yrs}$. It is thus likely that the dominant outburst recurrence time is the same between active and inactive states and is around $46\,\mathrm{d}$. For the analysis in this paper, we use the value we derived from the LINEAR and CRTS data, as it is derived from $5\,\mathrm{yrs}$ of data.

Our data are in agreement with those of H13, specifically regarding the changing state of CR Boo. However, H13 shows even more variability in the long-term light curve, particularly during the time period that is not covered by the data presented here (1990–2000). We believe that CR Boo's inactive state between 2005 and 2010 has been remarkably stable, particularly given the relatively clean outburst light curves presented here. It is obvious that the system often experiences rapid changes in its behavior.

6.3.1.2 V803 Cen

V803 Cen was found by Kato et al. (2004) to have a $77\,\mathrm{d}$ outburst recurrence time with very similar characteristics to the active state of CR Boo described earlier. The light curve presented here (Figure 6.1) shows no significant changes in photometric behavior over almost $7\,\mathrm{yrs}$. We see no coherent light curve when folded at the recurrence time given by Kato et al. (2004). No significant period in a periodogram calculated from the SSS data results in a coherent light curve either, which is consistent with the data of CR Boo in its active state. We thus use the period found by Kato et al. (2004) for our analysis in this paper and assume a 10% error, consistent with the variability in the outburst recurrence times of CR Boo, KL Dra, and PTF1J0719+4858 (see Table 7.2 for references). It is possible that this lack of periodicity is due to changing outburst recurrence times, as seen for CR Boo during its active state (Section 6.3.1.1).
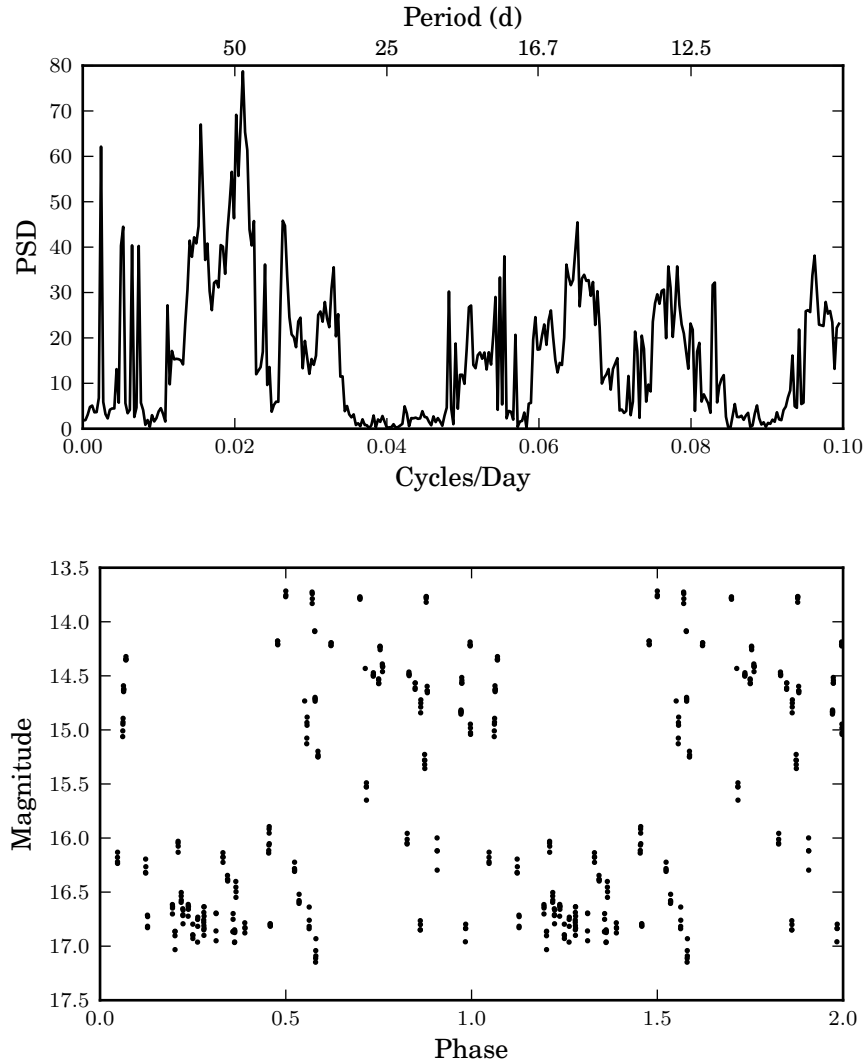
Figure 6.6 **Top:** A periodogram of the CSS and LINEAR data of CR Boo. The strongest peak is at 47.6 d, with an associated error of 4.8 d. Only with the proof from the P60 data in Figure 6.5 do we believe that this is a real period.
Bottom: A folded light curve of the CSS and LINEAR data of CR Boo's while it is in its inactive state. The data is folded at the above period of 47.6 d, and shows a clear outburst and quiescent states. The recurrence time is consistent over 5 yrs.

6.3.1.3   SDSSJ0926+3624

SDSSJ0926+3624 is perhaps the best understood AM CVn system, given its deep eclipses. Copperwheat et al. (2011) reported on two outbursts and showed the CSS light curve. The light curve we present here has both additional historical data from the LINEAR survey, as well as newer data from the CSS. Similarly to CR Boo, SDSSJ0926+3624 shows a dramatic change in behavior roughly half way through the light curve (Figure 6.1).

The earlier part of the light curve ($HJD \lesssim 2461620$) shows repeated outbursts, with a recurrence time of 140–180 d. We note that given the non-continuous coverage, gaps are variable in length, and given the cluster of adjacent outbursts while SDSSJ0926+3624 was in this state, we divided those gaps by an integer on the assumption of missed light curves.

The latter part of the light curve ($HJD \gtrsim 2461620$), however, does not show any outbursts. Given that the cadence of CSS did not change, this is surprising, and is likely an indicator of a real change in the system. We do know that at least one outburst was missed in the CSS coverage — that reported in Copperwheat et al. (2011) to have occurred in March 2009. Although it is possible others were missed as well, had the previous behavior continued we would have expected at least some to be observed by the CSS.

6.3.1.4   CP Eri

Previous studies of AM CVn systems have identified only a few outbursting systems that show both super outbursts and normal outbursts. These systems (PTF1J1919+4815, CR Boo, and PTF1J0719+4858) have some of the shortest known orbital periods of the out-bursting systems. The normal outbursts are typically 1–2 days in length and appear to have a similar or slightly lower strength as super-outbursts (e.g., K00, L11). The data presented here show that CP Eri (Figure 6.2), a slightly longer-period system with $P_{orb} = 28.7$ min, also appears to show normal outbursts. Three outburst events of at least two magnitudes between super-outbursts are constrained to last fewer than five days — consistent with what would be expected for a normal outburst. This likely indicates that other longer-period AM CVn systems also show normal outbursts.

6.3.1.5   PTF1J0435+0029

In 7 yrs of coverage with the CSS and the PTF, PTF1J0435+0029 was observed in outburst twice (Figure 6.3) . Given the faint nature of the system, only an observation at the very beginning of the outburst would be above the limiting magnitude of both surveys, and thus the lack of additional outbursts is not surprising. The two observed outbursts were $\sim$730 d apart ($t = 1250 \pm 30$ d and 1980^{+50}_{-8} d), but the time half way between had no observations, and hence both 365 d and 730 d recurrence times are consistent with the data. Here, we use the former, as the latter would be a significant outlier from the remainder of the AM CVn systems (see Table 6.3.1.6). Only further observations can remove this ambiguity.

6.3.1.6   2QZ J1427–01

We find three outbursts for 2QZ J1427–01 (Figure 6.3), with peak magnitudes at $t = 760^{+40}_{-50}$ d, 1240^{+30}_{-20} d, and 1830^{+10}_{-30} d. We constrain the duration of the outbursts to $<$50 d, based on the second outburst. We provide lower estimates for the remaining two outbursts using this outburst duration to obtain a lower bound on their times of peak luminosity, since both outbursts occurred before the start of an observing season. The mean difference between these peaks is 540$\pm$65 d, with the error derived based on the errors of each outburst peak. We note that this is roughly consistent with the 10–20% change in outburst recurrence time observed in shorter period systems.

These outbursts occur over a period of $\sim$1000 d, while we have data over a timespan of $>$3500 d. We thus expect additional outbursts at $t \approx$ 210 d, 2370 d, 2910 d, and 3450 d. The first falls between observing seasons, while the third and fourth are just before and after an observing season, respectively. Given the associated error, it is highly likely that no outburst would have been seen. There are observations at $t =$ 2354 d, 2374 d, and 2401 d, roughly coincident with when we would expect an outburst. One of the exposures on $t = 2374$ d does show a detection consistent with an outburst, while the remaining three exposures do not indicate outbursts. This may indicate that the system was at the end of an outburst. We note that the data obtained by R12 does not provide coverage of these predicted outburst times.

We also consider whether the outburst recurrence time may be shorter. A recurrence

Table 6.3. Outburst properties of recurring outburst systems.

System	Orb. Per. (min)	# Observed Outbursts	Observation Span (d)	Recurrence Time (d)	Duration (d)	Strength (mag)
PTF1J1919+4815[a]	22.5	$\cdots$	$\cdots$	36.8 ± 0.4	$\sim$13	3
CR Boo[b]	24.5	$\cdots$ [c]	3445	47.6 ± 4.8	$\sim$24	3.3
KL Dra[a]	25.0	$\cdots$	$\cdots$	44–65	$\sim$15	4.2
V803 Cen[a]	26.6	$\cdots$ [c]	2545	77	$\cdots$	4.6
PTF1J0719+4858[a]	26.8	23	2581	65–80	$\sim$18	3.5
SDSSJ0926+3624	28.3	9	3462	160 ± 20	$\sim$20	2.4
CP Eri	28.7	13	2691	108 ± 13	$\sim$20	4.2
PTF1J0943+1029	30.4	10	3645	110 ± 14	<30	4.1
V406 Hya	33.8	5	2540	280 ± 50	<100	5.9
PTF1J0435+0029	34.3	2	2629	365 ± 60	<60	5.1
2QZJ1427–0123	36.6	3	3455	540 ± 65	<50	4.3

Note. — A description of how the features calculated here is in Section 6.2.2.1. In particular, the probability of a missed outburst assumes that the recurrence time and duration provided here are correct.

[a]Properties presented here (except observation details) are from the literature. See Table 7.2 for references.

[b]The reported data are from the inactive state of CR Boo.

[c]We do not count the number of outbursts due to the complicated and rapidly changing nature of the light curve.

time of one-half the proposed value would require outbursts at $t = 1560\,$d and $2640\,$d, both of which are in the middle of observing seasons. Likewise, one-third of the proposed value also shows coverage during times of expected outbursts. We thus conclude that 2QZ J1427–01 has an outburst recurrence time of $540 \pm 65\,$d.

6.3.2 "Single Outburst" Systems

Seven of the known AM CVn systems have only had a single outburst recorded. We present the light curves of these systems in Figures 6.7 and 6.8. Drawing on our observations, as well as those reported in the literature, we list outburst times and strengths, as well as the probability of a missed outburst, in Table 6.3.2. We present the outburst light curves for four of the systems with the most details in Figure 6.9.

We focus on the data here, and leave out discussion of these systems and whether they are truly one-time outbursts until our discussion in Section 6.4.2.2. The most important
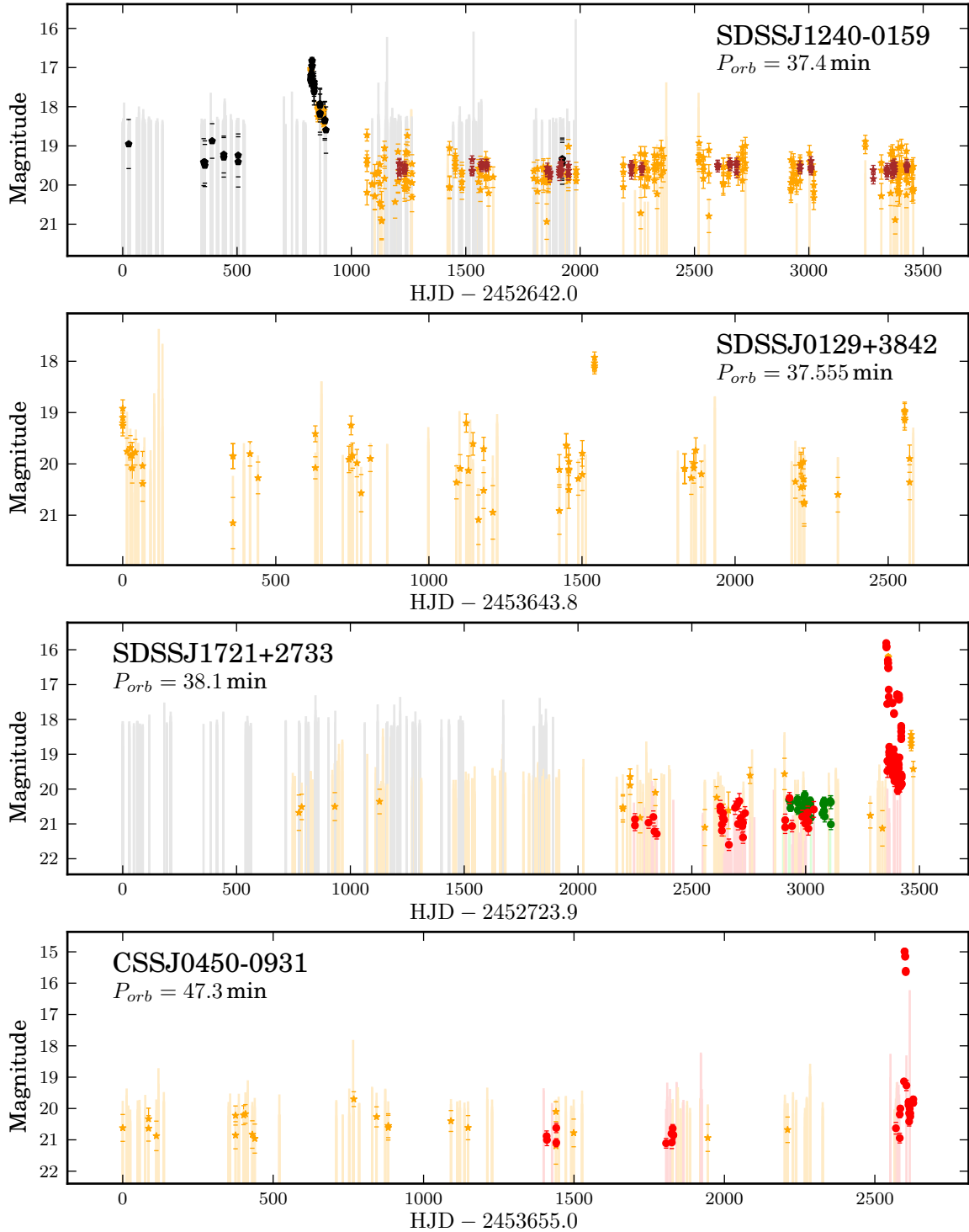
Figure 6.7 Light curves of the four outbursting AM CVn systems with only one recorded outburst. All systems have longer orbital periods than the regularly outbursting AM CVn systems. In the case of SDSSJ0129+3842, two additional possible outbursts are visible, but they do not meet our criteria for an outburst (Section 6.2.2.1).

Legend: black = LINEAR; yellow = CSS; maroon = MLS; red = PTF R; green = PTF g'. The tops of the vertical lines (color-coded to match the survey) are limiting magnitudes for non-detections.
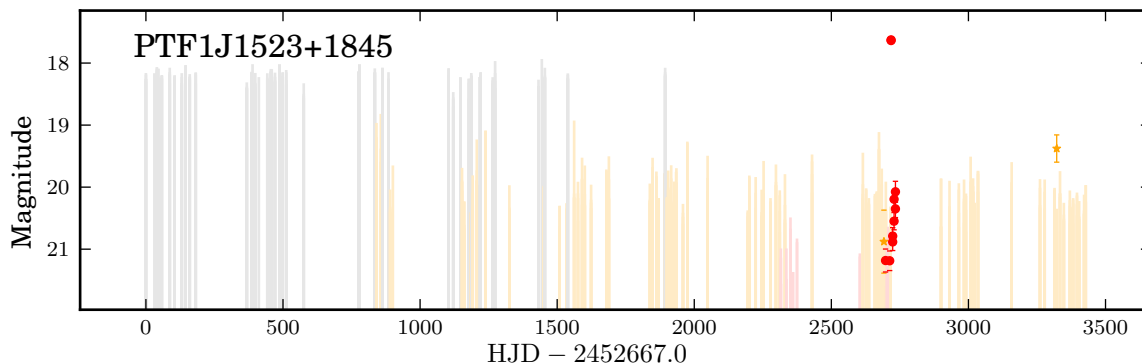
Figure 6.8 Light curve of PTF1J1523+1845, a single outburst AM CVn system with no known orbital period.
Legend: black = LINEAR; yellow = CSS; red = PTF R. The tops of the vertical lines (color-coded to match the survey) are limiting magnitudes for non-detections.

Table 6.4.   Details of single outbursts.

System	Outburst Date	Strength[a] (mag)	Probability of Non-Detection
SDSSJ0129+3842	2009 Nov 29	~5.4	0.78 ± 0.02
CSS0450–0931	2012 Nov 22	~5	0.75 ± 0.02
SDSSJ1240–0159	2005 Mar 15	~6	0.18 ± 0.01
PTF1J1523+1845	2010 Jul 07	~5.8	0.78 ± 0.02
SDSSJ1721+2733	2012 May 30	~5	0.59 ± 0.02
SDSSJ2047+0008	2006 Oct 12	~5	1.0

Note. — The data presented in this table is drawn from a combination of the referenced papers and the light curves presented here. Systems are arbitrarily ordered in terms of RA.

[a]The numbers presented here are lower bounds since the outburst peak was not always caught.

question to answer is to calculate the probability of a missed outburst. We use a bootstrap approach (Efron 1982) where, for each of 1,000 iterations for each system, we tested whether an outburst starting at a random time between the start and end points of the light curve would be detected. A system in outburst was assumed to be detected if it was 1.5 mag above quiescence and greater than the limiting magnitude for that exposure. We required at least two detections over the course of the outburst. This itself was repeated 100 times, and the standard deviation of these 100 runs is the reported errors for the probability of non-detection. The detection threshold was set in agreement with our definition of an outburst in Section 6.2.2.1 and the scatter of points in quiescence for all these systems was ∼0.5 mag.

For this to work effectively, we must use a reasonable model of the light curve. We note that for all but SDSSJ1240–0159, the post-peak outburst light curve consists of a sharp decline that reaches 1–2 mag above quiescence within 10 d, and then a gradual decline over 30-60 d. We base this not only on our data (Figure 6.9) but on similar light curves for SDSSJ0129+3842 in Figure 4 of Ramsay et al. (2012) and SDSJ2047+0008 in Figure 4 of Anderson et al. (2008). We model all three systems by using an inverse parabola that reaches 1.5 mag above quiescence after 10 d, and then a linear decline over the next 50 d back to quiescence. The only difference in our model between the systems is the initial outburst peak magnitude. In the case of SDSSJ1240–0159, we assume a simple linear decline from peak to quiescence over 80 days. This difference accounts for the significantly different shape of the outburst (Figure 6.9). The results of these calculations are listed in Table 6.3.2.

We make three observations here based on these results. First, it is not surprising that SDSSJ2047+0008 was not detected in our data, given its short outburst duration and quiescent magnitude of $g' \sim 24$ (Anderson et al. 2008). Second, out of the rest of the systems, only SDSSJ1240–0159 is likely to have not had a missed outburst. Its outburst shape, as noted earlier, is very different than the other systems. Finally, SDSSJ1721+2733 shows re-brightening events during its decline (see Figure 6.9), something also reported for SDSSJ0129+3842 (Shears et al. 2011).

6.3.3 Other Variability

Ramsay et al. (2012) noticed that SDSSJ0804+1616 showed significant variability, but not of the typical outburst variety. Instead, it showed irregular variability with an amplitude
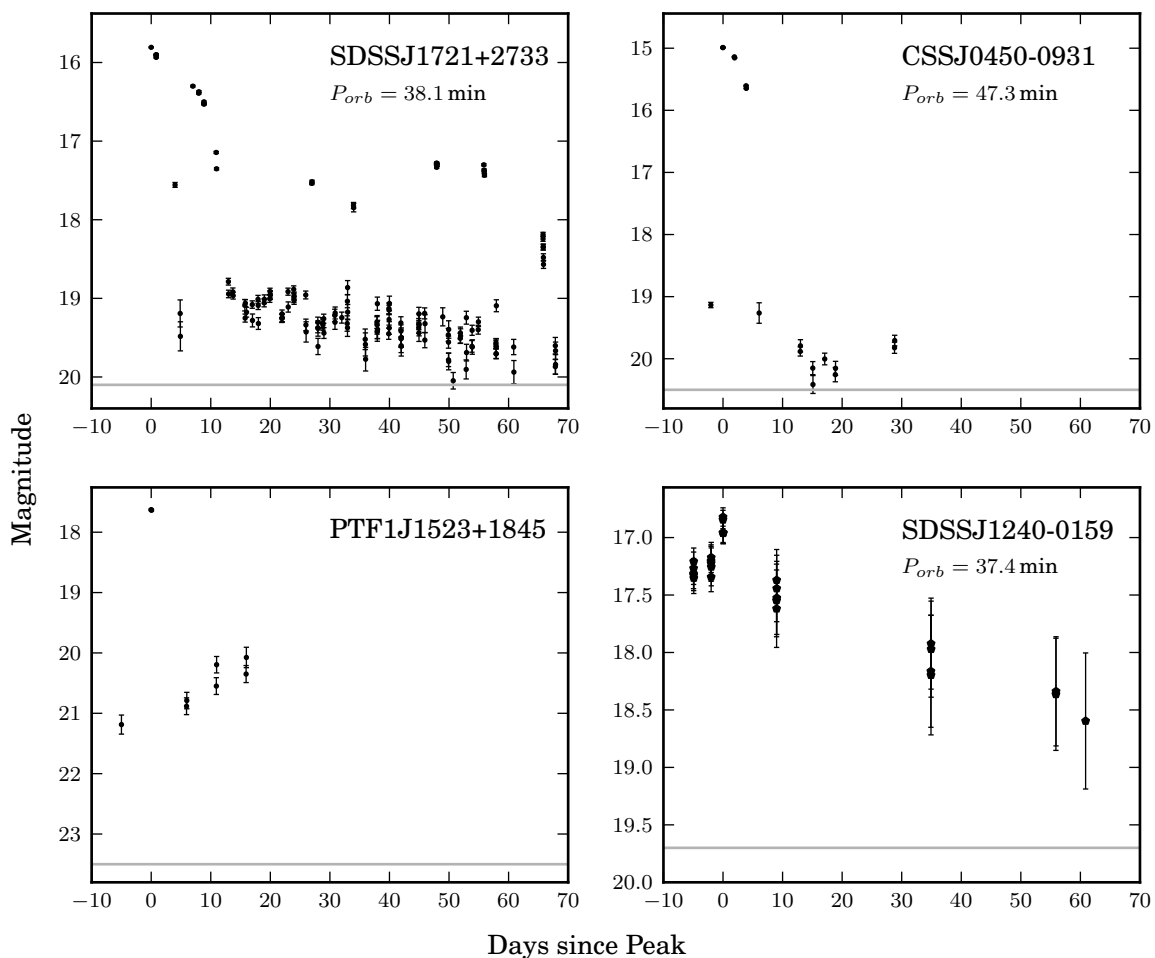
Figure 6.9 A plot of the outburst light curves for four of the single outburst systems. SDSSJ1240–0159 is from LINEAR data and the rest are PTF R-band data. The gray line indicates the quiescence level of each system. We note the similarity between the light curves of SDSSJ1721+2733 and CSSJ0450–0931, and, to a lesser extent, likely due to lack of data, PTF1J1523+1845. All three systems show a sharp rise, a fall within 10 days, and a gradual decline towards quiescence. On the other hand, the light curve of SDSSJ1240–0159 shows a gradual decline from peak and is still >1.5 mag brighter than quiescence 60 d from the peak of the outburst.
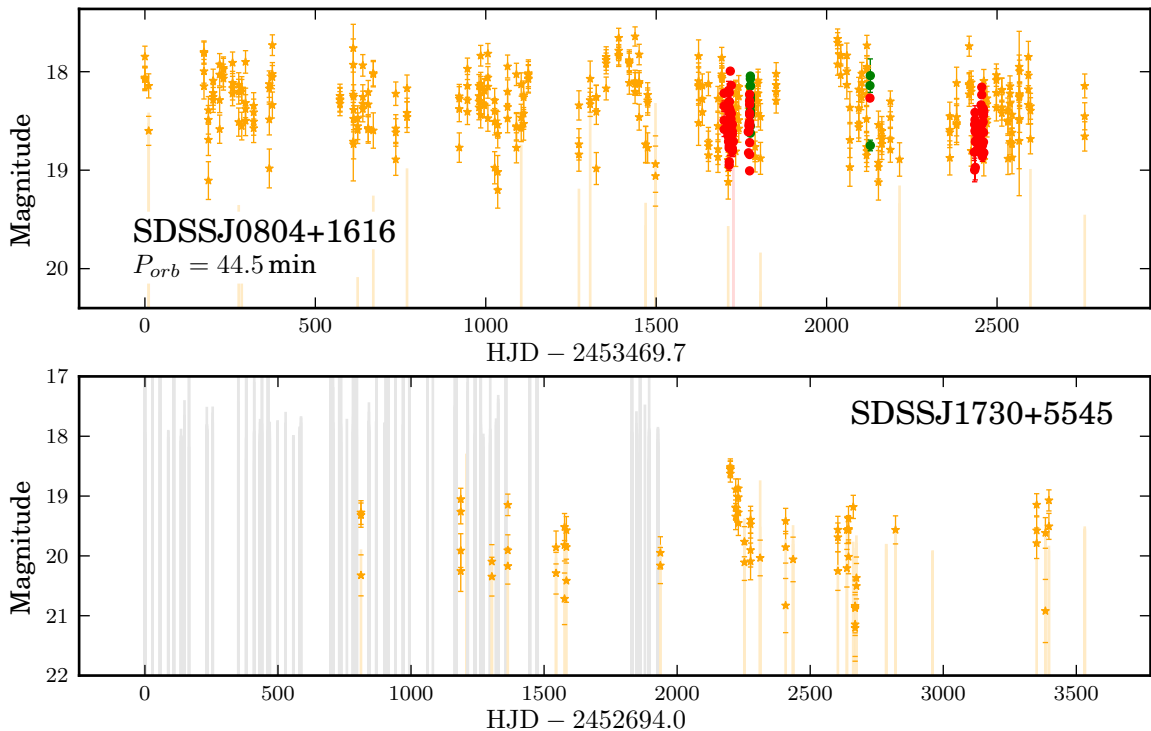
Figure 6.10 Light curves of two systems with non-outburst variability (Section 6.3.3). SDSSJ0804+1616 is possibly a magnetic system (Roelofs et al. 2009) and shows non-periodic variability akin to that seen in magnetic CVs. SDSSJ1730+5545 shows a potential outburst, but one which does not meet our criteria.
Legend: black = LINEAR; yellow = CSS; red = PTF R; green = PTF g'. The tops of the vertical lines (color-coded to match the survey) are limiting magnitudes for non-detections.

of $\sim$1 mag. The light curve we present in Figure 6.10 confirms this variability over 7 yrs. We find no discernible period, although the timescale of the variability could be as short as 1–2 nights, based on several nights where the target was observed $\sim$15 times in one night by the PTF. Roelofs et al. (2009) suggested that SDSSJ0804+1616 may be a magnetic system. Similar light curves have been observed in PTF for magnetic CVs (Margon et al. 2013), strengthening the argument that SDSSJ0804+1616 is, in fact, a magnetic system.

We also present the light curve of SDSSJ1730+5545 in Figure 6.10. The light curve contains what appears to be the tail end of an outburst. However, despite multiple detections at $\sim$1.5 mag brighter than the median magnitude, it fails to meet our criteria for the definition of an outburst. Similarly, SDSSJ0129+3842 also shows at least two other candidate outbursts, both of which fail to meet our criteria. We are reluctant to loosen the criteria, however, as SDSSJ1730+5545 is the only system where just a partial outburst may have been detected. Loosening the criteria would likely introduce spurious "outbursts" in

the other systems presented here.

6.4 Results and Discussion

6.4.1 AM CVn System Evolution

The composite light curves presented here allow us to see long-term changes in the photometric behavior of AM CVn systems. We summarize the phenomenology of outbursting AM CVn systems in the following three stages of evolution:

1. When the mass transfer rate from the secondary falls below a critical value (believed to occur around $P_{orb} = 20\,\mathrm{min}$), the accretion disk is no longer in a high state at all times and instabilities in the disk develop that lead to large amplitude photometric variations. The light curves of the shortest-period systems in this study (CR Boo and V803 Cen) show that the transition from a stable high state to "regular" outbursts is in fact an irregular one with variations on long timescales (years). The systems can spend most of their time in a high state with occasional excursions to the quiescent state (which we called the active state in our discussion of CR Boo; see Section 6.3.1.1), or, spend most of the time in a low state but with an extended period of time in a high state (the inactive state).

2. Only when reaching a period of $\sim$28 min does the system seem to settle into a more regular pattern of quiescence with well-defined outbursts. Between orbital periods of roughly 28 min and 37 min, AM CVn systems remain in their inactive state, and are in a gradual process of an exponential increase in their outburst properties (see Section 6.4.2 for details). Normal outbursts still occur, but are rarer and longer than in shorter-period systems. However, here too significant changes in behavior can occur, such as the sudden lack of outbursts from SDSSJ0926+3624.

3. At longer orbital periods, $\dot{M}$ has decreased significantly, and systems experience rare outbursts, if any. These systems may be the analogs to WZ Sge systems among the CVs, but the short outburst durations ($\sim$10–15 d) of all known systems except SDSSJ1240–0159 do not fit with this model. One possible explanation is that such short outbursts are the equivalent of the normal outbursts seen in much shorter-period systems (e.g., Section 6.3.1.4). The outburst of SDSSJ1240–0159, which shows

a significantly longer duration than the remaining systems, would then be a super-
outburst. Its outburst properties are, in fact, consistent with the relations we find in
Section 6.4.2. If this proposal is correct, then the recurrence time of these shorter-
duration outbursts could be on the order of years, while the recurrence time of super-
outbursts could be decades. Such a recurrence time would be consistent in WZ Sge
systems, but no normal outbursts have been observed in WZ Sge systems (Matthews
et al. 2007). However, the significantly different composition of the systems (He-rich
vs. H-rich) could account for this significant difference in behavior.

It is obvious that orbital period is not the only factor influencing the behavior of these
systems, and other factors, likely the component masses, donor composition, and donor
entropy will play a role. For example, V406 Hya has significantly stronger outbursts than
other systems of comparable orbital periods (see Table 6.3.1.6).

6.4.2   Outburst Behavior vs. Orbital Period

The change in outburst behavior with orbital period appears to be gradual, rather than
abrupt. While there is only data for a limited number of systems, these are enough to find
an approximate relation. For the outburst recurrence time and duration we chose to use an
exponential model, while for the strength, Δmag, we used a linear model in magnitudes (this
corresponds to an exponential model in flux). These choices are somewhat arbitrary and
are only a simple approximation to any physical relation. We tried to model the equations
using a power law, as might be expected based on the orbital evolution equations proposed
for AM CVn systems (Faulkner et al. 1972b), but found the exponential models to provide
significantly better fits. Using the values from Table 6.3.1.6, we find the following relations
using a least-squares fit,

$$P_{so} = 0.165(137)e^{0.219(24)P_{orb}} + 14.8(87)$$

$$\Delta\text{mag} = 0.13(6)P_{orb} - 0.16(168)$$

$$t_{dur} = 0.39(115)e^{0.122(82)P_{orb}} + 7.9(76),$$

where P_{orb} is the orbital period in minutes, P_{so} is the outburst recurrence time in days,
Δmag is the strength of the outburst, and t_{dur} is the duration of the outburst in days.
Parameter errors are provided from the fit. A plot of these quantities, together with the
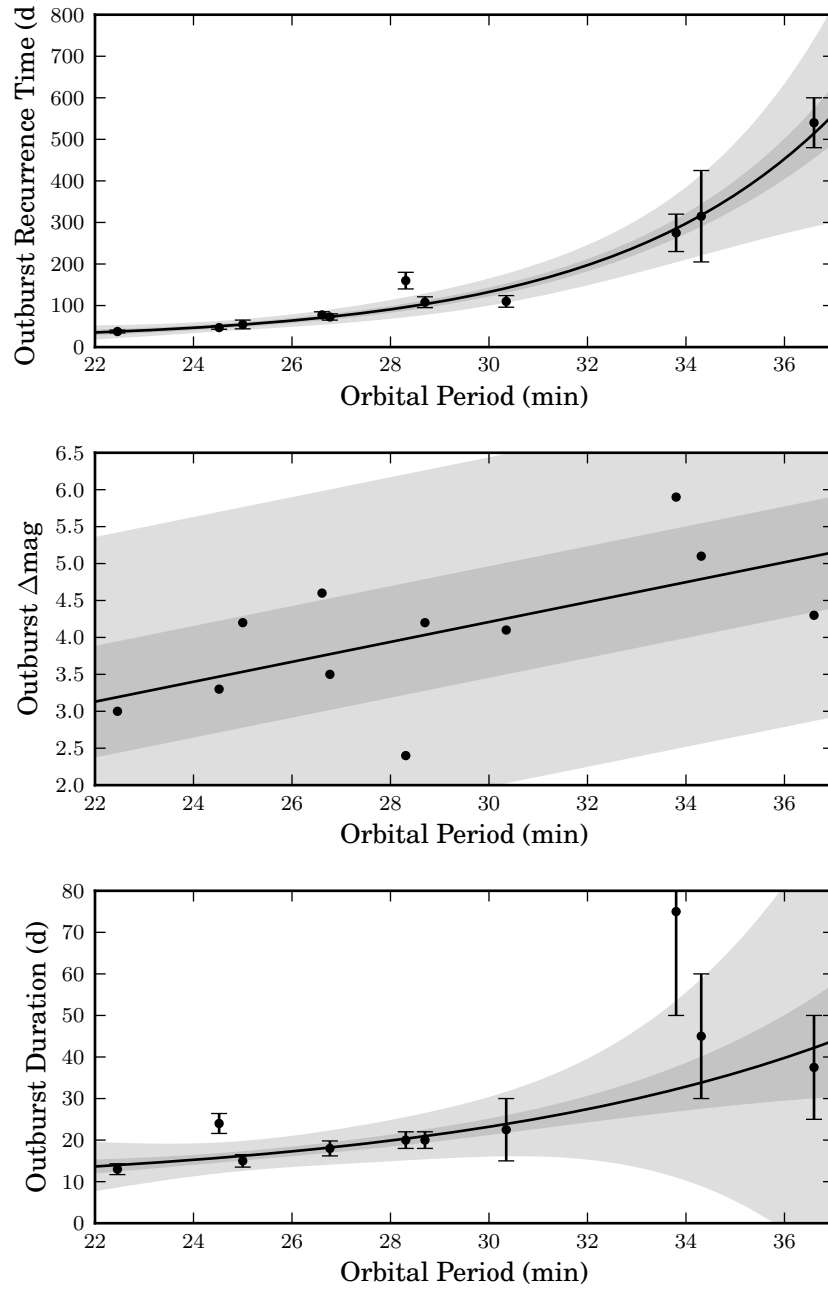
Figure 6.11 Plots of outburst properties vs. orbital period. Errors for recurrence times are given in Table 6.3.1.6. For outburst duration, we assumed a 10% error for all systems that do not have an upper limit in Table 6.3.1.6. For those with upper limits, we assumed that the duration was 75% of the upper limit, with a 25% error. These choices are somewhat arbitrary, but are reasonable given the light curves. The solid line is a best fit model. For the recurrence time and outburst duration we used an exponential model, while for the outburst magnitude we used a linear model (which corresponds to an exponential model in flux). The darker-shaded areas represent the 1σ errors while the lighter-shaded areas represent the 3σ errors. For the recurrence time and duration, we use the fit errors. For the outburst strength, we use the standard deviation of the residuals.

best fits, are shown in Figure 6.11. The outburst recurrence time is a much better fit than the duration or strength — this may be due to either measurement errors or because AM CVn systems vary more in outburst strength and duration than in recurrence time.

Verification of these relations will require significant additional period measurements. We note that these relations do not apply to systems with only one observed outburst, and we do not recommend applying them to systems with only a few observed outbursts. It is highly likely that, particularly at the long-period end, these relations are not accurate due to the lack of data in that period regime. In particular, the single outburst systems identified in this paper typically show an outburst duration of only 10–15 d (see Figure 6.9), whereas t_{dur} trends towards 50 d at a similar orbital period.

6.4.2.1   Prediction of Orbital Periods

The measurement of AM CVn system orbital periods is a difficult process, particularly for the faint systems discovered recently. The relation between orbital period and outburst recurrence time presented here allows us to estimate periods for systems not yet measured. Four systems show multiple outbursts and have unknown orbital periods:

- PTF1J2219+3135 has an outburst recurrence time of 64 ± 5 d from which we predict an orbital period of 26.0 ± 4.9 min.

- PTF1J1632+3315 has an outburst recurrence time of 230 ± 35 d and thus a predicted orbital period of 32.8 ± 5.3 min.

- SDSSJ1043+6532 has an outburst recurrence time of 99 ± 12 d and thus an predicted orbital period of 28.5 ± 5.0 min.

- PTF1J0857+0729 has only two observed outbursts, separated by $\sim$1550 d. It is likely to have a period $\geq$37 min.

We caution that these are estimates to serve primarily in observation planning. Errors are derived from a combination of fit parameter errors and outburst recurrence time errors. We can state that a preliminary analysis of phase-resolved spectroscopy of PTF1J2219+3135 from August 2012 does show an orbital period of $\sim$27 min, in agreement with the predicted period.

6.4.2.2 Single Outburst Systems

In Section 6.3, we separated the outbursting AM CVn systems into those that showed regular outbursts, and those for which only a single outburst has been observed. We also showed in Table 6.3.2 that it is highly likely that we missed an outburst for most of the systems. Only for one system did we find a probability of a missed outburst below 50%, while four out of six have missed-outburst probabilities of $\geq 75\%$.

Using the above relation, the recurrence time for a 38 min system is 2 yrs. We note that of the 7 systems with a single known outburst, only one was observed in outburst by LINEAR in 5.5 yrs of data and four were detected in 7 yrs CSS data. In contrast, in only 3.5 yrs of PTF data, three systems were detected in outburst, which shows that the deeper reach and faster cadence of PTF significantly improves the odds of detection. For these reasons, we believe that most of the "single" outburst systems follow the same principles as shorter-period orbital systems, but, given their short outburst duration (see Sections 6.3.2 and 6.4.1), long recurrence times, and faint quiescent magnitudes, are simply difficult to detect in outburst.

6.4.3 Implications for Discovery of AM CVn Systems

The relationships between orbital period and outburst properties developed in Section 6.4.2 allow us to calculate the detection probability, $\mathrm{p}(P_{orb}, m_{qui})$, of an outbursting AM CVn system by a synoptic survey with a known cadence and limiting magnitude. We can use these results to estimate the number of outbursting AM CVn systems with $20\,\mathrm{min} < P_{orb} < 37\,\mathrm{min}$ that a survey could discover. Such a calculation involves two elements. First, we must find the detection probability of an AM CVn system that has a specific orbital period and quiescent magnitude. Second, we need a model for the Galactic distribution of AM CVn systems. Here, we calculate the number of systems that could be discovered by two model surveys based on the CSS and the PTF.

6.4.3.1 Survey Definition and System Detection Probability

We begin by defining our surveys. We assume no weather interruptions, and normal-distributed limiting magnitudes with $\sigma = 0.5\,\mathrm{mag}$ around the median limiting magnitude of the survey. We do not account here for crowding and assume perfect detections (e.g.,

no artifacts). For the CSS-like survey, we assume four exposures per night over 30 min, taken every 2 weeks (Drake et al. 2009), and a median magnitude of $V = 19.5$. We assume that each field is observed for $\sim$200 d = 15 observations per year, for 7 years. For the PTF-like survey, we assume 2 exposures per night over 1 h, but with a cadence of 4 d and a limiting magnitude of $V = 20.5$. We assume that each field is observed for $\sim$3 months (20 observations) for 3 years. Lastly, we assume that both surveys cover Galactic latitudes of $15° < b < 90°$ at all Galactic longitudes.

We now construct an outburst light curve model. Although we constructed such a model for the calculation of non-detection probabilities in Section 6.3.2, that model was only applicable to systems with $P_{orb} > 37$ min. The light curve profile (see Section 6.3.1 of this paper and Figure 4 of Ramsay et al. 2012) of outbursting systems with $P_{orb} < 37$ min is substantially different. Thus, we model the outburst as a sudden rise to the outburst magnitude (Δmag$+m_{qui}$, as defined in Section 6.4.2), and a gradual decline over t_{dur} days to 0.5 mag above m_{qui}, with a return to quiescence thereafter.

To calculate the probability, $\mathrm{p}(P_{orb}, m_{qui})$, we use a bootstrap approach (Efron 1982). For every P_{orb} and m_{qui}, we calculate the light curve at the simulated exposure times using a random start time for the outburst sequence. We determine whether a particular light curve was detected based on the criteria in Section 6.2.2.1. Briefly, we required at least 2 consecutive detections (defined as being brighter than the limiting magnitude) within 15 d that were $\geq$0.5 mag above the quiescence magnitude. We note that we only use the 0.5 mag above quiescence criterion here, as opposed to the 3σ criterion. However, the error of observations at the 5σ limiting magnitude should be $\sim$0.2 mag, which is consistent with these criteria here. We caution that these criteria for outbursts, and the ones generally applied in this paper, are designed only to ignore fake outbursts. In a real survey, one would also want to select against short outburst-like events, such as M-dwarf flares (Chapter 7). We simulate 1,000 systems for each P_{orb} and m_{qui}. We repeat this process 500 times, and take the mean and standard deviation of the number of systems detected over the number of systems simulated as the detection probability and its associated error. We calculate the detection probability for $20\,\mathrm{min} \leq P_{orb} \leq 37\,\mathrm{min}$ in 0.2 min steps and for $14 \leq m_{qui} \leq 26$ in 0.2 mag steps, and interpolate for intermediate values.

In Figure 6.12 we show the detection efficiency of our surveys given P_{orb} and m_{qui}. We caution that these models do not account for weather and other scheduling irregularities
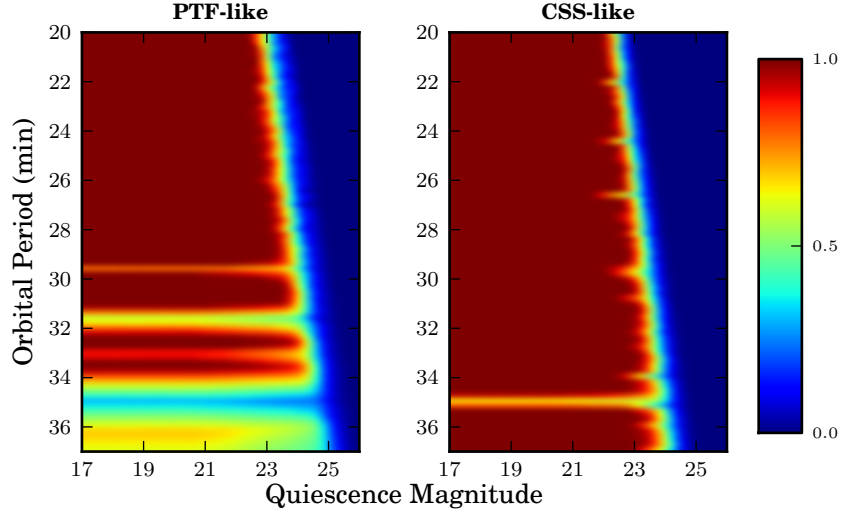
Figure 6.12 A plot of the detection efficiency of AM CVn systems given an orbital period and quiescent magnitude. A significant decrease in efficiency is seen at $P_{orb} = 35.8\,\text{min}$, as at this time the recurrence time is about one year. The PTF survey goes slightly deeper, but this is not as large an effect due to the longer baseline of the CSS. The PTF suffers at longer-orbital periods as the recurrence times increase to several years.

and, particularly in the case of the PTF-like survey, are only vaguely similar to the cadence of the survey they emulate. As expected, longer-period systems can be detected to fainter magnitudes given their increased strength, but are not as well-detected by the PTF-like survey due to its shorter baseline, relative to the $>1\,\text{yr}$ recurrence times at these orbital periods. The PTF-like survey is able to detect slightly fainter systems due to being deeper, but the longer baseline of the CSS-like survey removes this advantage.

6.4.3.2   System Evolution Models

Now that we have $\text{p}(P_{orb}, m_{qui})$, we must model the population of AM CVn systems. First, we find the fraction of AM CVn systems at each orbital period. The orbital evolution of AM CVn systems is believed to involve only the effects of gravitational wave radiation and mass transfer (Paczyński 1967). We assume that the percentage of systems at a given P_{orb} is equal to the amount of time the system spends at that orbital period over the lifespan of the system, which we define to be from $P_{orb} = 5\,\text{min}$ to $80\,\text{min}$. This ignores any changes in the birth rates of these systems.

We evolve a system with $M_{acc} = 0.6 M_{\odot}$ and $M_{don} = 0.25_{\odot}$ from $P_{orb} = 5\,\text{min}$ to longer orbital periods. The masses are arbitrary, but are in agreement with models and with the

measured masses of the components of SDSSJ0926+3624 (Copperwheat et al. 2011). To simplify the calculations, we fit these results with a power law,

$$f_{syst}(P_{orb}) = (6.9 \times 10^{-9})P_{orb}{}^{3.66}, \tag{6.1}$$

where P_{orb} is in minutes. This equation is normalized, such that $\int_{5\,\mathrm{min}}^{80\,\mathrm{min}} f_{syst}(P_{orb})\,\mathrm{d}P_{orb} = 1$.

We use the same Galactic population distribution model as Nelemans et al. (2001),

$$\rho(P_{orb}, R, z) = \rho_0 f_{syst}(P_{orb})e^{-R/H}\mathrm{sech}(z/h)^2\,\mathrm{pc}^{-3}, \tag{6.2}$$

where R is the radius from the center of the galaxy, z is the distance above the Galactic plane, ρ_0 is the population density at the center of the galaxy, H is the scale distance, and h is the scale height. We adopt, for the purposes of this calculation, the same scale height (300 pc) and scale distance (2.5 kpc) as Roelofs et al. (2007d).

The number of systems with orbital period P_{orb} at a point (r, b, l) when viewed from Earth can then be defined as

$$N_{obs}(P_{orb}, r, b, l) = r^2 \cos(b)\rho(P_{orb}, R, z)\mathrm{p}(P_{orb}, m_{qui}), \tag{6.3}$$

where b is the Galactic latitude, l is the Galactic longitude, and we can express R in terms of r, b, and l as $\sqrt{r^2 \cos^2 b + R_{GC}^2 + 2r \cos b \cos l}$. R_{GC} is 8125 pc, the distance from Sun to the Galactic Center.

We calculate m_{qui} using the distance, r, and the same parameterization for the absolute magnitude as Roelofs et al. (2007d),

$$M_{qui}(P_{orb}) = 10.5 + 0.075(P_{orb} - 30\,\mathrm{min}), \tag{6.4}$$

which is based on Figure 2 of Bildsten et al. (2006). This value for the absolute magnitude is only based on the temperature of the accretor and does not account for any luminosity from the disk. However, the disk has been measured to account for only 30% of an AM CVn system's luminosity (Copperwheat et al. 2011), so this assumption should provide a reasonable estimate.

6.4.3.3   Simulated Survey Results

We now combine our model for the detection efficiencies with that for the Galactic distribution to find the number of expected systems with $20\,\mathrm{min} \leq P_{orb} \leq 37\,\mathrm{min}$ that would be detected by our CSS-like survey and our PTF-like survey. We set ρ_0 to the most recent published population density estimates for AM CVn systems of $(5 \pm 3) \times 10^{-7}\,\mathrm{systems\,pc^{-3}}$ (Carter et al. 2013a, hereafter C13). We note that the estimates provided by C13 are relative to the Sun, while ρ_0 here is at the Galactic center.

We find that our CSS-like survey would detect $(8.3 \pm 5.0) \times 10^{-4}\,\mathrm{systems\,deg^{-2}}$ or, assuming a total coverage of $\sim20,000\,\mathrm{deg}^2$, a total of 17 ± 10 systems in total. For our PTF-like survey, we find that it would detect $(6.9 \pm 4.1) \times 10^{-4}\,\mathrm{systems\,deg^{-2}}$. With a coverage of $\sim16,000\,\mathrm{deg}^2$, we would expect a total of 11 ± 7 systems. Errors provided are only based on the error provided for the population density estimate.

Have the CSS and the PTF detected as many systems as we would expect if the population densities from Carter et al. (2013a) are correct? The CSS has detected 8 AM CVn systems in outburst with $20\,\mathrm{min} < P_{orb} < 37\,\mathrm{min}$, and another likely two systems with orbital periods in this range. The PTF has detected 6 outbursting AM CVn systems in this orbital period range, and an additional 3 systems with orbital periods likely to be in this range. This indicates that the surveys have detected, respectably, 60% and 90% of the estimated total, albeit with significant errors in these numbers. This difference is likely due to the systematic search conducted for AM CVn systems in the PTF (e.g., Levitan et al. 2013) whereas no such dedicated program exists for the CRTS. This indicates that a significant number of additional systems are likely to be found in the CSS data.

We caution that our simulations did not account for several factors. First, we did not account for scheduling irregularities and we assumed a perfect cadence. PTF, in particular, uses variable cadences. A more realistic study of PTF's AM CVn system detection efficiency based on the actual times of exposures is outside the scope of this paper. An additional observational constraint is the difficulty in confirming faint candidates. Systems with quiescent magnitudes significantly fainter than $g' \sim 21$ cannot be spectroscopically confirmed even with 8–10 m class telescopes unless caught in outburst. These factors indicate that while the CSS and the PTF may contain additional systems, many may be faint and confirming these systems will be extremely difficult.

Although this simulation considers regularly outbursting systems, we also need to consider the probability of detecting longer-period systems. Before the discovery of a 47 min photometric period in CSS0450–0931 (Woudt et al. 2013), only systems with P_{orb} below 40 min were believed to outburst. However, if, in fact, longer-period systems do outburst, and the relation in Section 6.4.2 (or a similar one) holds even for longer-period systems, this implies that CSS0450–0931 outbursts on the decade timescale. Such a timescale is not unreasonable, given the behavior of WZ Sge-type systems. The majority of AM CVn systems are believed to be long-period systems (Nelemans et al. 2001; Nissanke et al. 2012) and faint. Specifically, we can approximate that there are ∼3.2× more AM CVn systems with $37\,\text{min} < P_{orb} < 50\,\text{min}$ than with $20\,\text{min} < P_{orb} < 37\,\text{min}$ using our evolutionary model. Yet even if they are bright enough to be visible, only some will outburst during even a decade-long synoptic survey (depending on the actual outburst recurrence time), and of that sample, likely up to 75% (Table 6.3.2) will be undetected due to their short outbursts and the relatively sparse coverage of current synoptic surveys.

6.5   Conclusions

We have presented light curves of outbursting AM CVn systems drawn from three wide-area synoptic surveys. We have identified outburst recurrence times for all known outbursting systems with more than one observed outburst, and have found relationships between the orbital period and outburst strength, recurrence time, and duration. We have explored the differences between systems with recurring outbursts and only single detected outbursts, and have used the derived relations to predict the number of AM CVn systems that a PTF-like and a CSS-like survey should have observed in outburst. We find that the number of systems discovered by the PTF and the CSS are consistent with the latest population estimates, though we have not accounted for several factors in our calculations. In particular, more realistic analyses of the synoptic survey detection efficiencies for AM CVn systems are needed.

We note that this chapter is in preparation for submission to the Monthly Notices of the Royal Astronomical Society. Although the analysis performed here has shown a trend towards stronger, longer, and rarer outbursts as the orbital period of a system increases, a more quantitative approach is necessary to properly quantify the number of outbursts and

their properties. This is particularly relevant for systems with longer outburst recurrence times as it is highly likely that some outbursts were missed due to the irregular observation schedule. In particular, a Bayesian approach to calculating the outburst parameters given the observations presented here (and the lack of observations at certain times) should result in relationships that are better characterized.

Acknowledgements

Chapter 7

The AM CVn System Population Density: a Verification with Outburst-selected Systems[*]

DAVID LEVITAN[1], PAUL J. GROOT[2,1], THOMAS A. PRINCE[1], SHRINIVAS R. KULKARNI[1], RUSS LAHER[3], ERAN O. OFEK[4], BRANIMIR SESAR[1], AND JASON SURACE[3]

[1] Division of Physics, Mathematics, and Astronomy, California Institute of Technology, Pasadena, CA 91125, USA.

[2] Department of Astrophysics/IMAPP, Radboud University Nijmegen, PO Box 9010, NL-6500 GL Nijmegen, the Netherlands.

[3] Spitzer Science Center, MS 314-6, California Institute of Technology, Pasadena, CA 91125, USA.

[4] Benoziyo Center for Astrophysics, Faculty of Physics, Weizmann Institute of Science, Rehovot 76100, Israel.

Abstract

The AM CVn systems are rare, ultra-compact, semi-detached binaries with orbital periods below an hour. They are believed to be one of the end states of detached white dwarf (DWD) binaries, together with type Ia supernovae and R Cor Bor stars. Their population is poorly understood and the fraction of DWDs that survive the onset of mass transfer and an orbital period of a few minutes to become AM CVn systems is unknown. Recent observational studies of the AM CVn system population have disagreed with earlier, theoretical predictions by a factor of fifty.

---

[*]A version of this chapter is in preparation for submission to the *Monthly Notices of the Royal Astronomical Society.*

In this paper, we describe our search for AM CVn systems using the Palomar Transient Factory (PTF). We discuss the survey characteristics and our selection of candidate outbursting systems as part of the PTF outbursting system survey. We model the PTF's detection efficiency for AM CVn systems, and use this to compare our systematically selected sample with the calculated population density from the SDSS sample updated by Carter et al. (2013). We find that the number of systems the PTF has identified is consistent with their estimate of the population density. This result is particularly noteworthy since the PTF sample is most sensitive to systems with orbital periods below 30 min, while the SDSS sample is most sensitive to systems with longer-orbital periods.

7.1   Introduction

AM CVn systems are semi-detached, ultra-compact binaries. With orbital periods between 5 and 65 min, they are among the closest known stellar binaries. Although phenomenologically similar to cataclysmic variables (CVs; Warner 1995), they are evolutionarily very different, being He-rich and H-deficient, and are believed to be one of the few classes of post-period minimum binaries. These unique properties make them particularly interesting (for general reviews, see Nelemans 2005; Solheim 2010). However, one of the most challenging yet unsolved problems is that of their population density.

An accurate determination of the population density of AM CVn systems has direct relevance to several areas of astrophysics. First, AM CVn systems are strong Galactic gravitational wave sources for future space-based gravitational wave detectors (Nelemans et al. 2004). However, the number of AM CVn systems also makes them one of the most significant noise sources for such detectors as a result of confusion noise (Nelemans et al. 2001, 2004; Nissanke et al. 2012). Without a clear understanding of the population density of AM CVn systems, it is difficult to estimate their impact on realistic detector sensitivity.

Second, AM CVn systems may provide information on Galactic structure. As we describe later, standard population density models have not matched observational estimates for the AM CVn system population (Roelofs et al. 2007d; Carter et al. 2013a). However, these models have assumed "standard" Galactic scale height estimates, something that is not known to be correct. Recent work has suggested the possibility of multiple populations of AM CVn systems (Nissanke et al. 2012).

Lastly, an important formation channel for AM CVn systems is believed to be from detached white dwarf binary systems (Nelemans et al. 2001). These white dwarf binaries are also believed to be progenitors for type Ia supernovae and other exotic stars such as R Cor Bor stars (Webbink 1984). The fraction of type Ia supernovae from the double-degenerate channel could be found if the population density of the other outcomes was known.

AM CVn systems are typically identified from their He-rich, H-deficient spectra (e.g., Marsh et al. 1991). They are nominally known to have three distinct phenomenological states. Those with $P_{orb} < 20$ min are "high"-state systems, with an optically thick disk and absorption line spectra. Those with $P_{orb} > 40$ min are "quiescent" systems, showing emission-line spectra and an optically thin disk. Lastly, those with orbital periods between these two extremes (though see Woudt et al. 2013 and Chapter 6) are known as outbursting systems, and change from the characteristics of a high state system to a quiescent system with a luminosity difference of 3–6 mag between states.

Despite its significance, the population density of AM CVn systems has proven elusive to find. AM CVn, the prototype star, was first proposed to be an ultra-compact binary by Smak (1967). From then until the availability of the SDSS archive in the early 2000's, fewer than a dozen systems were identified, all serendipitously. Thus, systematics and biases were impossible to identify and only population synthesis estimates were thought to provide the best results (e.g., Nelemans et al. 2001).

The first systematically selected sample of AM CVn systems was found in the SDSS spectroscopic survey, from which seven new AM CVn systems were identified (Roelofs et al. 2005; Anderson et al. 2005, 2008) by their distinct He-emission line spectra. It was hoped that a population density calculation based on this sample would match the earlier population synthesis estimates from Nelemans et al. (2001), hereafter N01. Roelofs et al. (2007d), hereafter R07, "calibrated" the population density results with the results from the SDSS spectroscopic survey, finding a factor of 10 decrease in the population density. However, the SDSS spectroscopic survey has complex color selection criteria and only ~20% coverage for blue stars. This was accounted for by R07, but required a large scaling factor.

The next large sample of AM CVn systems has come from a follow-up survey to the earlier SDSS sample. Roelofs et al. (2009) showed that the majority of AM CVn systems are extremely blue and are in a relatively sparse area of color-color space. A project was

launched to obtain low-resolution spectra of every star identified from an observationally-determined color-color selection of the SDSS photometric data. The project has thus far identified a total of seven new color-selected AM CVn systems (Roelofs et al. 2009; Rau et al. 2010; Carter et al. 2013a), well below the original estimates of over forty.

Although the search for AM CVn systems in the SDSS is now approaching 100% completion, it is important to consider several limitations of this search. First, the survey is most sensitive to systems with relatively long orbital periods ($P_{orb} > 30$–$40\,$min). Longer-period systems tend to have narrow and strong He-emission lines (e.g., Marsh et al. 1991) whereas shorter-period systems, those that are believed to outburst, have much broader lines and, when outbursting, are observed to have absorption lines instead of emission lines (e.g., Roelofs et al. 2006a). While AM CVn systems evolve towards longer-orbital periods and it is believed most systems will be found in the longer-orbital period regime (Nelemans et al. 2004; Nissanke et al. 2012), confirmation with shorter-orbital period systems is necessary.

Two significant assumptions make it difficult to know whether the updated population estimates by Carter et al. (2013a), hereafter C13, are accurate. First, the color selections, both for the SDSS spectroscopic and the follow-up surveys, are complex, and it would not be surprising if some AM CVn systems were missed due to different colors (for an example of such a system, see Levitan et al. 2013). Second, R07 and C13 assumed a single Galactic scale-height of $300\,$pc. However, this number has not been observationally verified (Nissanke et al. 2012).

The Palomar Transient Factory Outbursting System Survey was started to acquire a systematically selected sample of outbursting systems in a color-independent fashion. The Palomar Transient Factory (PTF) is a wide-area, synoptic survey. Candidate outbursting systems are selected from PTF light curves, and all candidates are classified with low-resolution spectroscopy. As part of the project, we have thus far identified 7 new AM CVn systems and one candidate (Levitan et al. 2011, 2013, Chapter 5), as well as >200 cataclysmic variables (Groot et al. in prep).

This survey and the resulting sample is complementary to the SDSS sample described earlier. First, the PTF is most sensitive to those systems with orbital periods below $35\,$min, as these are known to outburst more frequently (Ramsay et al. 2012, Chapter 6). As such, it samples a different orbital-period regime. Second, by selecting systems based on outburst properties only, we can eliminate the color bias present in the earlier surveys (though, of

course, other biases are present). However, this sample is realistically too small to provide a good sample for a definitive population study. Hence, we concentrate on exploring whether current population density models are consistent with our discoveries.

We begin, in Section 7.2, by describing the PTF and the PTF Outbursting System Survey in greater detail, including the pipeline, quality metrics, and observation strategy. In Section 7.3, we describe the models we use for the AM CVn population. Section 7.4 describes our AM CVn system detection efficiency calculation. In Section 7.5, we calculate population results and compare to previous population estimates.

7.2   The PTF Outbursting System Survey

The PTF Outbursting System Survey used the PTF to identify outbursting systems. In total, we discovered 8 new AM CVn systems (Levitan et al. 2011, 2013, Chapter 5) and >200 CVs (Groot et al. in prep). In Table 7.2, we list the outbursting AM CVn systems for which there exist PTF light curves. We constrain our analysis to those seven systems that have (or are believed to have) $20\,\text{min} \leq P_{orb} \leq 37\,\text{min}$. This allows us to use the relationships between outburst properties and orbital periods developed in Chapter 5, where we found that all systems with multiple recorded outbursts in $10\,\text{yrs}$ of photometric data have $P_{orb} \leq 37\,\text{min}$.

7.2.1   The Palomar Transient Factory

The PTF (Law et al. 2009; Rau et al. 2009) used the Palomar $48''$ Samuel Oschin Schmidt telescope to image up to $\sim 2,000\,\text{deg}^2$ per night with a pixel scale of $1.01''\,\text{pix}^{-1}$. Exposures were $60\,\text{s}$ and were taken with a Mould-R or Gunn-g' filter. We refer the reader to Law et al. (2009) for details on the PTF hardware. The PTF project obtained data from March 2009 through the end of 2012. Subsequently, the intermediate Palomar Transient Factory (iPTF) project began using the same hardware and software. In this paper, we only consider data from the PTF.

PTF observations are organized into a tiling system covering the entire sky. Each field is assigned a unique, numerical "Field ID." The PTF camera uses eleven 2048×4096 CCDs, numbered 0–11 (but excluding the inoperable CCD 3). Thus, each exposure is associated with a field, chip, and filter. Hereafter, we refer to the unique combination of these three

Table 7.1. AM CVn systems with outbursts detected by the PTF.

System	m_{qui}	P_{orb} (min)	b	l	d[a] (pc)	Refs
PTF1J1919+4815	21.5	22.5	16	80	2057	1
CR Boo	17.4	24.5	66	341	290	2
PTF1J0719+4858	19.4	26.8	24	169	674	3
CP Eri	20.3	28.7	53	192	954	4
PTF1J0943+1029	20.7	30.4	43	224	1083	5
PTF1J1632+3511	23.0	$\cdots$ [b]	43	57	$\cdots$	5
PTF1J2219+3135	20.6	$\cdots$ [b]	21	89	$\cdots$	5
SDSSJ1721+2733	20.1	38.1	31	50	629	6,7
CSSJ0450-0931	20.5	47.3	31	208	550	8
PTF1J0857+0729	21.8	$\cdots$	31	221	$\cdots$	5
PTF1J1523+1845	23.5	$\cdots$	54	28	$\cdots$	5

[a]Distance is based on the absolute magnitude model as described in Section 7.3.2.

[b]The orbital period is believed to be $\leq 37\,\mathrm{min}$ based on outburst recurrence times (Chapter 6).

Note. — Only AM CVn systems with outbursts detected by the PTF as defined in Section 7.2.2 are listed here. For a recent, complete list of outbursting AM CVn systems, including all those with data from the PTF, we refer the reader to Chapter 6. This paper uses only those systems with P_{orb} below (or believed to be below) 37 min, which are in the first group of the table.

References. — (1) Chapter 5; (2) Patterson et al. (1997); (3) Levitan et al. (2011); (4) Groot et al. (2001); (5) Levitan et al. (2013); (6) Rau et al. (2010); (7) Augusteijn, T, (priv. comm.); (8) Woudt et al. (2013)

IDs as a "pointing."

Two primary pipelines process the PTF data. The "transient" pipeline uses difference images for the real-time detection of transient events (Gal-Yam et al. 2011). Although some of the PTF-discovered AM CVn systems were initially treated as transient events (Levitan et al. 2011, 2013), we do not use data processed through this pipeline here.

7.2.1.1   The Photometric Pipeline

The "photometric" pipeline, in contrast, prioritizes photometric and astrometric accuracy over processing speed. Raw images are initially de-biased and flat-fielded using standard procedures. Astrometric calibration is performed using a combination of SCAMP (Bertin 2006) and ASTROMETRY.NET (Lang et al. 2010). Flux measurements are made using sextractor's MAG_AUTO (Bertin & Arnouts 1996). Further details will appear in Laher et al. (in prep).

Photometric calibration is carried out in two steps. First, the zero-points for exposures of SDSS fields observed in the same night are fit using a formula accounting for airmass, time of night, and other factors. Zero-points for all exposures are then found from the fit parameters to a typical accuracy of a few percent (Ofek et al. 2012). We emphasize that these fit parameters are on a per night basis and are calibrated to the SDSS catalog.

Better photometric accuracy, as well as removal of the effects of changing weather, requires relative photometric techniques and the construction of light curves. We begin by co-adding the best exposures to obtain a co-added image with a 5σ limiting magnitude of $21.7 \leq R_{lim} \leq 23.2$. The sources found in this image are used to generate a "reference" catalog, and source detections from individual exposures are matched to this catalog with a matching radius of $1.5''$. Detections not matched to the reference catalog are saved to a separate "transient" catalog. Reference catalogs are calibrated to an absolute scale by comparing to the earlier-described absolute calibrations of individual exposures.

We then apply a relative photometric calibration to the light curves using the algorithm described in Ofek et al. (2011) and Levitan et al. (2011) on a per pointing basis. This step both corrects for changing weather conditions that give a poor fit for the initial SDSS-derived calibration and improves overall photometric performance to 6–8 mmag at the bright end of $14.5 < R < 16.0$ and ~ 0.2 mag at the faint end of $R \sim 21$ (Figure 3.4). Typical systematic errors for photometric measurements of sources on exposures in good conditions are $<1\%$,

as measured by a comparison of the measurements of bright stars in one exposure to their median magnitudes based on all exposures. We note that not all exposures are calibrated in this fashion, as it requires a sufficient number of exposures to generate a reference image. All light curves, together with exposure information, are stored in PyTables (Alted et al. 2002) files and are collectively referred to as the "PTF photometric database." In this paper, we only consider the data successfully calibrated through this pipeline, which constitutes all but a few percent of all data acquired by the PTF.

7.2.1.2 Photometric Performance

A fairly typical example of photometric performance was presented in Figure 3.4. For a more robust test, we modeled the rms vs. magnitude on a per pointing basis using the following relation from (Findeisen et al. 2013),

$$RMS = \sqrt{a^2 + [b \times 10^{0.4p(\text{mag}-14.5)}]^2}.$$

We found median values from our fits of $a = 0.0$, $b = 0.013$, and $p = 0.48$. The lack of a constant term is somewhat puzzling, but may be explained by the asymptotic behavior of the equation and the low systematic error in the PTF photometry.

7.2.1.3 Coverage Maps

The PTF obtained 244,544 exposures in R and 40,806 exposures in g'. The total sky coverage processed through the photometric pipeline is $17,500\,\text{deg}^2$ in R and $\sim6,400\,\text{deg}^2$ in g'. Since almost every field covered in g' is also covered in R, we restrict our analysis to only the data from R-band. We present coverage maps of the PTF survey in R-band in Figure 7.1.

7.2.1.4 Limiting Magnitudes

A crucial step in this process is the calculation of limiting magnitudes. Two sets of limiting magnitudes are calculated. First, a 5σ limiting magnitude is derived for each exposure based on known CCD characteristics, the seeing, and background levels. This value has been observed to be roughly correct for photometric nights, but can often be fooled by poor weather or seeing (typically a result of incorrect zero-points generated by
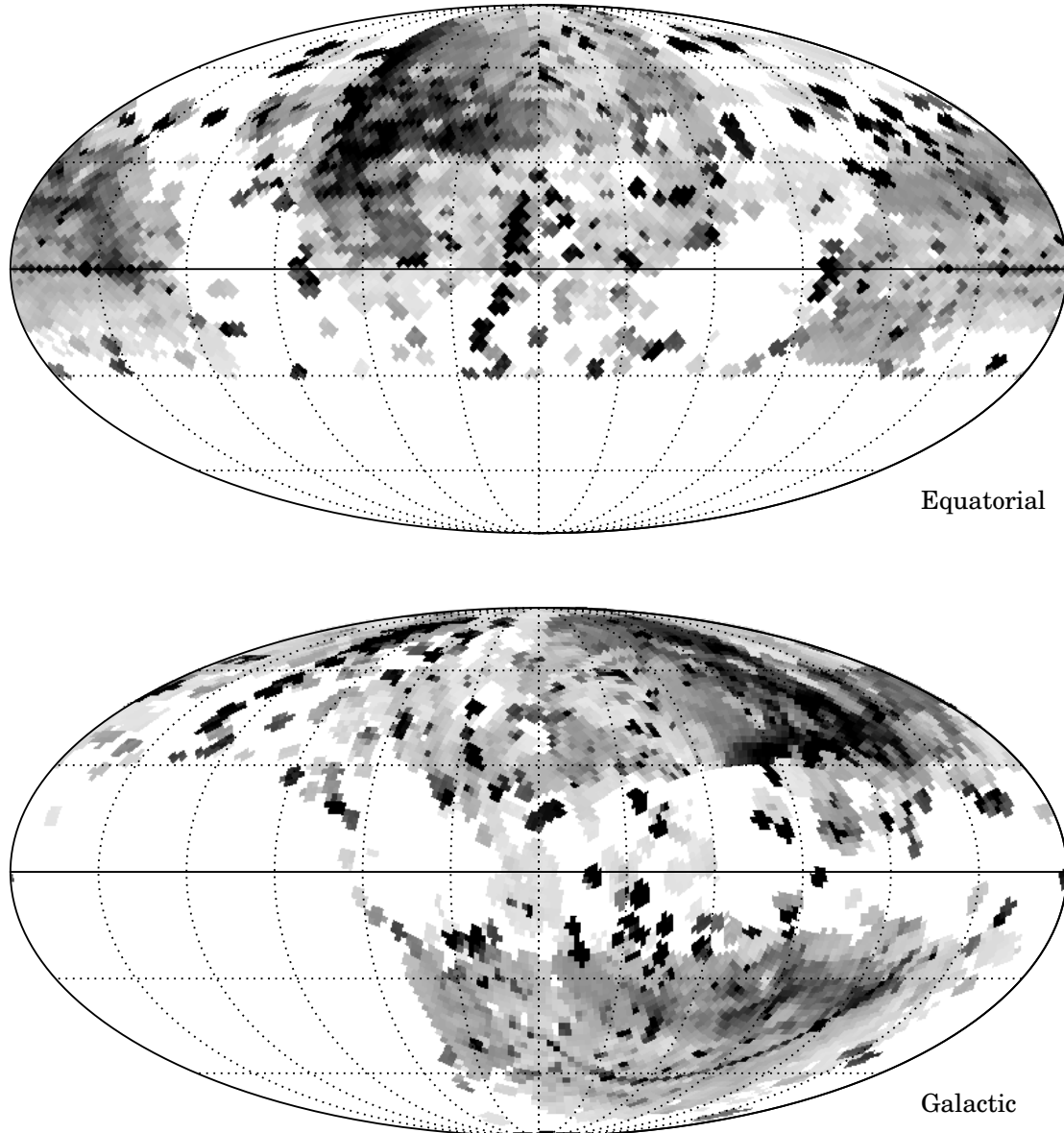
Figure 7.1 Coverage maps showing the number of exposures taken by the PTF per area of the sky over the course of the project. North is up in these maps, while East is to the left. Darker colors indicate more exposures — white indicates 0 exposures while black indicates 100 exposures. The top map is in Equatorial coordinates, while the bottom map is in Galactic coordinates.
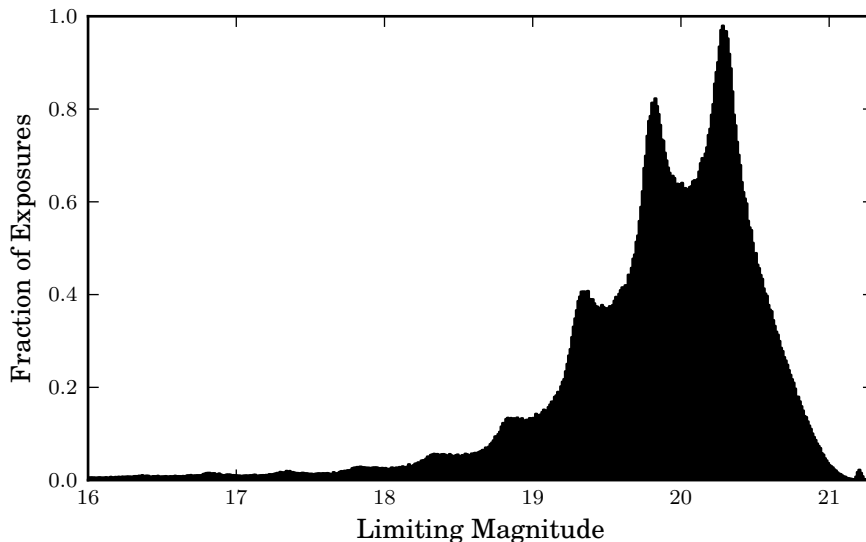
Figure 7.2 The 95% limiting magnitude of all R-band PTF exposures calibrated with relative photometry. The peak of the histogram is at $R \sim 20.3$ and the median limiting magnitude is $R \sim 20.0$. We do have have a complete explanation for the multi-modal distribution, but it is likely due in part to lunation, as plotting only observations during dark time makes the distribution much more single-peaked. Although full moon is typically reserved for the Hα survey, this was not always the case, particularly at the beginning of the survey.

the comparison to SDSS photometry).

To obtain accurate zero-points for all exposures, we separately calculate an observationally-defined limiting magnitude. We first perform a conservative, but simple, selection of stars. We assume all sources with $14.5 < m < 16$ are stars, and find the median and robust standard deviation of $\mu_{max}-$MAG_AUTO for these sources, where μ_{max} is an aperture-photometry measurement of each source that uses only the pixel with the highest flux. Cosmic ray hits, which are concentrated in only 1 or 2 pixels, will have a value near 0, while galaxies will be extended sources and thus have a high value. We use these values to select likely stars from the exposure, and for each 0.5 mag bin we compare the number of detected stars to the number of reference stars. We then fit an arctan function to these values, and calculate the magnitude at which 95% of stars in the reference image are detected in the individual exposure. We present a histogram of limiting magnitudes in Figure 7.2.
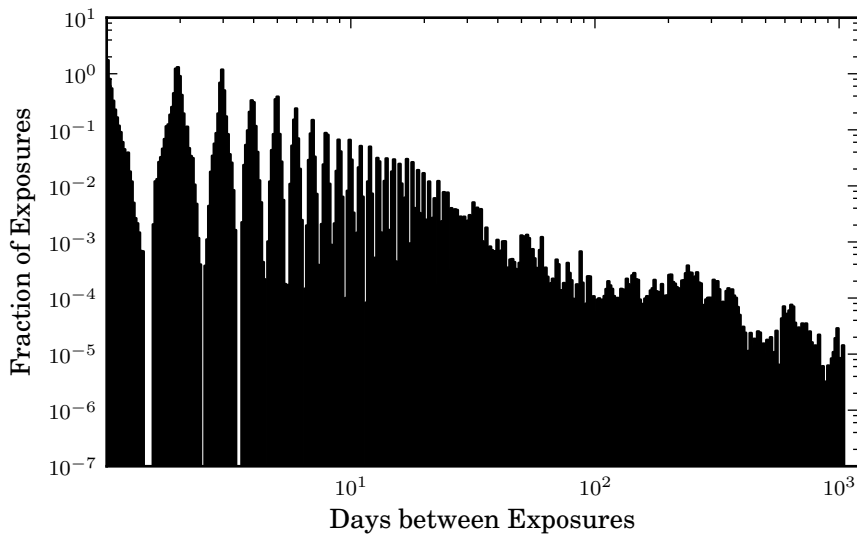
Figure 7.3 A histogram of the time between exposures. Most consecutive exposures of the same pointing are either $< 1\,\mathrm{d}$ or 2–$3\,\mathrm{d}$ apart, consistent with the nominal cadence of the PTF. The former are to verify that variability is not due to asteroids.

7.2.1.5 Cadence

Lastly, we consider the cadence of the PTF. Since the PTF was originally designed as a supernova survey, the default cadence has been 3–$5\,\mathrm{d}$, with two exposures per night separated by at least 30 minutes to identify asteroids. However, multiple other experiments have resulted in a variety of cadences, down to a few minutes. Nights around the full moon are typically used for an Hα survey. We present a histogram of cadences in Figure 7.3.

7.2.2 Outbursting Candidate Selection

We identified and classified outbursting systems in two steps. First, we used the PTF photometric database to identify sources with outburst-like light curves using a defined set of criteria. Next, after removing any "fake" outbursting systems by manual inspection of the light curves, we obtained low-resolution, classification spectra of the remaining candidates, and used these spectra to classify each candidate as an AM CVn system, CV, or background source.

The candidate selection criteria were designed to select AM CVn systems and CVs (since outbursts of the two classes are similar) while selecting against background sources, including M-dwarf flares, asteroids passing over stars, and artifacts in the data. The signature features of AM CVn system outbursts are the duration, of one to several weeks, and

strength, 3–6 mag (Ramsay et al. 2012, Chapter 6). In contrast, M-dwarf flares typically last less than a day, while almost all asteroids move rapidly enough to leave the vicinity of a star within an hour. Since the PTF often has unpredictable cadences that will not catch an outburst near peak, we used a lower outburst strength criterion than the 3–6 mag peak of AM CVn system outbursts.

We searched through all light curves for light curves showing Δmag ≥ 1.5 relative to the quiescent magnitude, defined as the fainter of the reference magnitude (Section 7.2.1.1) and the median magnitude based on all observations. For each of these light curves, we identified whether there were two consecutive measurements in outburst. We required the first measurement to be ≥ 1.5 mag brighter than the quiescent magnitude, while the second measurement only needed to be $\geq 5\sigma_{R,point}$ brighter than the quiescent magnitude, where we define $\sigma_{R,point}$ to be the median rms scatter of sources with similar magnitudes as the quiescent magnitude of source candidates (see Figure 3.4). This identified several thousand candidates.

The majority of these candidate light curves, however, were not real outbursts, but optical artifacts. These "ghosts" were caused by the reflection of extremely bright stars in the PTF telescope and camera system. We elected to manually sort through this list of candidates, and identified $\sim$300 outbursting candidate sources in the PTF data. Additional candidates were easily identifiable as long-period variables. Our main remaining contamination was from variable blazars and AGNs, which often have unpredictable variability.

We obtained low-resolution classification spectra of all but the 10 faintest ($g' > 22$) candidates, using a variety of telescopes, but primarily the Palomar 200″ Hale telescope with the DBSP spectrograph (Oke & Gunn 1982) and the Keck-I 10 m telescope with the LRIS spectrograph (Oke et al. 1995). Spectra were reduced using either standard routines in IRAF or optimal extraction as implemented in the PAMELA code (Marsh 1989), as well as the STARLINK packages KAPPA, FIGARO, and CONVERT. Systems were typically observed in quiescence and the distinctive He emission lines were straightforward to identify. We refer the reader to Levitan et al. (2011), Levitan et al. (2013), Chapter 5, and Groot et al. (in prep) for details on the identified AM CVn systems and CVs.

7.3   AM CVn System and Population Models

With fewer than forty known systems, multiple possible evolutionary pathways (N01), and unknown distances for the majority of systems (Roelofs et al. 2007a), the population of AM CVn systems has proven difficult to understand. Both the population synthesis models in N01 and the observationally-determined population density from R07 have not been supported by later observations (C13). Here, we use the PTF sample to obtain an independent estimate of the AM CVn system population by using the AM CVn systems detected in outburst by the PTF with $20\,\mathrm{min} < P_{orb} < 37\,\mathrm{min}$. We limit our study to this period range since Chapter 6, hereafter L13, found relationships between the outburst properties of systems in this period range and their orbital periods, while outbursts for longer-period systems are poorly understood. Now that we have described the PTF and our outbursting candidate selection mode, we describe the models used to simulate AM CVn systems and their distribution.

7.3.1   System and Orbital Evolution Models

AM CVn systems are believed to evolve from three possible classes of progenitors: detached white dwarf (WD) binaries, evolved He-star binaries, and evolved CVs. In all three cases, the progenitor evolves with a negative period derivative until reaching a minimum orbital period, at which time, if the mass transfer is stable, the donor becomes (semi-)degenerate, the system passes through a period minimum, and the system begins to increase in orbital period. This is perhaps best summarized in Figure 1 of Nelemans (2005). In the case that mass transfer is unstable, the components will end up merging (N01). It is believed that the detached WD channel is the dominant channel (N01), although no system has had its progenitor conclusively determined (Roelofs et al. 2007a; Nelemans et al. 2010). A substantial number of detached WD binaries are known, many of which are believed to be AM CVn system progenitors (Kilic et al. 2012). No candidate progenitor systems have been discovered that represent the other two channels, though recent discoveries of systems with $P_{orb} < 2\,\mathrm{hrs}$ and similar characteristics to those predicted (Breedt et al. 2012; Carter et al. 2013b; Geier et al. 2013) may indicate that such systems do exist.

In this paper, we assume all systems evolve from the detached binary WD channel, since its orbital evolution is the most straightforward and best understood. For this channel, it

is believed that the two progenitor WDs evolve closer together due to gravitational wave radiation (Landau & Lifshitz 1971). The less massive system eventually fills its Roche lobe and mass transfer is initiated. For systems with extreme mass ratios, the angular momentum transfer overpowers the gravitational wave radiation, and the system passes through an orbital period minimum and begins to evolve towards longer orbital periods (Paczyński 1967; Marsh et al. 2004). It is believed that even after birth AM CVn systems continue to evolve under this orbital evolution model. However, it is not known if there are secondary factors involved and the relatively low number of systems makes such a study difficult.

Since it is believed that the luminosity of the system changes with orbital period (see Section 7.3.2), we must incorporate an orbital period distribution into our calculations. We use the same model as L13, wherein we evolve two WDs from $P_{orb} = 5\,\mathrm{min}$ to $P_{orb} = 80\,\mathrm{min}$ using the equations for gravitational wave radiation and mass transfer (Paczyński 1967). We set initial masses of $0.6M_\odot$ and $0.25M_\odot$. These are somewhat arbitrary, but are in agreement with models and with the masses of the components of the only fully eclipsing AM CVn system, SDSSJ0926+3624 (Copperwheat et al. 2011). We then assume that the percentage of systems at a particular P_{orb} is equal to the time spent there. To simplify the calculations, we fit this distribution with a power law,

$$f_{syst}(P_{orb}) = (6.9 \times 10^{-9})P_{orb}^{3.66}, \tag{7.1}$$

where P_{orb} is in minutes. This equation is normalized, such that $\int_{5\,\mathrm{min}}^{80\,\mathrm{min}} f_{syst}(P_{orb})\,\mathrm{d}P_{orb} = 1$.

7.3.2   System Luminosity Model

For any population study, the apparent magnitude of a system must be related to its absolute magnitude. Since only a few systems have measured distances and most systems are too faint for parallax measurements (e.g., Roelofs et al. 2007a), we must rely on a luminosity model. Three components are believed to contribute to the luminosity of an AM CVn system: the accretor, the accretion disk, and the hot spot where transferred matter interacts with the disk. The donor star is not believed to make any significant contribution to the luminosity. The ratio of these components are known only for the eclipsing, 28 min orbital period system SDSSJ0926+3624, and are roughly 70% for the accretor, 20% for the

disk, and 10% for the hot spot (Copperwheat et al. 2011). The luminosity of the hot spot is consistent with that found for the partially eclipsing AM CVn systems, PTF1J1919+4815 (Chapter 5).

Roelofs et al. (2007d) used a parameterization of Figure 2 in Bildsten et al. (2006) to estimate the absolute magnitude of the accretor based on its thermal state,

$$M(P_{orb}) = 10.5 + 0.075(P_{orb} - 30 \, \text{min}), \tag{7.2}$$

where M is the absolute magnitude. R07 assumed that this is a valid estimate not only for the accretor but also for the system overall, which is likely true for the mostly longer-period systems that have been found by the SDSS. The PTF-discovered systems are concentrated much more heavily below orbital periods of 30 min.

We continue to use this relationship, as it is the best estimate for the absolute magnitude of the system. It is known that shorter-period systems have a substantial contribution from the disk. However, if the majority of the luminosity is from the accretor, then this is a reasonable estimate. We test this by using two systems with measured distances. First, we consider CR Boo, which has a quiescent magnitude of $m_g \sim 17.5$ (see Kato et al. 2000, as well as more recent data in Chapter 6). Roelofs et al. (2007a) found that CR Boo is 337^{+44}_{-35} pc from the Earth, which combined with its orbital period of 24.5 min yields an apparent magnitude estimate of $m_g \sim 17.7$. If the expected luminosity of the disk, 30%, is added, this is roughly equal to the observed quiescent magnitude. Second, we test V803 Cen, which has been recorded at a minimum of $V = 17.2$ (Patterson et al. 2000) and whose distance and period have been measured to be 347^{+32}_{-27} pc (Roelofs et al. 2007a) and 26.6 min (Roelofs et al. 2007b), respectively. Equation 7.2 predicts that V803 Cen should have a quiescent magnitude of 18.0. The difference between V803 Cen's predicted and measured luminosities are somewhat larger than that for CR Boo. However, we note that V803 Cen's photometric behavior is different than the majority of outbursting systems (Chapter 6) and that this may contribute some of this difference. Overall, the model appears to be relatively consistent with observations even for shorter-period systems.

7.3.3 Galactic Distribution Model

Galactic population distributions of stars are typically modeled using a scale height and distance and assume a single population. N01, as well as other studies of compact binary populations, have used

$$\rho(R, z) = \rho_0 e^{-R/H} \text{sech}(z/h)^2 \, \text{pc}^{-3}, \qquad (7.3)$$

as the model, where R is the distance from the center of the Galaxy, z is the height above the Galactic plane, ρ_0 is the population density at the center of the Galaxy, and H and h are, respectively, the scale distance and scale height. We note that R07 and more recent studies assume a more complicated model for the scale distance, but for the case of AM CVn systems detectable from optical observations, this does not have a significant effect. We also note that the population density estimates typically provided are the local density and must be scaled to ρ_0, the density at the Galactic center, used in Equation 7.3. H has been well established as 2.5 kpc (Sackett 1997) and does not change significantly between stellar classes.

The scale height, h, however, is dependent on the type of system being modeled. Typical values are 300 pc for stars in the thin disk, where younger populations are believed to be, and 900 pc for the thick disk, primarily composed of older populations (Jurić et al. 2008). R07 and C13 used $h = 300$ pc, but this was a semi-arbitrary decision at best and is, in fact, not necessarily consistent with the belief that most AM CVn systems are older systems. Since the scale height of AM CVn systems is not well established and difficult to test, we leave this as a free parameter in our study.

7.3.4 Outburst Light Curve Models

The long-term photometric variability of AM CVn systems was studied using data from three synoptic surveys by L13. We briefly describe the results here, but refer the reader to the original paper for details. L13 confirmed the predictions from Levitan et al. (2011) and Ramsay et al. (2012) that there is an overall positive trend in the super-outburst recurrence time with respect to orbital period. Additionally, L13 also showed that both the outburst strength and duration also increases with orbital period below $P_{orb} = 37$ min. The behavior of systems with longer orbital periods is poorly understood, due to a lack of knowledge of their recurrence times.

Chapter 6 fit the data from the long-term light curves and found the following relations:

$$P_{so} = 0.165e^{0.219P_{orb}} + 14.8$$

$$\Delta\mathrm{mag} = 0.13P_{orb} - 0.16$$

$$t_{dur} = 0.39e^{0.122P_{orb}} + 7.9,$$

where P_{orb} is the orbital period in minutes, P_{so} is the super-outburst recurrence cycle time in days, $\Delta\mathrm{mag}$ is the difference between peak outburst magnitude and quiescence magnitude, and t_{dur} is the duration of the outburst in days. We use these relations in our analysis of PTF AM CVn system detection efficiency (Section 7.4).

We also continue to use the outburst light curve model adapted by L13 for shorter-orbital period systems. Specifically, they modeled the outburst of AM CVn systems as a sudden increase to peak magnitude, followed by a decrease over t_{dur} to $0.5\,\mathrm{mag}$ above quiescence. The system then drops back to quiescence until the start of the next outburst cycle (i.e., for $P_{so} - t_{dur}$ days).

7.4   AM CVn Systems in the PTF Data

We now combine PTF exposure information with the models for AM CVn systems described in Section 7.3 to simulate how many systems should be detected by the PTF. We first find $\mathrm{p_{point}}(P_{orb}, m_{qui})$, the probability of detecting an AM CVn system in a particular pointing, for the PTF.

We use a bootstrap approach (Efron 1982), similar to that used by L13, to calculate the probabilities. For each PTF pointing, P_{orb}, and m_{qui}, we generate 1,000 simulated systems with varying zero-phases for their outburst cycle. We compute the magnitude of each system using the light curve models from Section 7.3.4 at the time of each exposure taken for the pointing, and compare it to the limiting magnitude for that exposure. We consider any detection at or brighter than the limiting magnitude to be a detection. If the detections satisfy the outburst criteria from Section 7.2.2 (with the exception that we know the quiescent magnitude a priori) we consider that the system was detected in outburst. The ratio of detected, outbursting systems to all simulated systems is then $\mathrm{p_{point}}(P_{orb}, m_{qui})$.

Quiescence Magnitude
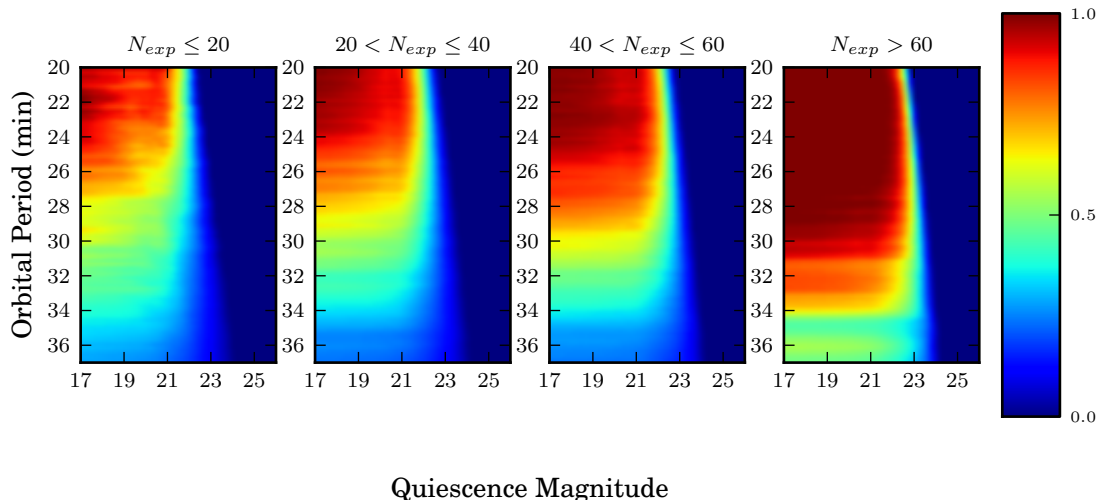
Figure 7.4 The median detection probabilities for AM CVn systems in the PTF-given orbital period and quiescent magnitude. Four ranges of the number of exposures per pointing are provided. As the number of exposures increases, the probability of detecting systems increases, particularly at the longer-orbital periods. Cadences are typically 3–5 days, though different for each pointing based on PTF scheduling (Figure 7.3).

7.4.1 Detection Probability Results

We calculated the detection probabilities for AM CVn systems with $20\,\mathrm{min} < P_{orb} < 37\,\mathrm{min}$ in $0.2\,\mathrm{min}$ steps and for quiescent magnitudes of $17 < V < 26$ in $0.2\,\mathrm{mag}$ steps. We present the median detection probabilities in Figure 7.4, separated into several figures by the number of exposures. In general, we see that the PTF cannot probe much past $R \sim 23$ and is most successful at detecting shorter-period systems. The inefficiency at detecting longer-period systems is due to their much longer outburst recurrence times — often times longer than the baseline of observations for a PTF pointing.

In Figure 7.5, we plot the detection probability of systems with respect to their P_{orb} and distance, as calculated using Equation 7.2. We see that the PTF can identify systems to $4\,\mathrm{kpc}$, significantly past any proposed Galactic scale heights for the AM CVn population.

The variety of the PTF's observation schedules gives us the opportunity to explore how many exposures at the PTF's nominal cadence of 3–5 days are needed to detect an AM CVn system. In Figure 7.6, we present a plot of the probability of detection vs. number of observations for AM CVn systems with $P_{orb} = 23\,\mathrm{min}$, $30\,\mathrm{min}$, and $37\,\mathrm{min}$, for the quiescent magnitude range $17 < V < 21$. As expected, the number of exposures necessary
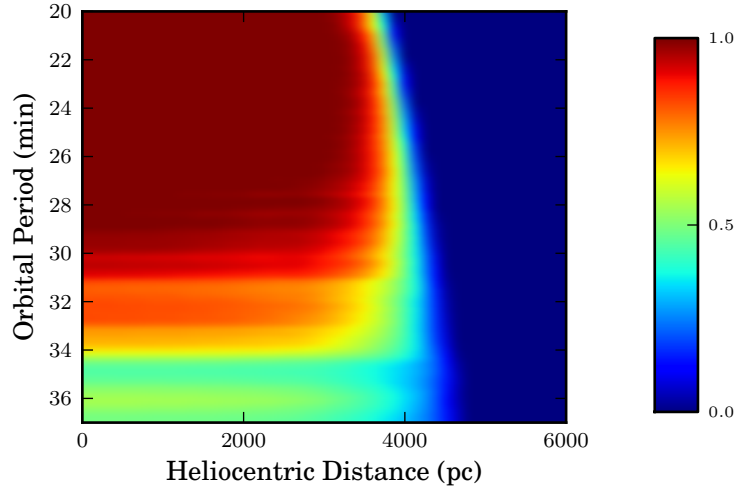
Figure 7.5 The probability of AM CVn system detection by the PTF vs. the distance of the system from Earth. This plot is generated for pointings with $N_{exp} > 60$. The PTF can detect systems out to 3.5–4 kpc.

to detect a systems increases significantly with the orbital period. Shorter-period systems can be detected with only twenty-five observations, while longer-period systems can require hundreds. Given that very few PTF pointings have more than 100 exposures, the lack of detection of longer-period systems is consistent with these results.

7.4.2 The Number of Observable Systems

To calculate the number of systems the PTF should be able to identify, given ρ_0, h, and $p_{point}(P_{orb}, m_{qui})$, we follow a similar approach to that of R07. The observable density of systems at a point in the Galaxy is

$$\rho_{obs}(P_{orb}, r, b, l) = r^2 \cos(b) \rho(R, z) p_{point}(P_{orb}, m_{qui}) f_{syst}(P_{orb})$$

where r is the distance from the Sun, b is the Galactic latitude, l is the Galactic longitude, and R is the distance from the center of the Galaxy along the Plane. We define R in terms of r, R_{GC} (the distance of the Earth from the Galactic Center), and the Galactic coordinates, b and l, as $R = \sqrt{r^2 \cos^2 b + R_{GC}^2 - 2rR_{GC} \cos b \cos l}$. The total number of systems, then, is the integral of ρ_{obs} over the sky area of interest, from $r = 0$ to the distance limit of the survey of interest, and over the range of periods of interest.

In practice, we simplify the calculation of the number of systems found in a particular
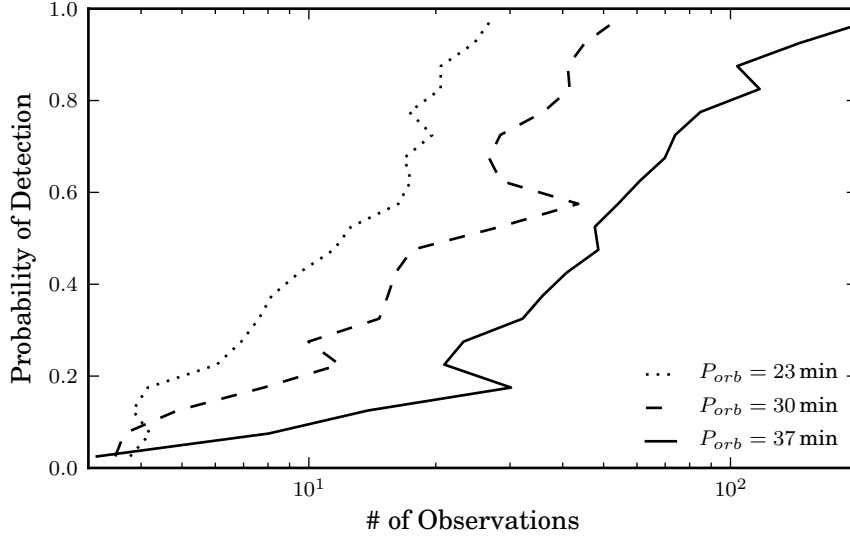
Figure 7.6 A plot of the the probability of detecting an AM CVn system vs. the number of observations. The three lines are for the orbital periods of 23 min, 30 min, and 37 min and are plotted based on 1% bins. Data is generated by taking the median probability of detecting a system at the specific P_{orb} with $17 \leq m_{qui} \leq 21$ and plotting a histogram with the number of exposures. The number of observations needed to detect short-period systems is around 25, while longer-period systems need substantially more.

PTF pointing to

$$N_{obs,point} = \Omega_{PTF} \int_{0}^{r_{max}} dr \int_{P_{min}}^{P_{max}} dP \, r^2 \rho_{obs}(P_{orb}, r, b, l) \mathrm{p}_{point}(P_{orb}, m_{qui}), \qquad (7.4)$$

where r_{max} is the maximum distance at which PTF can detect a system (see Figure 7.5, but this can be set to a large number as long as p_{point} is 0 for undetectable systems) and Ω_{PTF} is the area covered by one PTF pointing, $0.7 \deg^2$. The Galactic coordinates b and l are set on a per-pointing basis. The total number of systems detectable by the PTF is then:

$$N_{obs,PTF} = \sum_{pointings} N_{obs,point} \qquad (7.5)$$

Equations 7.4 and 7.5 are the equivalent of Equation 1 in R07. In Figure 7.7, we plot the expected total number of systems detected in all PTF pointings vs. scale height and ρ_0.
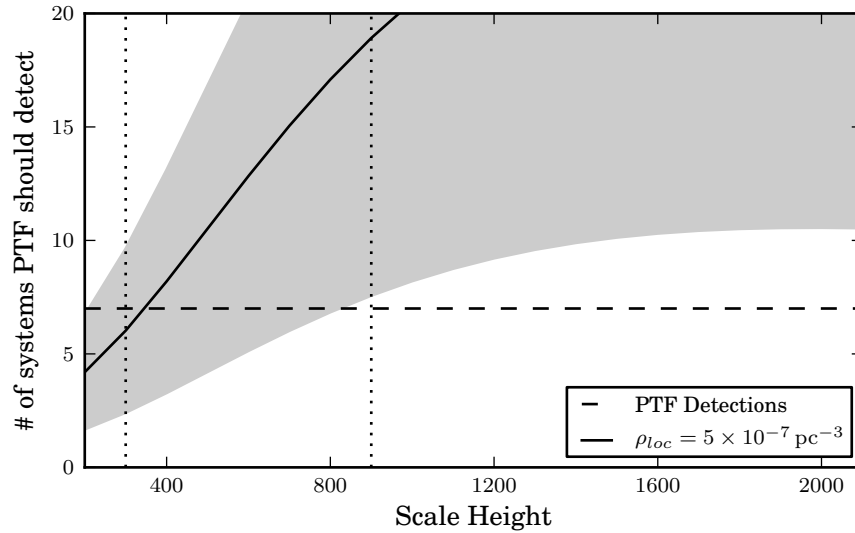
Figure 7.7 The expected number of AM CVn systems with $20\,\mathrm{min} < P_{orb} < 37\,\mathrm{min}$ that would be detected by the PTF as a function of the population density, ρ_0, and the scale height, h. The dashed line indicates the number of systems observationally detected by the PTF. The solid line is the number of systems that the PTF should detect assuming that the local space density is $5 \times 10^{-7}\,\mathrm{pc}^{-3}$, the population density estimate from C13. The gray area represents the 1σ estimate as given by C13 on the population density. The number of systems increases with scale height since the majority of PTF observations are at moderate Galactic latitudes and the PTF can detect systems to over $3\,\mathrm{kpc}$ (Figure 7.5). As the scale height increases, the number of expected detections begins to decrease. We mark scale heights of the expected thin and thick disks using the vertical, dotted lines. The observed number of systems intersects with the expected number of systems at $h \approx 390\,\mathrm{pc}$. We thus conclude that the number of systems detected by the PTF is consistent with the population density derived from the SDSS sample at $h \approx 300\,\mathrm{pc}$.

7.5 Discussion and Conclusion

7.5.1 Scale Height

Most recent AM CVn population studies have assumed that the AM CVn systems are members of the thin disk with a scale height of 200–300 pc (N01, R07, C13). However, the arguments given have been only cursory, with no quantitative evidence suggesting that this scale height is correct. Since the publication of N01 and R07, the population of AM CVn systems has increased by a factor of 3–5 and most have had their orbital period measured. Can we use these new data to differentiate between possible scale heights of the AM CVn system population?

We combine the measured orbital periods with Equation 7.2 to identify the distance of these systems and, together with their Galactic latitude, their height above the plane. The PTF sample with known orbital periods have heights of 270, 280, 550, 740, and 760 pc. The remaining three systems with unknown orbital periods are all equally faint with similar Galactic latitudes.

Are the heights of the systems consistent with a 300 pc scale? If we restrict the results presented in Section 7.4 to certain heights above the Plane, we find that 48% of systems should have $|z| < h$ (= 2.4 ± 1.5 systems) and 14% of systems should have $|z| > 2h$ (= 0.7 ± 0.8 systems). The presence of two systems at $z > 2h$ hints that the scale height may be somewhat higher than 300 pc.

Repeating the same analysis for $h = 900$ pc, we find that we should have detected at least 1 system with $|z| > h$. Given that PTF should detect systems at $d > 3$ kpc, this is not surprising. However, it does indicate that the scale height of AM CVn systems may be between those of the thick and thin disks. Recent work on the Galactic structure indicates that there may not be an explicit thin and thick disk but more of a gradual transition (see, e.g., Schönrich & Binney 2009).

7.5.2 Comparison with Past Studies

The results of Figure 7.7 show that the local population density from C13, $(5 \pm 3) \times 10^{-7}$ pc^{-3}, matches the population of outbursting AM CVn systems detected by the Palomar Transient Factory. The error on this estimate does provide some uncertainty in the scale

height and may hint, similarly to the results in Section 7.5.1, that the scale height is slightly higher than that used by population studies thus far. Other estimates of the density, including those from N01 and R07 are higher by at least a factor of three, and do no match the PTF results for any reasonable value of the scale height.

Can we explain the discrepancies between the earlier estimates and that of C13? Nelemans et al. (2001) used population synthesis to estimate both an optimistic and pessimistic population density that differed in the birth rate assumptions. It is likely that N01's birth rate assumptions were too optimistic and that recent theoretical work on the characteristics of systems that survive the period minimum may help explain the overestimation (Marsh et al. 2004; Kaplan et al. 2012).

The estimate from R07 was based on a small sample with only 20% completeness in the spectroscopic follow-up. In contrast, both the samples in C13 and this paper have had most candidates spectroscopically classified. This shows that without survey completeness a population density is difficult to calculate.

We emphasize several crucial points. The results here are the first time two independent studies have arrived at the same conclusion about the population density of the AM CVn systems. Even more exciting is that the two samples represent different orbital-period regimes of AM CVn systems. While the numbers of the individual samples are too small to reliably test the orbital-period models, the fact that the two samples agree indicates that the orbital-period model does work to at least first order.

We caution, however, that the biases of both the PTF and SDSS samples are not fully understood. The modeling in this paper is dependent on arbitrary fits to observed data. While the relations found in L13 fit the observed systems well, some systems are known to be outliers. Perhaps of greater concern is the lack of understanding of the outburst properties of longer-period systems. For the SDSS sample, the color-criteria are also observationally determined. It is known that not all AM CVn systems fit in this color cut. For example, one of the PTF sample has been found to be redder than other systems (Levitan et al. 2013).

However, the agreement between the results in this paper and those of C13 are certainly exciting. Better verification of the population density and scale height will require significantly more systems that have been systematically selected. We note that this chapter is a work in progress and significant revisions are planned. Despite our results showing

that the population density from the PTF sample matches that from the SDSS sample, the models used here are likely unnecessarily complex and could be simplified. By removing such complexity, we will be able to better understand the population density.

Acknowledgements

Chapter 8

Epilogue

My thesis, and other simultaneous work, has led to enormous advances over the last five years. In 2008, twenty AM CVn systems were known, and many did not have known orbital periods. Now, more than thirty-five systems are known, of which more than 20% were discovered by the PTF, and most have had their orbital periods measured. The PTF-discovered systems, primarily with $P_{orb} < 30\,\mathrm{min}$, are particularly interesting as they are complementary to those discovered by the SDSS, which tend to be at much longer orbital periods.

I first highlight some of the most important results about individual systems and the measurement of their properties:

1. *PTF1J1919+4815:* Perhaps the most interesting system presented in this thesis is PTF1J1919+4815, the partially eclipsing AM CVn system presented in Chapter 5. As the shortest-period outbursting system yet discovered, it will be particularly interesting to monitor its photometric behavior and compare it to that of CR Boo. The transition from high-state system to outbursting system is not well understood, and the discovery of additional systems near the boundary will help significantly.

   The system also provides clues to several, new mysteries. The high-speed light curve from the CHIMERA photometry shows possibly significant variability during parts of the superhump. If confirmed, this may aid in understanding the accretion processes driving the system. PTF1J1919+4815 also contains an optically-thick area at low velocities. The source of this feature, not observed in other systems, remains unknown.

2. *Normal outbursts:* The similar phenomenologies of AM CVn systems and their better-studied, H-rich counterparts, the CVs, has led to the application of many models from CVs to AM CVn systems. The structure of the outbursts has often led to comparisons between the super-outbursts of SU UMa CVs and the outbursts of AM CVn systems,

yet only a few systems (e.g., Kato et al. 2000) showed evidence of the normal outbursts that are a significant part of the SU UMa model. My work in Chapter 2 (particularly the high-cadence monitoring of normal outbursts), Chapter 5, and Chapter 6 shows that the normal outbursts are present in most short-period systems. Their presence in longer-period systems, however, is yet to be determined.

3. *Orbital period determination:* Prior to my work, the only accepted method of orbital period measurement was the blue-over-red method utilizing phase-resolved spectroscopy (Nather et al. 1981). While this remains the "gold standard," the work in Chapter 2 establishing a link between the movement of the hot spot and the photometric variability in quiescence will be extremely useful for future work. It is clear from the systems discovered by the PTF that most future discovered AM CVn systems will be faint. If this link between the photometric period and the orbital period is confirmed for other systems, then it becomes feasible to measure the orbital periods of many systems with smaller telescopes, as opposed to the 8–10 m class telescopes necessary now. This will be particularly useful for the faintest ($g' \geq 22$) systems.

More broadly, the sample of PTF-discovered AM CVn systems have addressed several questions about the AM CVn population:

1. *AM CVn system colors*: In Chapter 4, I compared the colors of five of the PTF-discovered AM CVn systems to that of the SDSS sample. I found that most systems coincided with the color cuts proposed by Roelofs et al. (2009). However, one system did not, which may indicate the possibility that some AM CVn systems are redder than those that have been found thus far. Carter et al. (2013a) recently proposed that the earlier color cut could be constrained even further to optimize the selection of AM CVn systems. The results here show this may not be a wise approach. Only by finding additional non-color-selected systems can we systematically understand how many systems were missed by the SDSS color-selected sample.

2. *Outbursting phenomenology*: The long-term photometric behavior of outbursting AM CVn systems has long been poorly understood and its study has been made difficult by the long recurrence times of the longer orbital-period systems. The most extensive previous work, Ramsay et al. (2012), was hampered by the necessity to pre-select

targets 2.5 yrs before the end of the observations. However, those 2.5 yrs saw the discovery of a significant number of new outbursting systems.

In contrast, the use of multiple synoptic surveys allows for the usage of archival data on a large number of systems. This breadth of information allowed me to draw conclusions about the overall class with the work in Chapter 6. In particular, that set of light curves showed that the outbursting phenomenology of AM CVn systems is even more varied than previously thought, and showed that systems can abruptly change their behavior over a decade-long time scale.

Additionally, it showed that a large number of longer-period systems are undiscovered and that the majority of these appear to have short, 10–15 day outbursts, as opposed to the much longer outbursts previously thought. This means that outbursting-system surveys are substantially more sensitive to the shorter-period systems than the longer-period systems. However, it also highlights that if the SDSS and outburst-selected samples can be combined, then coverage over a large range of orbital periods can be studied.

3. *Uniqueness of individual systems*: The work in Chapter 6 also highlighted that systems with similar orbital periods can have remarkably different behavior. On the short-period end, PTF1J1919+4815, CR Boo, and V803 Cen have orbital periods within minutes of each other, yet V803 Cen is primarily found in the high state, PTF1J1919+4815 has remarkable consistency in its super-outburst recurrence time with clearly defined super outbursts, and CR Boo cycles between these two behaviors. It is of course possible that all three systems exhibit the same long-term changes as seen in CR Boo, and further studies are definitely needed to ascertain this.

On the long-period end, systems such as V406 Hya and SDSSJ1240-0159 show much stronger and longer outbursts than systems with similar orbital periods and outburst recurrence times. This may indicate that the evolutionary history of these systems is different. Recent (Nelemans et al. 2010) and future work on discerning the progenitor of a system based on its current spectrum is particularly exciting in this regard.

4. *AM CVn system population:* Perhaps the most exciting work herein is the population study conducted in Chapter 7. Over the last decade, several studies have made estimates of the population density of AM CVn systems. However, these have never

been observationally supported. The PTF sample has, for the first time, agreed with an earlier study.

This result likely indicates that the population density of AM CVn systems has finally been constrained to within a factor of two. The consistency between Carter et al. (2013a) and this work is particularly noteworthy since the population estimates are from two separate parts of the AM CVn system orbital period range. The former is most sensitive to longer-period systems, while the latter is most sensitive to shorter-period systems.

Although the work presented herein does not emphasize the development of the PTF photomoteric pipeline, a significant portion of my work was the development of this pipeline and the well-calibrated data produced from it. In particular, Section 2.3.1 provides details on the matrix-based, least-squares algorithm that has calibrated most of the data presented here. It has also calibrated all data from the PTF photometric pipeline and papers using that data. I provide some technical details on the photometric pipeline itself in Chapter 3. The quality of the PTF data and an overview of the survey is described briefly in Section 7.2.1, but the performance of the PTF should undoubtedly be better characterized.

8.1   Into the Future

The study of AM CVn systems has perhaps never been more interesting, although maybe not as exciting. Gone are the days when every system changed our understanding of the class. Hopefully, we will soon progress from five or six systems in every systematically selected sample to twenty or thirty. Such samples will result in even more accurate estimates of the population density and may allow the usage of these estimates for studies of supernova rates and the detached white dwarf binary population.

Perhaps most exciting for the discovery of new AM CVn systems are the new, deeper, and more powerful surveys that will soon be commissioned. The last decade has shown the astronomical community that by mining digitized surveys, amazing discoveries can be made. Although the PTF has made its mark on the AM CVn systems, I have no doubt that future surveys, including the Large Synoptic Survey Telescope[1] (LSST) and the Zwicky Transient Facility (ZTF; Kulkarni 2012), will discover even more systems.

---

[1]http://www.lsst.org/

Finding more systems is not the only way to move forward. Recent work on looking backwards in time to understand the progenitors of AM CVn systems will likely yield some of the most exciting new results (e.g., Nelemans et al. 2010). That, combined with our ever better understanding of the merger process of binary white dwarfs will allow us to connect the AM CVn systems to type Ia supernovae and other related phenomena. Recent discoveries of AM CVn progenitors (Kilic et al. 2012) will provide population constraints on both sides.

If anything, the results presented herein show that significant additional study is needed. As a start, the orbital periods of all systems need to be measured so that the orbital period evolution can be understood. Higher-resolution spectra will hopefully provide clues to the origins of the AM CVn systems, and a better understanding of accretion disks may answer questions about the long-term photometric variability of these systems.

I conclude with a plot of the number of known AM CVn systems over time. It is obvious from the extrapolation in Figure 8.1 that there are an infinite number of systems to discover and that we are only a few years away from finding them! The Palomar Transient Factory has done its part in the search. I look forward to the next survey that adds a significant number of systems to our known population.
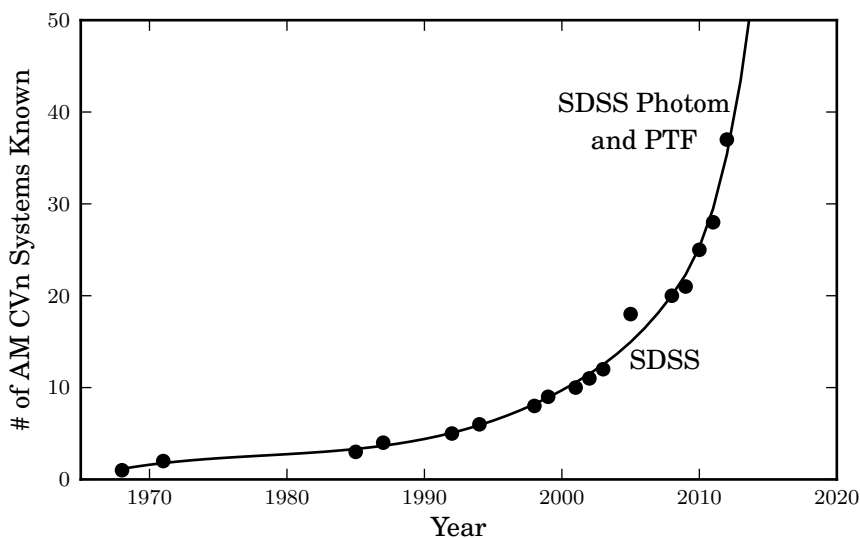
Figure 8.1 The growth of the known sample of AM CVn systems, with the SDSS spectroscopic, follow-up SDSS photometric, and PTF surveys highlighted. Each is accompanied by a significant jump in the number of systems. Points indicate the cumulative distribution. The solid line is a spline interpolation/extrapolation, showing infinite growth in only the next few years!

Bibliography

Abbott, T. M. C., Robinson, E. L., Hill, G. J., & Haswell, C. A. 1992, ApJ, 399, 680

Ahn, C. P., et al. 2012, ApJS, 203, 21

Alted, F., Vilata, I., et al. 2002, PyTables: Hierarchical Datasets in Python

Anderson, S. F., et al. 2005, AJ, 130, 2230

—. 2008, AJ, 135, 2108

Benn, C., Dee, K., & Agócs, T. 2008, in Proc. SPIE Conf., Vol. 7014 (Bellingham: SPIE)

Bertin, E. 2006, in Astronomical Society of the Pacific Conference Series, Vol. 351, Astronomical Data Analysis Software and Systems XV, ed. C. Gabriel, C. Arviset, D. Ponz, & S. Enrique, 112

Bertin, E., & Arnouts, S. 1996, A&AS, 117, 393

Bertin, E., Mellier, Y., Radovich, M., Missonnier, G., Didelon, P., & Morin, B. 2002, in Astronomical Society of the Pacific Conference Series, Vol. 281, Astronomical Data Analysis Software and Systems XI, ed. D. A. Bohlender, D. Durand, & T. H. Handley, 228

Bildsten, L., Shen, K. J., Weinberg, N. N., & Nelemans, G. 2007, ApJ, 662, L95

Bildsten, L., Townsley, D. M., Deloye, C. J., & Nelemans, G. 2006, ApJ, 640, 466

Breedt, E., Gänsicke, B. T., Marsh, T. R., Steeghs, D., Drake, A. J., & Copperwheat, C. M. 2012, MNRAS, 425, 2548

Buat-Ménard, V., & Hameury, J. 2002, A&A, 386, 891

Carter, P. J., et al. 2013a, MNRAS, 429, 2143

—. 2013b, MNRAS, 431, 372

Cenko, S. B., et al. 2006, PASP, 118, 1396

Cepa, J. 1998, A&SS, 263, 369

Copperwheat, C. M., Marsh, T. R., Dhillon, V. S., Littlefair, S. P., Hickman, R., Gänsicke, B. T., & Southworth, J. 2010, MNRAS, 402, 1824

Copperwheat, C. M., et al. 2011, MNRAS, 410, 1113

Deloye, C. J., Taam, R. E., Winisdoerffer, C., & Chabrier, G. 2007, MNRAS, 381, 525

Drake, A. J., et al. 2009, ApJ, 696, 870

Efron, B. 1982, The Jackknife, the Bootstrap and other resampling plans (Philadelphia: Society for Industrial and Applied Mathematics)

Eggleton, P. P. 1983, ApJ, 268, 368

Espaillat, C., Patterson, J., Warner, B., & Woudt, P. 2005, PASP, 117, 189

Faber, S. M., et al. 2003, in Society of Photo-Optical Instrumentation Engineers (SPIE) Conference Series, Vol. 4841, Society of Photo-Optical Instrumentation Engineers (SPIE) Conference Series, ed. M. Iye & A. F. M. Moorwood, 1657–1669

Faulkner, J., Flannery, B. P., & Warner, B. 1972a, ApJ, 175, L79

—. 1972b, ApJ, 175, L79

Findeisen, K., Hillenbrand, L., Ofek, E., Levitan, D., Sesar, B., Laher, R., & Surace, J. 2013, ApJ, 768, 93

Fontaine, G., et al. 2011a, ApJ, 726, 92

—. 2011b, ApJ, 726, 92

Gal-Yam, A., et al. 2011, ApJ, 736, 159

Geier, S., et al. 2013, ArXiv e-prints, 1304.4452

Greiss, S., et al. 2012a, AJ, 144, 24

—. 2012b, ArXiv e-prints, 1212.3613

Groot, P. J., Nelemans, G., Steeghs, D., & Marsh, T. R. 2001, ApJ, 558, L123

Hermes, J. J., et al. 2012, ApJ, 757, L21

Honeycutt, R. K. 1992, PASP, 104, 435

Honeycutt, R. K., Adams, B. R., Turner, G. W., Robertson, J. W., Ost, E. M., & Maxwell, J. E. 2013, PASP, 125, 126

Hook, I. M., Jørgensen, I., Allington-Smith, J. R., Davies, R. L., Metcalfe, N., Murowinski, R. G., & Crampton, D. 2004, PASP, 116, 425

Horne, K. 1986, PASP, 98, 609

Hynes, R. I. 2002, in Astronomical Society of the Pacific Conference Series, Vol. 261, The Physics of Cataclysmic Variables and Related Objects, ed. B. T. Gänsicke, K. Beuermann, & K. Reinsch, 676

Jha, S., Garnavich, P., Challis, P., Kirshner, R., & Berlind, P. 1998, IAUC, 6983, 1

Jurić, M., et al. 2008, ApJ, 673, 864

Kaplan, D. L., Bildsten, L., & Steinfadt, J. D. R. 2012, ApJ, 758, 64

Kasliwal, M. M., et al. 2010, ApJ, 723, L98

Kato, T., Nogami, D., Baba, H., Hanson, G., & Poyner, G. 2000, MNRAS, 315, 140

Kato, T., Stubbings, R., Monard, B., Butterworth, N. D., Bolt, G., & Richards, T. 2004, PASJ, 56, 89

Kato, T., et al. 2001, Inf. Bull. Variable Stars, 5120

Kilic, M., Brown, W. R., Allende Prieto, C., Kenyon, S. J., Heinke, C. O., Agüeros, M. A., & Kleinman, S. J. 2012, ApJ, 751, 141

Kotko, I., Lasota, J.-P., Dubus, G., & Hameury, J.-M. 2012, A&A, 544, A13

Kulkarni, S. R. 2012, ArXiv e-prints, 1202.2381

Kupfer, T., Groot, P., Steeghs, D., Levitan, D., & Rutten, R. in press, MNRAS

Landau, L. D., & Lifshitz, E. M. 1971, The classical theory of fields

Lang, D., Hogg, D. W., Mierle, K., Blanton, M., & Roweis, S. 2010, AJ, 139, 1782

Lasota, J.-P. 2001, New A Rev., 45, 449

Law, N. M., et al. 2009, PASP, 121, 1395

Levitan, D., et al. 2011, ApJ, 739, 68

—. 2013, MNRAS, 430, 996

Margon, B., Levitan, D., Prince, T. A., & Hallinan, G. 2013, in Stella Novae: Future and
    Past Decades, ed. P. A. Woudt & V. A. R. M. Ribeiro (ASPCS)

Marsh, T. R. 1989, PASP, 101, 1032

Marsh, T. R., & Horne, K. 1988, MNRAS, 235, 269

Marsh, T. R., Horne, K., & Rosen, S. 1991, ApJ, 366, 535

Marsh, T. R., Nelemans, G., & Steeghs, D. 2004, MNRAS, 350, 113

Marsh, T. R., et al. 2007, in ASP Conf. Ser., Vol. 372, 15th European Workshop on White
    Dwarfs, ed. R. Napiwotzki & M. R. Burleigh (San Francisco: ASP), 431

Matthews, O. M., Speith, R., Wynn, G. A., & West, R. G. 2007, MNRAS, 375, 105

McCarthy, J. K., et al. 1998, Proc. SPIE, 3355, 81

Miller, J., & Stone, R. 1992, The CCD Cassegrain Spectrograph at the Shane Reflector,
    Tech. Rep. 48, Santa Cruz:Lick Observatory

Miller, J. S., Robinson, L. B., & Goodrich, R. W. 1988, in Instrumentation for Ground-
    Based Optical Astronomy, ed. L. B. Robinson, 157

Monet, D. G., et al. 2003, AJ, 125, 984

Morales-Rueda, L., Marsh, T. R., Steeghs, D., Unda-Sanzana, E., Wood, J. H., & North,
    R. C. 2003, A&A, 405, 249

Nather, R. E., Robinson, E. L., & Stover, R. J. 1981, ApJ, 244, 269

Naylor, T. 1998, MNRAS, 296, 339

Nelemans, G. 2005, in ASP Conf. Ser., Vol. 330, The Astrophysics of Cataclysmic Variables and Related Objects, ed. J.-M. Hameury & J.-P. Lasota (San Francisco: ASP), 27

Nelemans, G., Portegies Zwart, S. F., Verbunt, F., & Yungelson, L. R. 2001, A&A, 368, 939

Nelemans, G., Yungelson, L. R., & Portegies Zwart, S. F. 2004, MNRAS, 349, 181

Nelemans, G., Yungelson, L. R., van der Sluys, M. V., & Tout, C. A. 2010, MNRAS, 401, 1347

Nissanke, S., Vallisneri, M., Nelemans, G., & Prince, T. A. 2012, ApJ, 758, 131

Nogami, D., Monard, B., Retter, A., Liu, A., Uemura, M., Ishioka, R., Imada, A., & Kato, T. 2004, PASJ, 56, L39

Ofek, E. O., Frail, D. A., Breslauer, B., Kulkarni, S. R., Chandra, P., Gal-Yam, A., Kasliwal, M. M., & Gehrels, N. 2011, ApJ, 740, 65

Ofek, E. O., et al. 2012, PASP, 124, 62

Oke, J. B., & Gunn, J. E. 1982, PASP, 94, 586

Oke, J. B., et al. 1995, PASP, 107, 375

Osaki, Y. 1989, PASJ, 41, 1005

—. 1996, PASP, 108, 39

Paczyński, B. 1967, Acta Astron., 17, 287

—. 1971, Acta Astron., 21, 1

Patterson, J., Walker, S., Kemp, J., O'Donoghue, D., Bos, M., & Stubbings, R. 2000, PASP, 112, 625

Patterson, J., et al. 1997, PASP, 109, 1100

—. 2002, PASP, 114, 65

—. 2005, PASP, 117, 1204

Podsiadlowski, P., Han, Z., & Rappaport, S. 2003, MNRAS, 340, 1214

Provencal, J. L., et al. 1997, ApJ, 480, 383

Ramsay, G., Barclay, T., Steeghs, D., Wheatley, P. J., Hakala, P., Kotko, I., & Rosen, S. 2012, MNRAS, 419, 2836

Ramsay, G., et al. 2010, MNRAS, 407, 1819

Rau, A., Roelofs, G. H. A., Groot, P. J., Marsh, T. R., Nelemans, G., Steeghs, D., Salvato, M., & Kasliwal, M. M. 2010, ApJ, 708, 456

Rau, A., et al. 2009, PASP, 121, 1334

Reegen, P. 2007, A&A, 467, 1353

Richards, J. W., et al. 2011, ApJ, 733, 10

Roelofs, G. H. A., Groot, P. J., Benedict, G. F., McArthur, B. E., Steeghs, D., Morales-Rueda, L., Marsh, T. R., & Nelemans, G. 2007a, ApJ, 666, 1174

Roelofs, G. H. A., Groot, P. J., Marsh, T. R., Steeghs, D., Barros, S. C. C., & Nelemans, G. 2005, MNRAS, 361, 487

Roelofs, G. H. A., Groot, P. J., Marsh, T. R., Steeghs, D., & Nelemans, G. 2006a, MNRAS, 365, 1109

Roelofs, G. H. A., Groot, P. J., Nelemans, G., Marsh, T. R., & Steeghs, D. 2006b, MNRAS, 371, 1231

—. 2007b, MNRAS, 379, 176

Roelofs, G. H. A., Groot, P. J., Steeghs, D., Marsh, T. R., & Nelemans, G. 2007c, MNRAS, 382, 1643

Roelofs, G. H. A., Nelemans, G., & Groot, P. J. 2007d, MNRAS, 382, 685

Roelofs, G. H. A., Rau, A., Marsh, T. R., Steeghs, D., Groot, P. J., & Nelemans, G. 2010, ApJ, 711, L138

Roelofs, G. H. A., et al. 2009, MNRAS, 394, 367

Ruiz, M. T., Rojo, P. M., Garay, G., & Maza, J. 2001, ApJ, 552, 679

Sackett, P. D. 1997, ApJ, 483, 103

Scargle, J. D. 1982, ApJ, 263, 835

Schlegel, D. J., Finkbeiner, D. P., & Davis, M. 1998, ApJ, 500, 525

Schoembs, R., & Hartmann, K. 1983, A&A, 128, 37

Schönrich, R., & Binney, J. 2009, MNRAS, 399, 1145

Sesar, B., Stuart, J. S., Ivezić, Ž., Morgan, D. P., Becker, A. C., & Woźniak, P. 2011, AJ,, 142, 190

Shears, J., Brady, S., Koff, R., Goff, W., & Boyd, D. 2011, ArXiv e-prints, 1104.0107

Shporer, A., Brown, T., Lister, T., Street, R., Tsapras, Y., Bianco, F., Fulton, B., & Howell, A. 2010, arXiv:1011.6394

Smak, J. 1967, Acta Astron., 17, 255

Smith, A. M., et al. 2011, MNRAS, 412, 1309

Solheim, J. 2010, PASP, 122, 1133

Steeghs, D., Marsh, T. R., Barros, S. C. C., Nelemans, G., Groot, P. J., Roelofs, G. H. A., Ramsay, G., & Cropper, M. 2006, ApJ, 649, 382

Stokes, G. H., Evans, J. B., Viggh, H. E. M., Shelly, F. C., & Pearce, E. C. 2000, Icarus, 148, 21

van Dokkum, P. G. 2001, PASP, 113, 1420

Warner, B. 1995, Cataclysmic variable stars (Cambridge: Cambridge University Press)

Webbink, R. F. 1984, ApJ, 277, 355

Wood, M. A., Casey, M. J., Garnavich, P. M., & Haag, B. 2002, MNRAS, 334, 87

Wood-Vasey, W. M., Aldering, G., Nugent, P., & Li, K. 2003, IAUC, 8077, 1

Woudt, P. A., Warner, B., & Motsoaledi, M. 2013, The Astronomer's Telegram, 4726, 1

Woudt, P. A., Warner, B., & Rykoff, E. 2005, IAUC, 8531, 3